

**SUB-DOPPLER LASER COOLING OF LITHIUM ATOMS
IN A GRAY OPTICAL MOLASSES**

CHRISTINE SATTER

(Bachelor of Science, Utrecht University)

**A THESIS SUBMITTED FOR THE DEGREE OF MASTER
OF SCIENCE**

**DEPARTMENT OF PHYSICS
NATIONAL UNIVERSITY OF SINGAPORE**

2017

Declaration

I hereby declare that this thesis is my original work and it has been written by me in its entirety. I have duly acknowledged all the sources of information which have been used in the thesis.

This thesis has also not been submitted for any degree in any university previously.

A handwritten signature in black ink, appearing to read 'Christine Satter', is written over a horizontal line.

CHRISTINE SATTER

8 August 2017

Acknowledgments

A successful completion of the work presented in this thesis would not have been possible without the expertise, time, and good company that many have shared with me during my candidature as a Master's student at CQT. To the following people I am especially grateful.

First and foremost I would like to thank my supervisor, Prof. Kai Dieckmann, for the opportunity to work and learn on this experiment, and for the countless discussions and suggestions. His enthusiasm for his work is inspiring, and I have learned a great deal from him about physics, and thinking of creative solutions in the lab. I would like to thank him also for his valuable feedback during the preparation of this thesis document, and the preceding seminar presentation.

Much gratitude is due to the PhD graduate from our lab, and our mentor, Christian Gross, whose experience and insight into the physics of our experiment greatly helped us forward on many occasions. His generosity also saved me much time and effort in the creation of this thesis. Former group members Sambit Bikas Pal, Mark Lam and Jaren Gan should also be mentioned, for their readiness to help me learn all there is to learn in an atomic physics lab.

I would like to express my sincere gratitude to my friend and colleague Senmao Tan, with whom the experiment on the gray molasses was carried out. With him exciting moments in the lab were shared, such as the first observation of cooling with the new method. Together with our colleagues on the mixture experiment, Andrew Laugharn and Anbang Yang, fruitful discussions and pleasant moments inside and outside of the lab setting were enjoyed.

There are many more in CQT that I would like to thank for their contributions

in some form or another. I am thankful to the research support staff, especially Dileej Nair, Teo Kok Seng, and Bob Chia Zhi Neng, for their creative input and help in fabricating the new mount for the tapered amplifier, and countless other small objects. Also the CQT admin office was always there to sort out any administrative issue quickly and efficiently, and for that I am grateful.

Outside of the work sphere, I would like to thank friends both in Europe and Singapore (or wherever they currently are), who know all about my experience and have supported me throughout. My time at the university, and in Singapore, has been greatly enhanced because of them.

Last but far from least, I would like to thank my brother and my parents for their unfailing support.

Contents

Summary	ix
List of Tables	xi
List of Figures	xiii
1 Introduction	1
2 Sub-Doppler laser cooling of ${}^6\text{Li}$ atoms	7
2.1 Laser Cooling	7
2.1.1 Doppler cooling	7
2.1.2 The bright optical molasses	8
2.2 Spectral resolution of excited state manifolds	10
2.3 Cooling in a gray molasses	12
2.3.1 Coherent population trapping in dark states	13
2.3.2 Motional coupling and VSCPT	14
2.3.3 Confinement in momentum space	15
2.3.4 A gray Sisyphus cycle	16
2.3.5 The gray molasses and ${}^6\text{Li}$	18
3 Experimental set-up and techniques	21
3.1 Overview: experimental sequence and laser sources	21
3.1.1 Sequence of the experiment	21
3.1.2 The cooling light	24
3.2 Tapered gain elements	26
3.2.1 Laser diode dimensions	26
3.2.2 Tapered amplifier properties and operation	27
3.2.3 Protecting the TA	29
3.3 The independent set-up	30
3.3.1 Design of TA mount	32
3.3.2 Fiber coupling	34
3.3.3 TA operating behaviour	35

3.4	The integrated set-up	37
3.4.1	The MOT laser system	38
3.4.2	Integration of the gray molasses light	39
3.5	The optical dipole trap	40
3.6	Detection	42
4	The gray optical molasses	45
4.1	Analyzing cold atomic clouds	45
4.2	The D_2 magneto-optical trap	47
4.3	Sub-Doppler cooling in a D_1 gray optical molasses	49
4.3.1	Characterization of the gray molasses	50
4.3.2	Compensation of earth and stray magnetic fields	54
4.3.3	Analysis of time of flight measurements	57
4.3.4	Optimal performance and discussion	60
4.4	Summary	64
5	Atomic transfer into an optical dipole trap	65
5.1	Optical dipole trapping	65
5.1.1	The conservative potential	66
5.1.2	The trap loading process	67
5.1.3	Gray molasses as precursor to ODT loading	69
5.2	Loading the ODT from the gray molasses	70
5.2.1	Optimizing the captured atom number	70
5.2.2	Discussion	74
5.3	Cooling in the UV MOT	76
5.3.1	Optimization of phase-space density	77
5.3.2	Hold time of the UV MOT	78
5.4	Summary and outlook	80
6	Conclusion and Outlook	83
	Bibliography	85

Summary

Alkali-metal atoms are prime candidates for studies of degenerate quantum gases and standard magneto-optical trapping and cooling of these elements to the Doppler limit is conventionally done on the D_2 transition. However, typical sub-Doppler cooling techniques are not effective for lithium because of this species' unresolved hyperfine structure in the excited state. In this research work, a gray optical molasses operating on the D_1 atomic transition is applied to cool a cloud of ${}^6\text{Li}$ atoms to sub-Doppler temperatures. This method combines velocity-selective coherent population trapping with polarization-gradient cooling in a blue-detuned Sisyphus cycle.

A new laser system was constructed to produce the light on the D_1 wavelength for gray molasses cooling. To achieve the required optical power, a tapered amplifier chip was installed in this set-up and its performance was characterized. In the experiment a different set-up is eventually used, which allows for more convenient integration of the new D_1 -frequency light into the pre-existing laser system. Here, a scheme is used where D_2 - and D_1 -frequency light beams rapidly take turns injection seeding the same diode laser. A beat system is set up that allows us to monitor the correct seeding of the diode laser during the different stages of the experimental sequence, in a fast, time-resolved manner.

We observe that the gray molasses efficiently cools the atoms from 380 to 32 μK in 2.5 ms. From a compressed magneto-optical trap, 2.8×10^8 atoms are captured in the low-intensity molasses. A characterization of the gray molasses is presented and the influence of magnetic eddy fields on its efficacy is discussed. A comparison is made based on results that were previously achieved in gray molasses experiments. While our cloud is cold, a reduction in the peak density after the molasses phase is observed. Likely for this reason, an attempt to transfer the atoms from the gray molasses into an optical dipole trap was so far not efficient. A discussion is given, and suggestions are put forward to improve these results.

List of Tables

4.1	Overview of the fit parameters extracted from the Gaussian cloud expansion fitting routine	59
4.2	The performance of the gray molasses as reported in the present study, and that of three other lithium experiments	61
5.1	Parameters of the crossed ODT under typical trapping conditions and of a single-beam ODT consisting of one of the individual ODT beams.	70

List of Figures

2.1	Polarization gradients in a $\text{lin}\perp\text{lin}$ configuration	9
2.2	The Sisyphus cooling cycle in conventional sub-Doppler cooling	10
2.3	Partial level structure of ${}^6\text{Li}$	12
2.4	The atomic Λ -structure for CPT in dark states	14
2.5	The gray molasses cooling scheme	17
3.1	Top view of part of the experimental apparatus	22
3.2	Level scheme of the D_1 and D_2 transitions	25
3.3	Propagation of a beam through a TA chip	28
3.4	The independent set-up for the production of gray molasses light	31
3.5	Design of the copper base and components for mounting the TA chip	33
3.6	The TA output power as a function injection current and seed power	36
3.7	The integrated set-up for the production of gray molasses light	38
4.1	Overview of the experimental sequence for gray molasses	49
4.2	Temporal evolution of the gray molasses	51
4.3	Atom number and radius of gray molasses as a function of global detuning	52
4.4	Atom number and radius of gray molasses as a function of Raman detuning	52
4.5	Atom number and radius of gray molasses as a function of intensity	54
4.6	Atom number and radius of gray molasses as a function of magnetic bias field	56
4.7	Comparison of GM time of flight fit curves	58
4.8	Time-of-flight temperature measurement of cMOT and gray molasses	60
5.1	Atom number in ODT as function of MOT loading time and Raman detuning	72
5.2	Atom number in ODT as function of ODT activation time	73
5.3	Atom number and radius of UV MOT as function of hold time	79

1 Introduction

Research Area

The study of ultracold atomic gases forms an active area of research due to the opportunity they present to study quantum many-body physics with high tunability and control (Bloch et al., 2008). At temperatures of a few nanokelvins above absolute zero, many-body quantum phases of atoms become accessible. For bosonic particles, an interesting state of matter called Bose-Einstein condensate (BEC) can be produced in experiments below a critical temperature (Anderson et al., 1995), as a direct consequence of quantum statistics for indistinguishable particles. An ultracold, non-interacting gas of fermionic particles on the other hand, is prohibited from undergoing the phase transition into a BEC by the Pauli principle. However, close to a Feshbach resonance, an ultracold Fermi gas can enter the strongly interacting regime where quantum many-body effects play an important role (Bloch et al., 2008). As the strength of the inter-particle interaction is increased, the exhibited behaviour of the degenerate gas varies continuously from Cooper pairing of weakly attracting independent fermions, described by the Bardeen-Cooper-Schrieffer (BCS) model (Bardeen et al., 1957; Nozière and Schmitt-Rink, 1985), to a BEC of tightly bound di-fermionic molecules (Cubizolles et al., 2003; O'Hara et al., 2002). This transition and the intermediate regime in between, known as the BEC-BCS cross-over, are subjects of great interest.

The first quantum degenerate Fermi gases with ultracold atoms were realized by DeMarco and Jin (1999) with potassium and by among others Truscott et al. (2001) with lithium atoms, which are the only stable fermionic alkali-metal isotopes. Both have accessible Feshbach resonances, but ${}^6\text{Li}$ offers especially favorable properties near the resonance for studying the

BEC-BCS crossover regime. The ${}^6\text{Li}$ Feshbach resonance is exceptionally broad (Chin et al., 2010), and on the molecular side of the resonance the trapped sample enjoys a lifetime on the order of seconds (Ketterle and Zwierlein, 2008), much longer than for e.g. ${}^{40}\text{K}$ (Regal et al., 2004).

Crucial for obtaining the low temperatures required to form quantum degenerate gases was the advent of laser cooling and the realization of the magneto-optical trap (MOT) (Chu et al., 1985; Raab et al., 1987). Only temperatures down to the limit dictated by Doppler theory were expected, but surprisingly even lower values were found (Lett et al., 1988). The apparent additional cooling mechanism at work was explained by Dalibard and Cohen-Tannoudji (1989) and attributed to interference effects between the trapping lasers in combination with the multilevel structure of the atoms. An even lower temperature regime can be accessed with evaporative cooling of the atoms (Masuhara et al., 1988), which then enables the achievement of quantum degeneracy and Bose-Einstein condensation.

The experimental realization of a degenerate quantum gas is more challenging for ${}^6\text{Li}$ atoms than for most other alkali-metal species. Standard sub-Doppler cooling methods are inefficient for lithium, which is attributed to the fact that the D_2 transition, on which laser cooling is commonly performed, is characterized by an unresolved hyperfine structure of the excited state (Fort et al., 1998). Methods of cooling on lithium that circumvent this problem are therefore an active area of research. Narrow-line Doppler cooling is one method that has been shown to be effective, as was first demonstrated by Duarte et al. (2011). This technique was successfully implemented in our set-up (Sebastian et al., 2014) by cooling in a MOT on the narrow-linewidth $2S_{1/2} \rightarrow 3P_{3/2}$ transition, which has a wavelength in the ultraviolet range. The UV MOT achieves a final temperature of around $50\ \mu\text{K}$ and high phase-space densities (10^{-4}), facilitating loading into a small-angle, crossed optical dipole trap (ODT) for subsequent cooling stages (Gross et al., 2016).

Another method that has recently been used to obtain sub-Doppler temperatures for ${}^6\text{Li}$ is the gray optical molasses (Rio Fernandes et al., 2012). This method combines velocity-selective coherent population trapping with a friction force in the form of an optical molasses. The gray molasses significantly reduces the temperature of the atomic ensemble and was used

for efficient all-optical production schemes for quantum gases (Burchianti et al., 2014; Salomon et al., 2014), among which ${}^6\text{Li}$ Fermi gases (Burchianti et al., 2015). The gray molasses operates on the D_1 transition, which is slightly better resolved than the D_2 transition, and for which laser sources are readily available. An additional benefit of the gray molasses is the use of dark states, so that cooling is in principle not limited to the single-photon recoil temperature and less loss is experienced due to light-assisted atomic interactions (Aspect et al., 1988).

Photoassociation spectroscopy

Another interesting application of ultracold atoms is photoassociation spectroscopy (Abraham et al., 1995; Lett et al., 1993; Miller et al., 1993). Photoassociation (PA) refers to the formation of long-range molecules out of two colliding atoms under the absorption of a photon. Among many applications, PA spectroscopy can be used to measure the ground-state s -wave scattering length, which characterizes the collisional properties of ultracold trapped atoms. PA is also an important tool for the production of ultracold ground-state molecules (Ulmanis et al., 2012). While PA spectroscopy of lithium below the $2S$ - $2P$ asymptote has received abundant attention from theorists and experimentalists alike, as discussed by e.g. LeRoy et al. (2009) and Dattani and LeRoy (2011), there is so far no experimental data on the long-range part for any of the lithium potentials correlated to the $2S$ - $3P$ asymptote (Musial and Kucharski, 2014).

An attempt at a PA measurement to molecular states of this unexplored potential was made in our set-up (Gross, 2016). Since the photon required for PA on this transition is in the UV range, the 323-nm laser for narrow-line sub-Doppler cooling was used. Atoms were loaded into a MOT on the D_2 line and exposed to the PA laser. A scan covering a frequency interval of 140 GHz was performed, but the results showed no clear deviation from the background due to off-resonant atomic excitations. From thorough calculations of PA transition rates (Gross, 2016) could be concluded that PA transitions to states correlated to the $2S$ - $3P$ asymptote are difficult to observe in a magneto-optical trap, where an involved experimental sequence is required to suppress background noise. In order to observe the

weak PA transitions, the measurement should rather be performed in the optical dipole trap to benefit from higher atomic densities and a different scaling of atomic and molecular transition rates. As mentioned, the ODT was previously loaded from the UV MOT, which yields sub-Doppler temperatures through narrow-line cooling. For the PA experiment, the UV laser would now have to be used to provide the light for the PA transition. Revisiting this PA experiment would therefore mean abandoning narrow-line cooling, and finding an alternative sub-Doppler cooling scheme for ${}^6\text{Li}$.

This thesis

In this thesis, a gray optical molasses is implemented and optimized as a sub-Doppler cooling strategy for ${}^6\text{Li}$, to replace narrow-line cooling on the UV line. For this purpose, an additional laser source and subsystem have been added and conveniently integrated into the pre-existing set-up for cooling on the D_2 transition. The performance of gray molasses cooling in our set-up is characterized, and the transfer efficiency of the cooled atoms into a crossed optical dipole trap is investigated.

This thesis is divided into the following chapters. **In Chapter 2**, a theoretical framework is introduced for understanding sub-Doppler cooling of ${}^6\text{Li}$ atoms. The chapter begins with a brief review of the Doppler limit and Sisyphus cooling. Next, the reason for the inefficacy of standard techniques for cooling of lithium is discussed. In this research work, a gray optical molasses is employed to achieve sub-Doppler temperatures, and the cooling mechanism underlying this method is described in detail.

In Chapter 3, the experimental set-up for producing the gray molasses is described. First an overview of the sequence of the experiment is given, in conjunction with a description of several relevant parts of the apparatus. Then, the laser system that produces the light for the gray molasses on the atomic D_1 transition is described. Initially a new, independent laser set-up was built for this purpose, with its own light source and amplifying medium to increase the available optical power. Eventually however, a simpler, more convenient way of integrating the molasses light into the pre-existing laser system for the atomic D_2 transition

was chosen for implementation in the experiment. In this chapter, both set-ups are discussed. The chapter ends with a description of the optical dipole trap and our detection technique for obtaining information about our atomic cloud.

In Chapter 4, the sub-Doppler laser cooling scheme for ${}^6\text{Li}$ based on a gray optical molasses is described. First, a short overview is given of the statistical quantities by which we assess the quality of our cold atomic clouds during the various stages of the experiment. Then follows a description of the MOT that is applied on the D_2 atomic transition to pre-cool the atoms for capture in the gray molasses. The molasses rapidly reduces the temperature of the cloud and enhances the phase-space density by an order of magnitude. Our characterization of the gray molasses is presented. Canceling residual magnetic fields proved to be crucial for effective cooling, and was a challenge in our set-up due to the presence of long-lived eddy currents. Finally, the results that optimize the phase-space density of the gray molasses are discussed and compared with those obtained in other studies.

In Chapter 5, an attempt is described to transfer the atoms from the gray molasses-cooled cloud into the crossed optical dipole trap (ODT). A discussion is given of the principle of optical dipole trapping and trap loading dynamics. Subsequently, our results on the capture efficiency are presented. In our first attempts to load the atoms from the gray molasses into the ODT the transfer efficiency was so far low. This is discussed in the context of the loading mechanism of the ODT and the quality of the gray molasses-cooled cloud. To verify that the ODT is operating as desired, we instead pre-cool the cloud in a MOT on the UV transition, with the intent of emulating the ODT loading experiment performed in our set-up by [Gross et al. \(2016\)](#). An oscillatory phenomenon was however detected in the UV MOT dynamics that interfered with obtaining high densities. This phenomenon is discussed, and an outlook is given on the suitability of the gray molasses for loading the ODT in our experiment.

2 Sub-Doppler laser cooling of ${}^6\text{Li}$ atoms

In this chapter a theoretical framework is introduced for understanding sub-Doppler cooling of ${}^6\text{Li}$ atoms. The chapter begins with a brief review of the Doppler limit and Sisyphus cooling. Next, the reason for the inefficacy of standard techniques for cooling of lithium is discussed. In this research work, a gray optical molasses is employed to achieve sub-Doppler temperatures, and the cooling mechanism underlying this method is described in detail.

2.1 Laser Cooling

Cooling by radiation pressure was first proposed in the late 1970s by [Hänsch and Schawlow \(1975\)](#) for a gas of neutral atoms and by [Wineland and Dehmelt \(1975\)](#) for ions in an electromagnetic trap. Today, laser cooling and trapping are standard techniques in the field of atomic physics and is used for all experiments investigating quantum degenerate gases. Atomic samples at temperatures in the micro- and even nanokelvin range are obtained by exploiting exchanges of energy and momentum between atoms and laser light ([Chu, 1998](#); [Cohen-Tannoudji, 1998](#); [Phillips, 1998](#)). A comprehensive treatment of laser cooling schemes in general can be found in e.g. [Metcalf and van der Straten \(1999\)](#) and [Guéry-Odelin and Cohen-Tannoudji \(2011\)](#).

2.1.1 Doppler cooling

Laser cooling is based on the scattering force that atoms experience when exposed to a light field that is near-resonant with an atomic transition. When the light field is red-detuned with respect to the atomic transition, the Doppler-induced imbalance between opposite scattering forces results in a net force that always opposes the motion of the atom. In a 3D optical

molasses configuration, counter-propagating laser beams along three spatial directions provide this damping force in all three dimensions.

For a given laser detuning δ , the damping force is highest for a class of atoms with a certain velocity v . As the detuning is decreased, the atoms that are most strongly addressed are those that move more slowly. The equilibrium temperature that is reached by Doppler cooling is then dependent on δ , as (Metcalf and van der Straten, 1999)

$$k_{\text{B}}T = \frac{\hbar\Gamma}{4} \left(\frac{2|\delta|}{\Gamma} + \frac{\Gamma}{2|\delta|} \right) . \quad (2.1)$$

Here, a negative δ and is assumed, and Γ is the natural linewidth of the excited state in the atomic transition. When $|\delta|$ becomes much smaller than the linewidth it becomes unresolved, and an even slower velocity class of atoms cannot be addressed. The minimum temperature that can be reached by Doppler cooling is achieved at a laser detuning of $\delta = -\Gamma/2$ and is given by (Metcalf and van der Straten, 1999)

$$k_{\text{B}}T_{\text{D}} = \frac{\hbar\Gamma}{2} . \quad (2.2)$$

Here, T_{D} is called the Doppler temperature. From the previous argument, an intuitive picture follows of the dependence of the temperature limit on the natural linewidth. For a larger natural linewidth, the smallest resolved detuning is also relatively large, leading to a higher overall temperature.

2.1.2 The bright optical molasses

An early experiment using laser cooling on sodium atoms by Lett et al. (1988) surprisingly found temperatures lower than what was predicted to be possible by Doppler theory, as was verified by the use of several different techniques of temperature measurement. Since Doppler theory was rigorous for two-level atoms, an explanation would have to involve the Zeeman sublevel structure of the atomic energy levels. This explanation was found by Dalibard and Cohen-Tannoudji (1989), who proposed a dissipative mechanism due to polarization gradients.

The sub-Doppler cooling mechanism is commonly understood by considering the movement

of an atom through a red-detuned light field in lin \perp lin configuration, as shown in Fig. 2.1. In this configuration, a standing wave is formed by two counter-propagating laser beams with orthogonal linear polarizations. The overall polarization of the standing wave varies periodically with position, such that the polarization is σ_+ and σ_- at intervals separated by a distance $\lambda/4$. In the case of a $J = 1/2 \rightarrow J' = 3/2$ atomic transition, there are only two Zeeman sublevels in the ground state. Because of the off-resonant laser field, light shifts will be induced in these sublevels and due to the polarization gradient these light shifts are spatially modulated with period $\lambda/2$. The light shift potentials thus formed in space for the two $J = 1/2$ sublevels are out of phase, as shown in Fig. 2.2. For a moving atom in a given Zeeman sublevel the probability to be optically pumped to the other sublevel is highest at the top of the potential hill, due to the local polarization of the light field. The atom is pumped to the bottom of the valley of the other sublevel after which it starts another movement up the slope of the potential. Because the timescale τ_p for optical pumping is much larger than the lifetime of the excited state $1/\Gamma$, the atom spends more time traveling uphill than downhill in the potential landscape. In each step of this Sisyphus cooling cycle the atom thus loses an amount of kinetic energy that is approximately equal to the depth of the potential U_0 . This energy is carried away by the spontaneously emitted photon in the optical pumping process.

The Sisyphus mechanism ceases to be effective when the kinetic energy of the atom becomes insufficient to climb the potential hill. Hence the equilibrium temperature is given by (Foot,

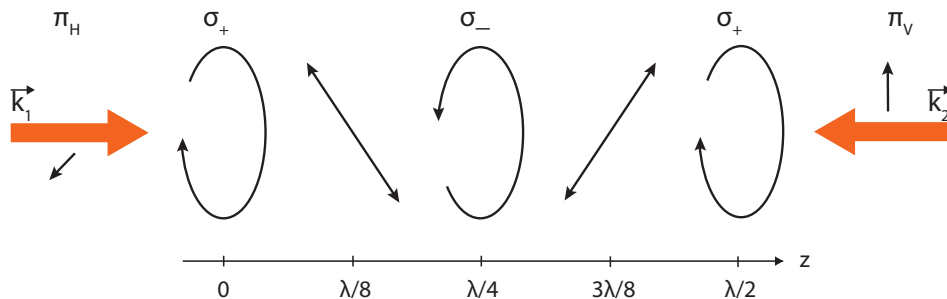


Figure 2.1: Polarization gradients in a lin \perp lin light configuration. Two counter-propagating laser beams with orthogonal linear polarizations together create a standing wave with polarization gradients along the axial position.

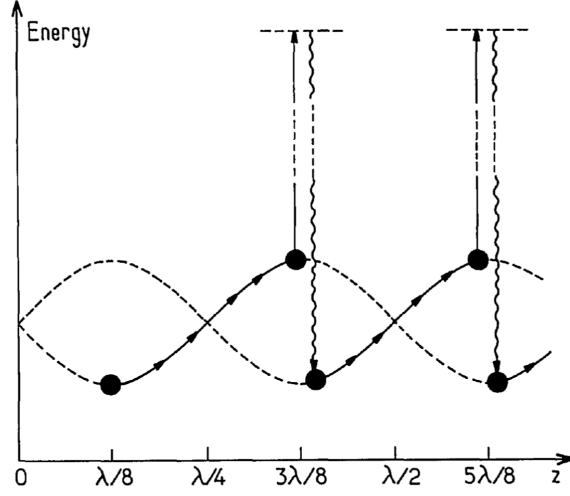


Figure 2.2: The Sisyphus cooling cycle in conventional sub-Doppler cooling. Spatially modulated light shifts are induced in the Zeeman sublevels of the ground state. Atoms are optically pumped from one sublevel to another with highest probability at the top of the potential hill. The repetition of multiple cycles leads to a reduction in the kinetic energy of the atom. Figure from [Dalibard and Cohen-Tannoudji \(1989\)](#).

2005)

$$k_{\text{B}}T_{\text{sub-Doppler}} \simeq U_0 \propto \frac{I}{|\delta|} \quad , \quad (2.3)$$

where an intensity I much smaller than the saturation intensity ($I/I_{\text{sat}} \ll 1$) and large detuning $|\delta| \gg \Gamma$ have been assumed. However, the loss of energy by climbing a potential hill is balanced by the recoil energy that the atom acquires during spontaneous emission of the photon. Therefore, a fundamental limit to sub-Doppler cooling exists in the form of the recoil limit, where the minimum temperature is given by ([Foot, 2005](#))

$$k_{\text{B}}T_{\text{r}} = \frac{h^2}{M\lambda^2} \quad . \quad (2.4)$$

Here, M is the atomic mass and λ the wavelength of the spontaneously emitted photon.

2.2 Spectral resolution of excited state manifolds

The then new Sisyphus technique was soon tested and applied successfully to sodium ([Lett et al., 1988](#)), cesium ([Salomon et al., 1990](#)) and rubidium atoms ([Shang et al., 1991](#)). It is

a popular choice for achieving sub-Doppler temperatures due to its relatively low technical requirements. However, some species proved stubborn against the Sisyphus mechanism. Sub-Doppler temperatures have not been observed for ${}^6\text{Li}$, and for ${}^{40}\text{K}$ the cooling mechanism seems to operate less than optimally as compared to the other species (Gokhroo et al., 2011; Modugno et al., 1999), as characterized by bimodal temperature distributions where a fraction of the atoms does not experience cooling.

In theoretical models (constructed for ${}^{39}\text{K}$) the efficiency of sub-Doppler cooling was shown to be reduced for small hyperfine splittings of the excited state (Fort et al., 1998). If the spectral resolution of the excited state manifold is on the order of only a few natural linewidths, addressing an individual hyperfine state is compromised and efficient optical pumping is enabled. Strong, off-resonant excitations of other excited hyperfine states can cause interference processes between transitions. For ${}^{39}\text{K}$ for example, with an excited state spectral resolution of 5.4Γ , only a small window of laser detunings δ is available for which sub-Doppler forces do not suffer from these interference effects (Landini et al., 2011). Consequently the capture range of the sub-Doppler force is greatly reduced and effective pre-cooling stages need to be applied. For ${}^{40}\text{K}$ the splitting between the two relevant states is about 7Γ , which is still considered small, in particular in comparison to rubidium and cesium.

The level structure of ${}^6\text{Li}$ is shown in Fig. 2.3. The hyperfine level spacing of both $2P$ manifolds is close to the natural linewidth ($\Gamma = 2\pi \times 5.87$ MHz), with the complete $2P_{3/2}$ state having a spectral resolution of less than one Γ . Laser cooling experiments applying the standard Sisyphus cooling configuration on ${}^6\text{Li}$ have not yielded sub-Doppler temperatures. There has been a report of successful sub-Doppler cooling for strontium (Xu et al., 2003), which also has a hyperfine splitting that is on the order of the natural linewidth. However, a model of the cooling transition reveals that a key factor for successful cooling in this species is the large magnetic degeneracy of the ground state.

Hamilton et al. (2014) have reported sub-Doppler temperatures for ${}^7\text{Li}$ using a Sisyphus cooling scheme involving a far-detuned molasses. An optical lattice is detuned from both the $2P_{1/2}$ and $2P_{3/2}$ excited states, which are separated in frequency by 10 GHz, by a minimum of 1 GHz, so that cooling effectively only acts on the atomic fine structure. This circumvents any

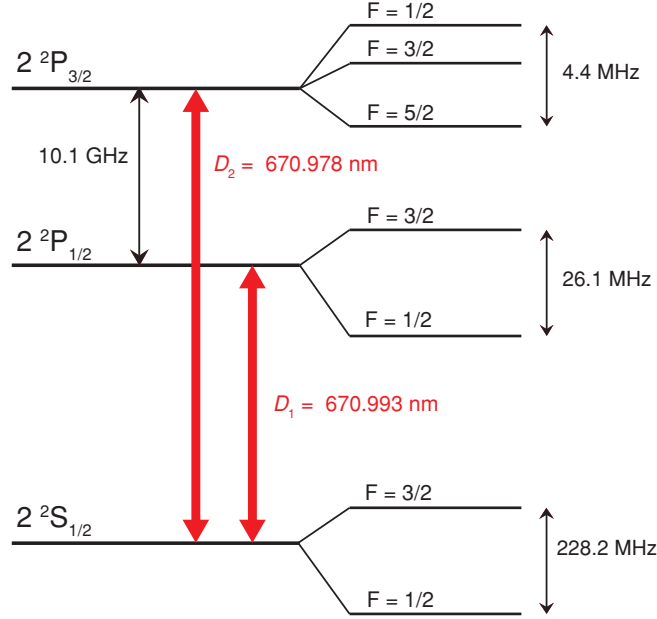


Figure 2.3: Partial level structure of ${}^6\text{Li}$. The hyperfine level spacing of both $2P$ manifolds is close to the natural linewidth ($\Gamma = 2\pi \times 5.87\ \text{MHz}$), with the complete $2P_{3/2}$ state having a spectral resolution of less than one Γ .

complications associated with the involvement of hyperfine states. Temperatures as low as $100\ \mu\text{K}$ were reached with up to 45% of the atoms in the cooled fraction. Moreover, [Hamilton et al. \(2014\)](#) adiabatically release the cloud from the lattice using a gentle ramp-down of the fields, which also has a cooling effect. Adiabatic lattice relaxation has earlier been observed to be effective for lithium ([Chen et al., 1992](#)), so that it is difficult to distinguish the individual contribution of the Sisyphus mechanism to the achievement of the temperatures measured.

2.3 Cooling in a gray molasses

Although standard Sisyphus cooling is not effective for ${}^6\text{Li}$, alternative methods have been found to reach sub-Doppler temperatures. One of these methods is the use of a gray optical molasses, which was first proposed as a theoretical scheme in the nineties by [Shahriar et al. \(1993\)](#), [Grynberg and Courtois \(1994\)](#) and [Weidemüller et al. \(1994\)](#). It was realized experimentally soon afterwards on the D_2 line for cesium ([Boiron et al., 1995, 1996](#)) and rubidium ([Esslinger et al., 1996](#)). Temperatures of roughly six times the single photon recoil energy were reached. The cooling strategy essentially consists of velocity-selective coherent

population trapping (VSCPT) enhanced by a Sisyphus cycle. Hence, this section starts with a description of dark states and their role in VSCPT, continues with the components of the Sisyphus cycle and how it ties together with VSCPT to form the gray molasses, and ends with a discussion of the limits of gray molasses cooling and its operation on ${}^6\text{Li}$ and other species.

2.3.1 Coherent population trapping in dark states

In Section 2.1.2 was described how a bright optical molasses can reduce the temperature of an atomic sample below the Doppler limit. However, resonant dipole-dipole interactions between atoms and photon reabsorption lead to reduced atomic densities and hamper cooling processes (Cooper et al., 1994; Walker et al., 1990). This limitation can be mitigated by using dark states to reduce atom-atom interactions. Dark resonances have been known since 1976 (Alzetta et al., 1976; Arimondo and Orriols, 1976) and play a major role in coherent population trapping (CPT).

The basic principle of CPT is sketched in Fig. 2.4. A three-level atom with Λ -type atomic structure interacts with a light field. The ground states $|g_1\rangle$ and $|g_2\rangle$ are each coupled to the excited state $|e\rangle$ by two counter-propagating laser fields with Rabi frequencies Ω_1 and Ω_2 respectively. When the Raman detuning Δ is zero, the population in the excited state vanishes and no more fluorescence is observed. The atom is said to enter a linear superposition of the two ground states that is decoupled from the light (Arimondo and Orriols, 1976), a so-called dark state. Since this dark state cannot interact with the light field the atomic population cannot be optically addressed and is effectively trapped. In a semi-classical picture, the light-atom coupling can be described by the interaction operator

$$\hat{V} = \hbar\Omega_1/2 |e\rangle \langle g_1| + \hbar\Omega_2/2 |e\rangle \langle g_2| + \text{h.c.} \quad , \quad (2.5)$$

as can be derived from first principles from the dipolar interaction. A new basis can then be

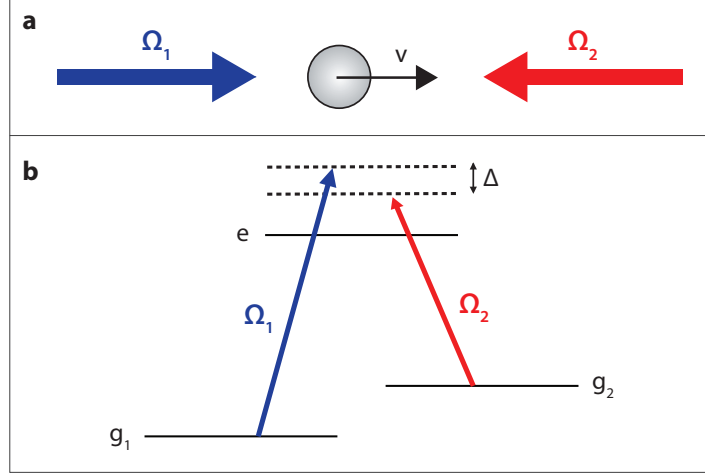


Figure 2.4: (a) An atom moving with velocity v in a light field created by counter-propagating laser beams with Rabi frequencies Ω_1 and Ω_2 respectively. (b) The atomic Λ -structure for coherent population trapping in dark states in this configuration. The ground states $|g_1\rangle$ and $|g_2\rangle$ are each coupled to the excited state $|e\rangle$ by the respective laser fields. When the Raman detuning Δ is zero, the excited state becomes depopulated.

introduced for the ground states, with

$$|\psi_D\rangle = \frac{1}{\Omega} (\Omega_2 |g_1\rangle - \Omega_1 |g_2\rangle) \quad , \quad (2.6)$$

$$|\psi_B\rangle = \frac{1}{\Omega} (\Omega_1 |g_1\rangle + \Omega_2 |g_2\rangle) \quad , \quad (2.7)$$

and $\Omega = \sqrt{\Omega_1^2 + \Omega_2^2}$. The state $|\psi_D\rangle$ is called dark, or non-coupled, since it is unaffected by the light field as shown by $\hat{V}|\psi_D\rangle = 0$. The state $|\psi_B\rangle$ is called bright, or coupled, since it couples to the excited state by $\langle e|\hat{V}|\psi_B\rangle = \hbar\Omega/2$.

2.3.2 Motional coupling and VSCPT

If the atom is assigned a velocity \vec{v} , the laser frequencies experience a Doppler shift of magnitude $\Delta\omega = \vec{k}_i \cdot \vec{v}$, where \vec{k}_i is the wave vector of each of the counter-propagating beams, the magnitude of which is related to the wavelength by $k = 2\pi/\lambda$. If $\vec{k}_1 \cdot \vec{v} \neq \vec{k}_2 \cdot \vec{v}$, the Raman resonance condition is no longer fulfilled and photons can be absorbed. Hence the state $\psi_D(\vec{v})$ is no longer dark for $\vec{v} \neq 0$, and coherent population trapping becomes *velocity-selective*.

In the basis of the coupled and non-coupled states, this can be understood by considering the total Hamiltonian $\hat{H} = \hat{H}_{\text{atom}} + \hat{V}$. The bright and dark state are not eigenstates of the

kinetic part of the atomic Hamiltonian \hat{H}_{atom} and consequently motional coupling is induced that can transfer the atomic population between the two ground states. It can be obtained (Papoff et al., 1992), that the frequency at which the atomic state oscillates between the dark and the bright state is given by

$$\frac{1}{\hbar} \langle \psi_{\text{B}}(p) | \frac{\hat{p}^2}{2m} | \psi_{\text{D}}(p) \rangle = -\frac{2\Omega_1\Omega_2}{\Omega^2} k \frac{p}{m} \quad , \quad (2.8)$$

where $p/m = v$ is the atomic speed. The time that the atom spends in the dark state decreases with the atomic momentum p . Atoms with low speed are kept longer in the dark state, while faster atoms will be transferred to the bright state.

In velocity-selective coherent population trapping (VSCPT), the dark state is populated by momentum redistribution due to spontaneous emission, which causes a cold atom to perform a random walk in momentum space (Aspect et al., 1988). The random walk slows down when \vec{p} decreases and stops when the atom becomes trapped in a small volume around $\vec{p} = 0$, in a velocity dark state that cannot absorb light. The atom can stay in this state for a very long time. VSCPT makes cooling below the recoil limit possible, since the photon scattering rate $R_{\text{F}}(\vec{p})$ vanishes as $\vec{p} \rightarrow 0$ (Bardou et al., 1994). Hence, the single photon recoil energy no longer appears as a fundamental lower bound.

2.3.3 Confinement in momentum space

Since the momentum distribution has no steady-state value, there is no lower temperature limit for sub-recoil cooling by VSCPT. The longer the interaction time, the lower the temperature. However, VSCPT inherently relies on diffusion of the atomic motion to the cooled velocity class by spontaneous emission events. Due to the random nature of this process, a large part of the atoms will diffuse toward higher momentum values where they are tuned out of resonance for effective cooling. Therefore, just a small fraction will finally be cooled below the recoil limit (Bardou et al., 1994). In three dimensions, the efficiency of VSCPT falls off rapidly as a function of velocity, leading to a capture range on the order of the recoil velocity (Shahriar et al., 1993). An improvement to this deficit of VSCPT is to confine the atoms

in momentum space during cooling, by applying a friction mechanism that is able to coexist with VSCPT and that operates under the same conditions (Shahriar et al., 1993; Weidemüller et al., 1994).

2.3.4 A gray Sisyphus cycle

In a gray optical molasses, such a sub-Doppler cooling mechanism is implemented in the form of a Sisyphus cooling cycle, in analogy to the bright molasses. Atomic populations are transferred back and forth between the dark and bright states in the ground state manifold, while kinetic energy is lost by movements uphill in a potential landscape formed by light shifts induced on the bright states.

A schematic representation of the gray molasses scheme is given in Fig. 2.5. An atom with two ground states, one dark state $|\psi_{\text{D}}\rangle$ and one bright state $|\psi_{\text{B}}\rangle$, propagates through a light field in lin \perp lin configuration. The counter-propagating light fields are off-resonant with respect to the atomic transition, and therefore the atom will experience a light shift on $|\psi_{\text{B}}\rangle$, of magnitude δ_{B} . The dark state is not affected by the light field. For blue detuning, the light shift will bring $|\psi_{\text{B}}\rangle$ to a positive energy with respect to $|\psi_{\text{D}}\rangle$, and since δ_{B} is proportional to the intensity and polarization of the field, the light shift potential will be spatially modulated. Like in the standard Sisyphus cooling mechanism, optical pumping from $|\psi_{\text{B}}\rangle$ to $|\psi_{\text{D}}\rangle$ has the highest probability at the top of the light shift potential, due to the local polarization and intensity of the light field. Once in the dark state $|\psi_{\text{D}}\rangle$, the atom can only depart through velocity-induced, non-adiabatic passage of atomic population to the bright state $|\psi_{\text{B}}\rangle$, in other words, through motional coupling (Weidemüller et al., 1994). This closes the Sisyphus cycle. The probability of the non-adiabatic transfer can be calculated with perturbation theory as

$$P = \left| \frac{\langle \psi_{\text{B}}(p) | \frac{\hat{p}^2}{2m} | \psi_{\text{D}}(p) \rangle}{E_{\text{B}} - E_{\text{D}}} \right|^2. \quad (2.9)$$

It is highest in the valleys of the light shift potential, where the energy difference $E_{\text{B}} - E_{\text{D}}$ between the two states is smallest. The probability of motional coupling varies with the square of the atomic velocity. At the end of one cycle, the kinetic energy of the atom will

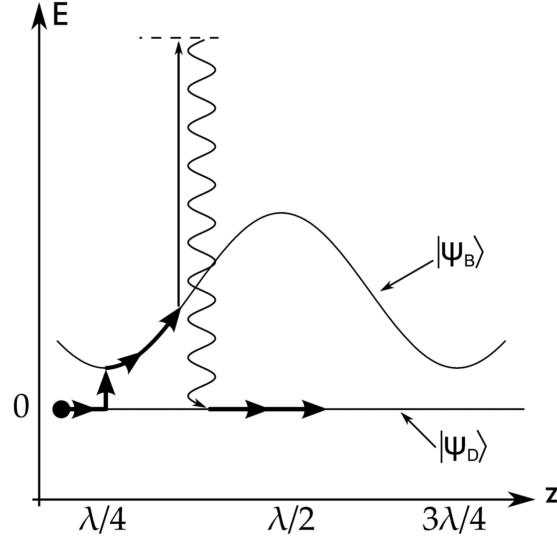


Figure 2.5: The gray molasses cooling scheme. In the presence of a blue-detuned light field, the ground state splits into a dark manifold and a bright manifold with positive energy, shown as $|\psi_D\rangle$ and $|\psi_B\rangle$ respectively. Due to polarization gradients, the bright-state energy is spatially modulated. Kinetic energy is lost when an atom in $|\psi_B\rangle$ climbs a potential hill before being pumped back into the dark state $|\psi_D\rangle$. Motional transfer from $|\psi_D\rangle$ to $|\psi_B\rangle$ is most probable at the potential minima. Figure from [Rio Fernandes et al. \(2012\)](#).

be reduced and therefore the probability of motional coupling also decreases. After many cycles, the atoms will be cold and accumulate in the dark state $|\psi_D\rangle$, resulting in a reduced fluorescence rate and diminished atom-atom interactions.

In this explanation so far, the representation of the gray molasses cooling principle was restricted to a one-dimensional Λ -structure. In general, for an atomic ground state with angular momentum F , gray molasses operate on the $F \rightarrow F' = F$ or $F \rightarrow F' = F - 1$ transitions. For any polarization of the local electromagnetic field, the ground state manifold possesses respectively one or two dark states that are not optically coupled to the excited state by the incident light ([Grynberg and Courtois, 1994](#)). For the $F = 1 \rightarrow F' = 1$ case it was shown that dark states survive in a three-dimensional arrangement of $\sigma^+\sigma^-$ polarized light ([Lawall et al., 1994](#); [Ol'shanii and Minogin, 1991](#)). This is however not for all transitions the case, and in general in three dimensions dark states may be localized in space.

Although VSCPT does not have a lower temperature limit, the Sisyphus cooling mechanism becomes inefficient when the kinetic energy of the atom is too small to climb the potential hill. The associated equilibrium temperature pertaining to the Sisyphus cycle scales with the light

shift as $k_{\text{B}}T \propto I/\delta$. This temperature appears as a limiting temperature for the gray molasses scheme when $T \gg T_{\text{R}}$ (Rio Fernandes et al., 2012). The capture velocity of the molasses is determined by the distance that an atom can travel in the light shift potential during the optical pumping time τ_{p} . For efficient cooling this should be on the order of a wavelength of the cooling light. The capture velocity is thus in the range of $v_{\text{cap}} \sim \lambda/\tau_{\text{p}} = \Gamma_{\text{p}}/k$, where Γ_{p} is the optical pumping rate. For a detuning δ with respect to the cooling transition $\Gamma_{\text{p}} \propto I/\delta^2$ and thus v_{cap} increases with laser intensity (Rio Fernandes et al., 2012). Because the cooling mechanism only works for blue detunings, the atoms in velocity classes outside the sub-Doppler capture range are heated up by Doppler heating.

2.3.5 The gray molasses and ${}^6\text{Li}$

A gray molasses-type strategy led to the first observation of sub-recoil temperatures using VSCPT in three dimensions (Lawall et al., 1995), performed on ${}^4\text{He}$ atoms. In recent years, cold and dense atomic samples were created using gray molasses cooling schemes, on ${}^{40}\text{K}$ (Rio Fernandes et al., 2012), ${}^{39}\text{K}$ (Nath et al., 2013; Salomon et al., 2013, 2014), ${}^{41}\text{K}$ (Chen et al., 2016), ${}^7\text{Li}$ (Grier et al., 2013), ${}^{23}\text{Na}$ (Colzi et al., 2016) and ${}^6\text{Li}$ (Burchianti et al., 2014, 2015; Sievers et al., 2015). The results obtained for lithium and potassium show a robustness of the gray molasses scheme against spectral overlap in the excited hyperfine state of these species. As pointed out by Lam (2016), the atomic transition does not feature explicitly in the gray molasses process, since the accessibility of dark states depends only on the relative detuning of the two laser fields, and not on a detuning to the atomic transition. Therefore, spectral overlap in the excited state would also have less of an impact in a gray molasses cooling scheme. However, in the experiments mentioned above, cooling is performed on the D_1 transition $2S_{1/2} \rightarrow 2P_{1/2}$, which benefits from a better-resolved excited state hyperfine structure. Rio Fernandes et al. (2012) cite this as one of their reasons for choosing this transition. In addition, off-resonant excitations are named as another process besides motional coupling that could lead to transfer of atomic populations out of the dark states.

Sievers et al. (2015) suggest that the gray molasses scheme is inherently more robust against off-resonant excitations than standard sub-Doppler cooling on the D_2 line. They emphasize

that all the dipole-allowed D_1 transitions are “open”, meaning that the probability of inelastic (m_F - or F -changing) photon scattering is comparable to or larger than that of elastic scattering. The consequence of this feature for the cooling mechanism is investigated in a model in which ${}^6\text{Li}$ atoms are subjected to a 1D lattice in $\text{lin}\perp\text{lin}$ configuration and typical cooling parameters. The decay rate γ due to inelastic light scattering of the six dressed ground states of ${}^6\text{Li}$ is studied as a function of the spatially dependent light shifts ϵ . For small light shifts ($\epsilon < 1.5\text{ MHz}$), a positive correlation is observed between ϵ and γ : the larger the light shift of the dressed state, the higher the decay rate from that state. This correlation is found to be crucial for efficient cooling. It leads to accumulation of slow atoms in low-light shift states, and ensures that the decay rate to these states is highest at the top of the light shift potential. It was verified numerically that the correlation between ϵ and γ is robust for more complicated 3D lattices and for other atomic species, and importantly even persists for a vanishing D_1 hyperfine splitting.

In contrast, sub-Doppler cooling on the D_2 lines possesses a significant difference. The $F = I + 1/2 \rightarrow F' = I + 3/2$ transitions, for example, are characterized by both “open” and “closed” transitions, where “closed” is taken to mean that more elastic than inelastic scattering occurs. [Sievers et al. \(2015\)](#) argue that when cooling is performed on the closed transitions with red-detuned light, as in standard Sisyphus cooling, a similar correlation between the light shift and decay rate as described above is established, but only if the closed transitions can be isolated. In the case of small hyperfine splitting, the “open” transitions are simultaneously addressed, which leads to degraded correlations and contributes to the inefficiency of the sub-Doppler cooling. It would be interesting to see this argument tested in a similar study for the D_2 transition that takes all relevant hyperfine states into account. Then truly, a full comparison can be made between the gray molasses and standard Sisyphus cooling.

3 Experimental set-up and techniques

In this chapter the experimental set-up for producing the ${}^6\text{Li}$ gray molasses is described. First an overview of the sequence of the experiment is given, in conjunction with a description of several relevant parts of the apparatus. Then, the laser system that produces the light for the gray molasses on the atomic $2S_{1/2} \rightarrow 2P_{1/2}$ (D_1) transition is described. Initially a new, independent laser set-up was built for this purpose, with its own light source and amplifying medium to increase the available optical power. Eventually however, a simpler, more convenient way of integrating the molasses light into the pre-existing laser system for the atomic $2S_{1/2} \rightarrow 2P_{3/2}$ (D_2) transition was chosen for implementation in the experiment. In this chapter, both set-ups are discussed. The chapter ends with a description of the optical dipole trap and our detection technique for probing the atomic cloud.

3.1 Overview: experimental sequence and laser sources

3.1.1 Sequence of the experiment

For successfully producing a quantum degenerate gas, several steps of cooling and trapping are required. Here, we apply an all-optical approach ([Barrett et al., 2001](#)), whereby the atoms are directly transferred into an optical dipole trap after the laser cooling stages. This approach is favourable because it allows for a short measurement cycle and low experimental complexity. An overview of our set-up is shown in [Fig. 3.1](#), and the individual parts are addressed in this section as they come up in the experimental sequence. A detailed description of the hardware and overall arrangement of the experimental set-up was given by [Gross \(2016\)](#).

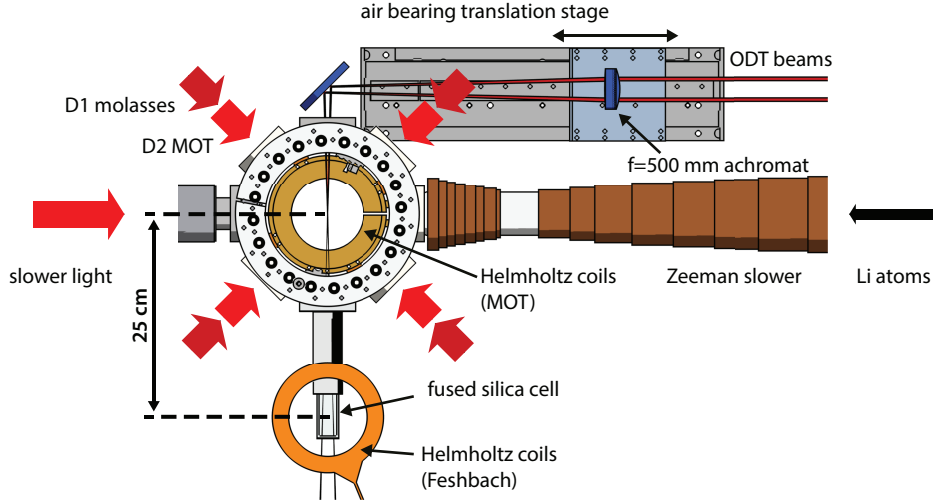


Figure 3.1: Design of the experimental apparatus. An atomic beam of ${}^6\text{Li}$ atoms is Zeeman slowed and Doppler cooled in a MOT on the D_2 transition, followed by sub-Doppler cooling in a D_1 gray molasses. The atoms are transferred into a two-beam, crossed ODT and transported to a glass cell. The position of the air bearing translation stage in this illustration is a mirror image of its exact position in the set-up.

Vacuum system To ensure the successful formation of an ultracold atomic sample, the atoms must be isolated from their surroundings and collisions with high-kinetic-energy particles in the background gas avoided. Therefore, the experiment is performed in a vacuum chamber. Several differential pumping sections ensure a large pressure drop to the main chamber with a background pressure on the order of 1×10^{-11} mbar.

Atom source and Zeeman slower The atom source for the experiment consists of a lithium reservoir, located on the right side of the set-up in Fig. 3.1, which is heated up to beyond the melting point and produces an atomic beam. After passing through the differential pumping stages and a series of collimation tubes, the beam is sent through the central axis of the set-up into the Zeeman slower. Here, the atoms are decelerated by a counter-propagating laser beam, which enters the vacuum system from a viewport on the opposite side of the set-up. The frequency of the slower light is kept on resonance with the atomic transition of the ever more slowly moving atoms by means of a spatially varying magnetic field (Phillips and Metcalf, 1982), produced by a solenoid composed of copper windings.

The D_2 magneto-optical trap When the slowed atoms reach the stainless steel, octagonal central chamber, they are captured in a 3D MOT on the red D_2 transition for the first cooling stage. Quartz viewports allow the propagation of three pairs of counter-propagating beams through the MOT chamber in a molasses configuration. A quadrupole magnetic field is produced by two coils in anti-Helmholtz arrangement to provide a confinement force for the atoms in addition to the frictional force due to the molasses. The light used for laser cooling is brought to the optical table containing the experiment via a single-mode polarization-maintaining optical fiber cluster. This fiber cluster collects the light of the appropriate frequencies from their respective optical paths on a laser table, merges them, and splits into six optical fiber branches on the output side. The six output ports are arranged around the MOT chamber to form the 3D molasses configuration. Directly after the fiber output, the MOT beams are expanded to a $1/e^2$ radius of 0.9 cm. In combination with a moderate magnetic field and a large detuning of the cooling light this yields a large trap volume.

After a loading stage, the D_2 MOT is compressed by simultaneously ramping up the magnetic field gradient, and decreasing the intensity and detuning of the cooling light. The resulting compressed MOT (cMOT) has a higher density and a lower temperature of about $380 \mu\text{K}$. Direct loading of a large number of atoms into the ODT is however still inefficient at this point in the sequence, due to the much smaller spatial size of the ODT compared to the MOT-cooled cloud and temperatures that are on the same order as the ODT trap depth.

The D_1 gray molasses In our approach we therefore employ a second laser cooling stage to achieve better conditions for loading of the optical dipole trap. A gray optical molasses is employed on the D_1 atomic transition. This stage takes typically only 2-3 ms. The quadrupole magnetic field and MOT beams are abruptly switched off, and are replaced by the D_1 molasses beams. Gray molasses cooling is sensitive to the presence of magnetic fields. It is therefore necessary to cancel the magnetic field in the MOT chamber during this cooling stage. Our MOT chamber is equipped with three pairs of coils, each in Helmholtz configuration, in addition to the anti-Helmholtz coils producing the quadrupole field. These bias coils are installed around the chamber along the three orthogonal spatial directions and allow the

magnetic field inside the MOT chamber to be adjusted in three dimensions. They are used to compensate for the earth magnetic field and to apply a bias field. Along the z -axis of the set-up, which is defined to be parallel to gravity, the coils can apply from -3 G up to $+3\text{ G}$, and in the horizontal plane they can apply from -3.5 G up to $+3.5\text{ G}$ at the center of the MOT chamber.

Optical dipole trap for transport to a glass cell After gray molasses cooling, the atoms are transferred into the optical dipole trap. The ODT consists of two high-intensity infrared beams, which are focused by a lens and made to cross at their foci. The focusing lens is placed on an air-bearing translation stage. When used for further cooling to quantum degeneracy, initial evaporative cooling of the atomic cloud takes place in the ODT in the MOT chamber. The trap then transports the atoms to a small, custom-made science cell. The latter is made out of fused silica and is the final destination of the atomic cloud.

3.1.2 The cooling light

The light needed for laser cooling on the D_1 and D_2 lines is generated on a dedicated optical table and is guided through an optical arrangement to acquire the necessary intensities and frequencies. A level scheme showing the transitions used in the experiment is given in Fig. 3.2. For the D_2 MOT, a closed transition for circularly polarized light is present on the $|2 S_{1/2}, F = 3/2\rangle \rightarrow |2 P_{3/2}, F = 5/2\rangle$ line, and thus laser cooling is performed on this transition. However, due to the large spectral overlap in the hyperfine structure of the $2 P_{3/2}$ state, the probability of optical pumping to the $|2 S_{1/2}, F = 1/2\rangle$ ground state is high. Therefore, repumping light is applied on the $|2 S_{1/2}, F = 1/2\rangle \rightarrow |2 P_{3/2}\rangle$ transition. The beams of both frequencies contribute significantly to the cooling process and the distinction between ‘cooling’ and ‘repumping’ light is mostly a convention.

For the gray molasses, cooling is performed on the blue side of the $|2 S_{1/2}, F = 3/2\rangle \rightarrow |2 P_{1/2}, F = 3/2\rangle$ transition. Since the transition is not closed and spontaneous decay to the other ground hyperfine state is allowed, here too a repumper is applied on the $|2 S_{1/2}, F = 1/2\rangle \rightarrow |2 P_{1/2}, F = 3/2\rangle$ transition to pump the atomic population back into the cooling line.

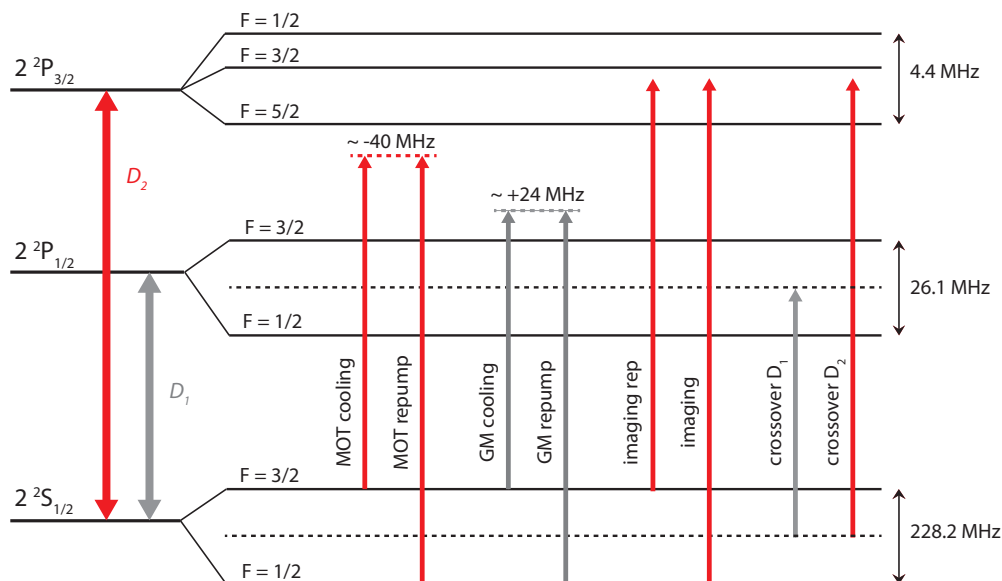


Figure 3.2: Level scheme of the D_1 and D_2 transitions. Arrows indicate the transitions used for the cooling and repumping frequencies in the experiment, as well as the detection light and the atomic cross-over frequency that the laser sources are locked to. Energy level spacings are not to scale.

Again, both the ‘cooling’ and ‘repumping’ beam have a cooling effect on the atomic ensemble. On Raman resonance with the cooling beam, the repumper enhances the gray molasses cooling effect considerably, as is discussed in more detail in Chapter 4.

Laser sources

In general, the laser source chosen for use in this experiment is the external cavity diode laser (ECDL). This is a narrow-linewidth laser source that works with a diffraction grating to provide laser light with a single spatial mode and a tunable wavelength. It can be used to produce laser light with a linewidth narrower than the natural atomic linewidth, so that the atomic transitions can be driven efficiently. However, ECDLs are limited in output power. After grating stabilization, optical Faraday isolation, and passage through beam-shaping optics, typically only a few tens of milliwatts are left in the output beam. When more power is required, the output of the ECDL can be amplified. A common technique is injection seeding of a ‘slave’ diode laser, which yields typically 60-80 mW optical power for near-infrared light. However, if powers exceeding 100 mW are required in a single-mode beam suitable for experimentation in laser cooling and trapping, the only method currently available among the

semi-conductor diode lasers (Kangara et al., 2014) is traveling-wave amplification in a gain element with a tapered waveguide (Mehuys et al., 1992; Walpole et al., 1992). Such a tapered amplifier (TA) achieves high power while retaining the narrow linewidth and stability of the ECDL.

For both the gray molasses and the MOT, enough optical power needs to be present in each of the six beams in the 3D molasses configuration. Therefore, the use of a TA is required for both light frequencies. To produce light on the D_1 wavelength for gray molasses cooling, a set-up was constructed containing an ECDL and a new TA. The design of the TA mount was improved, and the performance of the TA chip, including its gain saturation, was characterized. This set-up is in the following referred to as the ‘independent set-up’. Eventually however, an option to make use of the existing TA in the D_2 optical set-up was put forward. This arrangement allows the set-ups for the D_1 and D_2 frequencies to be integrated, and turned out to be more convenient since the gray molasses light can follow the beam paths to the experiment that are already in place for the MOT light. This set-up is referred to as the ‘integrated set-up’ in the following. Both the independent and integrated set-up are discussed in this chapter, but first the operating principle of tapered amplifiers is described.

3.2 Tapered gain elements

Despite the high cost of TA gain elements, the tapered amplifier is a popular choice for amplification of the optical power in laser cooling experiments. Before they became widespread, other gain elements were used that required more complex experimental set-ups and thorough spectral filtering of the output beam. In this section the operation of the TA is discussed, and some safety recommendations for the protection of the sensitive chip are given.

3.2.1 Laser diode dimensions

In order to maintain a single spatial mode, the transverse dimensions of the optical waveguiding structures of semiconductor laser diodes must be on the order of the wavelength of the light they generate. For such small dimensions the available optical power in CW operation

is limited because of heating, both in the bulk and at the emitting facet (Walpole, 1996). Wider waveguide stripes of several hundred micrometers across can and have been used, but for these broad-area emitting diode lasers (BAL) (Goldberg and Chun, 1988; Goldberg et al., 1993; Shvarchuck et al., 2000) it is difficult to maintain a single spatial mode. Operated as independent lasers, these devices oscillate in very high-order lateral modes, but as amplifiers they can behave well when both anti-reflection coated on both facets and injected with a high-optical-quality input beam of lowest spatial order. However, due to its geometry, the BAL requires an aspect ratio of the input beam on the order of 100 in width to height, and due to its relatively low gain, higher input powers are needed than can be conveniently generated with semiconductor laser sources.

3.2.2 Tapered amplifier properties and operation

The tapered amplifier offers the advantage that the input beam does not need to be of high power, and the output is of high spatial and spectral quality. A semiconductor TA chip is characterized by a laterally tapered gain region in the wafer plane, as illustrated in Fig. 3.3. A short, straight waveguide section of length d_1 is used as a modal filter to excite only the fundamental transverse mode and gives the advantage that a modest input power is sufficient to achieve large energy densities. The beam is focused into the waveguide by a short-focal-length input collimator (IC). As the beam passes through the waveguide and is amplified, the tapered section of length d_2 makes sure that this energy density is kept below the damage threshold (Voigt et al., 2001), while still achieving high output powers. In the direction perpendicular to the wafer plane, the structure geometry remains uniform along the device length $D = d_1 + d_2$, which is typically around 2 mm. The input facet of the tapered gain element has the typical width w_1 of a low power single-transverse-mode diode laser of 5-10 μm , whereas the width w_2 of the output facet of the taper is about 200 μm (Walpole, 1996). If the chip is designed correctly, the size of the input aperture is such that, as a single-mode beam propagates through the chip, it will diffract to exactly fill the tapered region. That way, the beam will grow and propagate towards the large output aperture while remaining near-diffraction-limited.

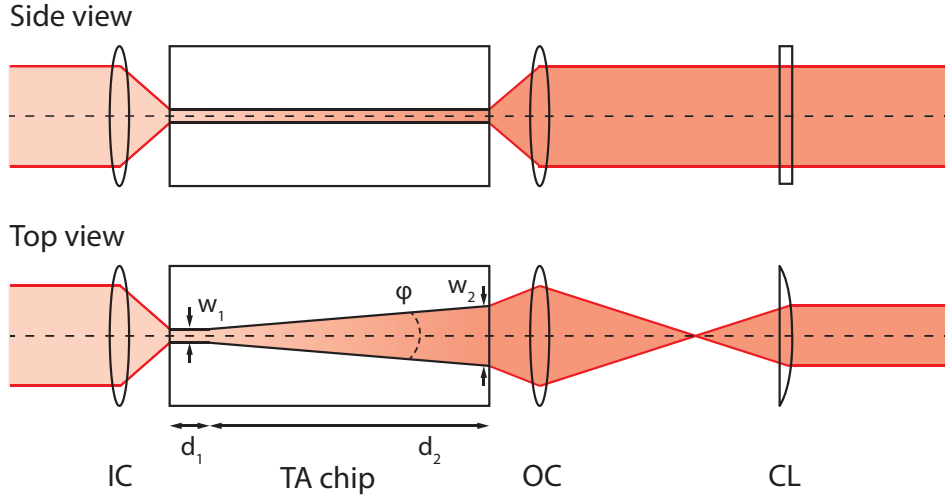


Figure 3.3: Propagation of a beam through a tapered amplifier gain element. The TA chip is shown in top and side view with input collimator (IC), output collimator (OC), and a cylindrical lens (CL) that compensates for the astigmatism. Adapted from Voigt et al. (2001), sizes and distances are not to scale.

An excellent description of the operating principle of the TA is given in Walpole (1996) and Fuchs (2006) and is briefly summarized here. Gain in optical power is obtained by electrically pumping the contact region over the entire area of the tapered profile. If the gain medium is long enough, spontaneous emission is small compared to the stimulated emission initiated by the input beam. The gain region is pumped by a spatially homogeneous current density, and thus the gain along the beam propagation axis is uniform. But since the gain varies with the inverse of the local optical power density, it is not laterally uniform. This means that an incoming Gaussian beam experiences a lower gain along the center of the taper than in the outer regions because the former region gets saturated first. Hence, the edges experience higher gain until the whole wavefront saturates to a nearly uniform intensity, and an increasingly top-hat-like intensity distribution is approached, which is uniform over a certain area and zero outside.

Since the beam expands from the small waveguide and diffracts at the tapered angle, the amplitude and phase will be uniform along the curved wavefronts extending from the aperture, but not along the flat surface of the emitting facet. However, a uniform phase along the surface, and therefore a diffraction-limited beam, can be obtained to a high degree of approximation. In the plane of the taper, the beam emitted by the output aperture seems to

emanate from a virtual source point inside the diode, at a distance of D/n_g behind the output facet. Here n_g the modal index of the transverse waveguide. In the plane perpendicular to the tapered waveguide the beam diffracts at a much higher angle due to the smaller structure size in that dimension. Therefore, the overall output beam is highly astigmatic and, in addition to an output collimator (OC), a cylindrical lens (CL) is needed to correct for the astigmatism, as shown in Fig. 3.3. To calculate the far-field pattern of the TA, the top-hat distribution with a uniform phase at the output facet is considered. One can calculate the lateral power density $P(\phi)$ as a function of the far-field angle ϕ . This is nothing other than the squared Fourier transform of the top-hat distribution,

$$P(\phi) = \frac{\sin^2(\pi w_2 \sin(\phi)/\lambda)}{(\pi w_2 \sin(\phi)/\lambda)^2}, \quad (3.1)$$

with w_2 being the width of the output facet and λ the wavelength of the light. From this equation can be derived that approximately 90% of the beam intensity lies inside the central lobe of the far field pattern.

TAs have been used as sources of frequency-doubling and pumping solid-state lasers (Zimmermann et al., 1996). Apart from the achievable output power, efforts to investigate tapered amplifier systems have addressed the frequency tunability of the narrow-linewidth output (Wandt et al., 1998), simultaneous multiple-frequency generation (Ferrari et al., 1999), spatial-mode properties (Livas et al., 1994), and broadband spectral properties (Voigt et al., 2001).

3.2.3 Protecting the TA

TA chips are notoriously delicate and susceptible to permanent damage by several mechanisms, as described in detail by Kangara et al. (2014). When installing the chip, it should be handled with extreme care so that no other objects touch the chip or the delicate wiring. During operation, the chip must never be exposed to high injection currents without proper temperature regulation, due to the high intensities produced. A thermoelectric cooler should be used to regulate and stabilize the temperature. Moreover, dust particles can be attracted

by the high optical power in an optical-tweezer effect and burned into the faces of the TA chip facets. The accumulation of dust must therefore be prevented by the use of a protective housing. Like for any laser diode, a protection circuit should be installed to prevent the application of a voltage spike, or voltage of wrong polarity across the chip's terminals. And last but not least, a Faraday isolator should be used to prevent optical retroreflections from entering the chip. Any backward-propagating field is amplified and focused by the tapered guide, producing an excessively high intensity at the narrow input facet that could destroy it (Voigt et al., 2001). For this purpose, it is valuable to have access to gain information about the TA chip. For seeding powers that saturate the chip, any retroreflections will at least not be further amplified, so that the risk to the chip is lower.

While operating the TA, one must always be conscious of the presence of the seed beam, since there are two ways in which this beam could be involved in deterioration of the chip. First, when both the injection current and temperature regulation are off, seeding of the chip with 15-20 mW can instantly cause permanent damage. The mechanism of this instant degradation is not fully understood and testing is difficult due to the price of the chip. One may speculate however, that a disconnected TA chip acts like a photodiode and builds up charge on its leads that can electrocute it (Kangara et al., 2014). The other degradation mechanism occurs when the TA chip is operated for long periods of time at high currents without a seed laser. When the TA is not seeded, the electric power that is converted to optical power during seeded operation is now dissipated as heat. Eventually, after several hours, thermal degradation occurs, even when the temperature regulation is on and performing optimally.

3.3 The independent set-up

An illustration of the independent set-up is shown in Fig. 3.4. On a 40 × 45 cm breadboard, a Thorlabs laser diode (HL6545MG) is used in a home-made ECDL to produce red light at $\lambda_{D1} = 670.993$ nm. A Thorlabs 57 dB optical isolator (IOT-5-670-VLP) prevents disturbances to the laser due to back-reflections from surfaces further along the beam path. After grating

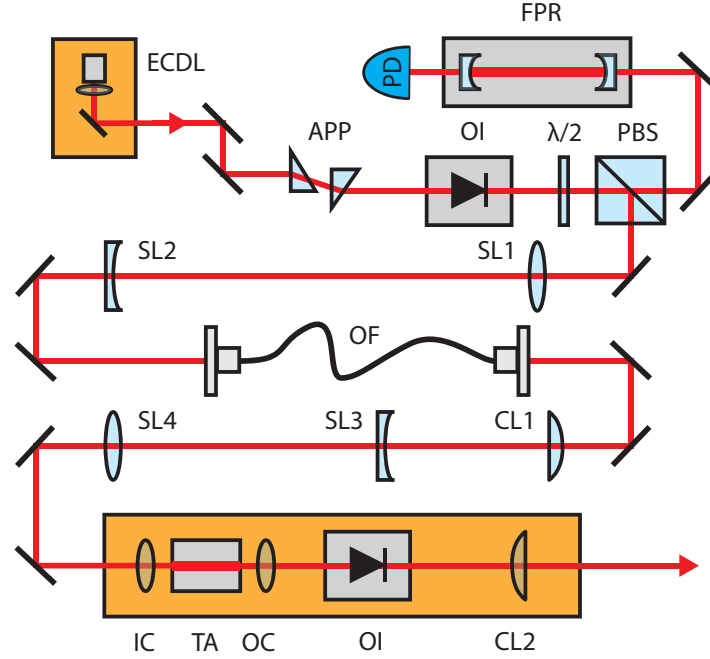


Figure 3.4: The independent set-up for the production of gray molasses light. An ECDL generates light at the D_1 wavelength, which is used to seed a tapered amplifier (TA) chip. The beam passes through a polarization maintaining optical fiber (OF) and several beam-shaping optics such as spherical lenses (SL) and cylindrical lenses (CL) to optimize seeding of the TA.

stabilization and passage through the isolator, 40-45 mW total optical power is available in the beam. A few milliwatts of light are branched off by a polarizing beamsplitter cube (PBS) for use in a Fabry-Pérot resonator, which serves to monitor the quality of the emitted electromagnetic modes. The remainder of the beam is used for seeding the tapered amplifier. The ECDL output is coupled into a single-mode, polarization-maintaining optical fiber (Thorlabs Inc., P3-630PM-FC-2) to get a measure of the effective gain achieved by the TA, in a method that is described later in this section. To optimize the input coupling into the fiber, use was made of an anamorphic prism pair (APP) to circularize the beam, and a lens pair to decrease the beam size. When operated on its own, the TA emits amplified stimulated emission (ASE) in both directions. The backwards traveling beam can be used as an aid in coupling the seed beam into the amplifier, by mode-matching the two beams as much as possible. For this purpose, a telescope lens pair is used to change the size and divergence angle of the beam, and a cylindrical lens produces the required elliptical beam shape.

The TA is a commercial semiconductor chip by Eagleyard Photonics, model EYP-TPR-

0670-00500-2003-CMT02-0LAB. According to the manufacturer's data sheet the output power of the TA reaches 0.5 W at a maximum forward current of 1.0 A with proper injection from a seed laser. The wavelength tuning range at 25 °C is from 665 to 675 nm. This particular chip has a slightly different design compared to conventional TA chips, which are anti-reflection coated on both facets so that they act as an amplifier only. In the case of our chip, the facet on the tapered side has medium reflectivity. This allows the formation of an external cavity with a rear-positioned holographic grating, so that the chip can be operated as an ECDL in Littrow configuration with high optical output power and tunable emission wavelength (Eagleyard Photonics, 2016). However, this aspect of the chip design is not made use of in our application and the chip is only operated as an amplifier.

The optical fiber transmits 60% of the ECDL output, so that in the end, up to 25 mW is available in the seed beam directly in front of the TA at a wavelength of 671 nm. A 57 dB optical isolator (Thorlabs Inc., IOT-5-670-VLP) prevents damage to the chip due to back-reflections. The isolator is rotated at a small angle with respect to the beam path, so that reflections off its front facet will not be reflected directly back into the chip. Due to the isolator transmission the TA output experiences considerable loss. Taking small reflection losses due to the lens surfaces also into account, the useful output power is estimated to be about 70% of the total power emitted by the TA. In the remainder of this section, all quoted powers are as measured behind the optical isolator and cylindrical lens. The TA was operated within the specifications of the manufacturer's data sheet, which recommends that the optical power at the output facet does not exceed 500 mW.

3.3.1 Design of TA mount

The commercial TA chip comes in a C-mount package and is fixed with a central screw onto a shoulder on a copper base. An illustration of the TA mount design is shown in Fig. 3.5. Copper is chosen for its excellent heat conductivity. The TA chip is installed onto the shoulder part of the copper base, with a collimating lens directly behind and in front of the chip. The collimating lenses are mounted in cylindrical tubes that are held in place by tube holders. For this tapered amplifier system, the design of the TA installation was modified slightly as

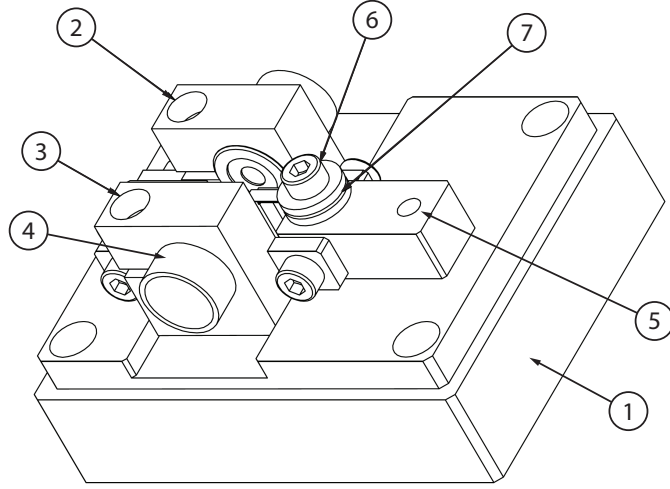


Figure 3.5: Design of the copper base and components for mounting the TA chip. The numbers 1-7 refer to: (1) copper base with central shoulder for mounting the TA chip; (2) Lens tube holder for input collimator; (3) Lens tube holder for output collimator; (4) Lens tube for collimating lens; (5) Tapped hole for placement of cathode connection; (6) Nylon screw for fixing anode connection washer; (7) Conductive washer for fixing the anode connection, crimp terminal not shown.

compared to the standard design that was used in our group. The main motivation was to improve the ease of adjusting the position of the collimator lenses in the vertical direction, while ensuring that their position remains highly stable once fixed. Since the quality of the output beam is directly dependent on correct seeding of the chip and collimation of the output beam, being able to carefully position the collimating lenses is quite crucial. Previously, adjusting the vertical position of the lens was done by taking out the tube holders and filing a short section off the bottom. In the new design, the holders are fixed to the shoulder part of the copper base by screws. The design of the holder is such that some freedom of movement is allowed around these screws, so that displacement of the lens in both the vertical and horizontal direction is facilitated. Adjusting the lens position along the propagation axis of the light is achieved by moving the lens tube inside the holder.

The mounting wire of the TA chip is its anode and is connected to the chip by delicate bond wires, while the rest of the C-mount bulk forms the cathode. When the chip is installed, the mounting wire is contacted with a conductive washer with crimp terminal at position (7) in Fig. 3.5. The conductive washer is isolated from the copper base by means of a nylon washer and the mounting wire is fixed in place on top of the conductive washer by another

nylon washer and nylon screw. Note that with this design, no soldering on the chip mounting wire is needed to establish electrical contact. The negative lead of the current controller is soldered onto the crimp terminal of the conductive washer, so that electrical contact with the chip is established. Another conductive washer with crimp terminal is installed at position (5) in Fig. 3.5, and fixed using a conductive screw. The chip cathode makes direct contact with the copper base, so that this washer can be used to attach the positive lead of the current controller. For the temperature regulation, a small hole is made in the copper base near the chip location. A thermistor is inserted and sends a signal to the PID regulator. A thermoelectric cooler is installed underneath the copper base and is used to stabilize and adjust the temperature of the chip.

As mentioned, the new design of the TA mount and lens tube holders improves the ease of adjustment of the input and output collimators. The use of washers with crimp terminals at the copper shoulder provides better access to the electrical connections without the need to solder onto the chip, which is an advantage during the installation and decreases the risk of damage to the chip. In exchange, the mounting wire needs to be cut to shorten it, and bent slightly to meet the conductive washer. Finally, a major change with respect to the previous design is the one-piece copper base. Previously, a flat copper base and gold-coated, separate shoulder for mounting the chip were used. The new design improves the thermal conductivity, but has as a disadvantage that copper is damage-prone. Features on the shoulder that are much used during chip installation, such as tapped holes for screws, will wear out more quickly.

3.3.2 Fiber coupling

A polarization-maintaining, single-mode optical fiber was used in the set-up, transmitting 60% of the ECDL output in the forward direction. In a convenient trick, the fiber transmission in the backwards direction of the ASE light from the TA also provides some information. Loss occurs at the TA-fiber interface due to shape mismatch. The shape of the beam emitted from the TA facet is elliptical and the fiber aperture forces this beam into a Gaussian profile. The fraction of the light that does not fit this mold is lost. Because the optical path is reversible, the same holds true in the forwards direction. An equal fraction of the Gaussian

seed beam from the fiber output will not fit the mold imposed by the single-mode TA input. Hence, the backwards emitted TA beam can be used to choose the optimal mode-matching optics for coupling the seed beam into the TA. The combination of optics that gives the highest backwards fiber transmission will optimize seeding of the chip. Moreover, the fraction of intensity that still does not couple properly into the chip is not amplified. Then, with knowledge about the fiber transmission of the backwards emitted TA beam at optimal mode-matching conditions, a good estimate can be obtained of the effective gain of the TA chip.

In practice, this technique did not prove very convenient. Only about 8% of the backwards emitted TA beam was transmitted by the fiber. Little difference was observed when trying out various combinations of mode-matching optics, even though the total power of the TA output was very sensitive to the different lens combinations. Eventually therefore, mode-matching was performed by mimicking the beam shape of the fiber output to the backwards emitted TA beam, and fine-tuned by observing the effect of different lens positions on the TA output power. The exact reason for the low fiber transmission of the backwards emitted TA beam is uncertain. It seems that the TA emission when unseeded is not single-moded and the majority of the beam is lost at the fiber input terminal.

3.3.3 TA operating behaviour

When the TA receives no seed input, it operates as a laser diode. As the injection current I_{TA} is increased from zero, the optical output power shows the lasing threshold at around 0.7 A, as shown in Fig. 3.6(a). Only amplified stimulated emission (ASE) is present that reaches a maximum intensity of 25 mW in the forwards direction. The beam profile of the unseeded light differs from that of the amplified output beam, especially in the horizontal plane, and is not well collimated by the TA output couplers. When seeded, the far-field amplified output beam looks like a square, bright spot of roughly uniform intensity. The beam profile shows a less bright, vertical stripe that divides the beam into two lobes. By fine tuning of the mirrors in front of the TA, this stripe can be moved horizontally. The central wavelength of the emission spectrum increases with temperature with a specified slope of 0.25 nm/K, which is typical for GaAs-based semiconductor lasers. When a seed beam is present, the temperature

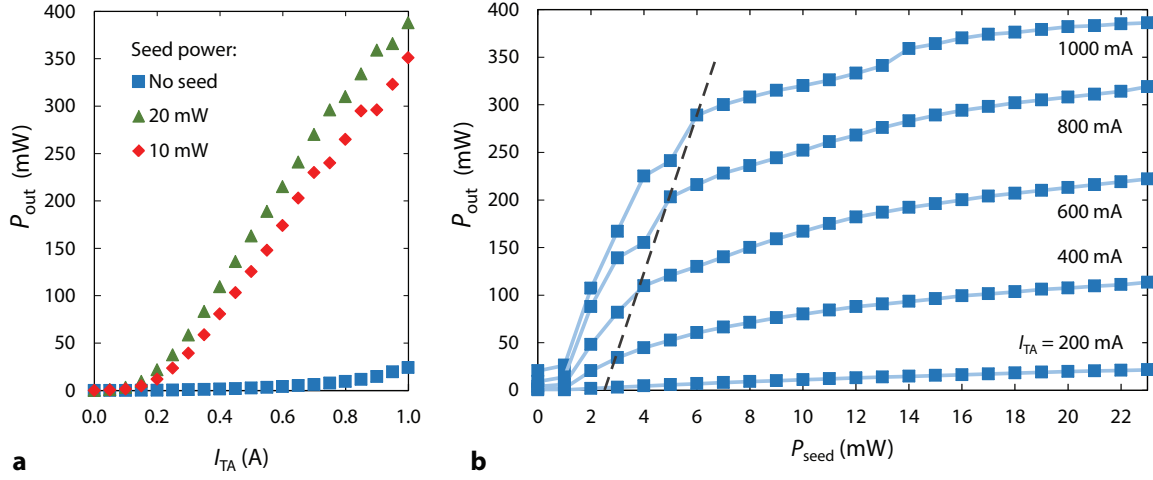


Figure 3.6: The TA output power P_{out} versus (a) injection current I_{TA} and (b) seed power P_{seed} . The dashed line highlights the trend that the seed power at which the chip saturates increases with injection current.

of the chip can be adjusted to shift the gain profile towards the seed wavelength. This leads to a better suppression of the ASE background in the emission spectrum (Voigt et al., 2001). Additionally, the chip temperature also affects the output power of the TA. For this chip, the emitted power exhibited local maxima as a function of the temperature, and we choose to operate the TA at one of these.

The gain behaviour of the TA chip is displayed in Fig. 3.6. In panel (a) the output power is plotted as a function of injection current I_{TA} , as was measured at 10 and 20 mW seed power. It is evident that the lasing threshold is lowered considerably when seeded. At 20 mW the amplifier is well saturated. This is evident from panel (b) where the output power is plotted against the seed power, at varying injection currents. As is indicated by the dashed line, the seed power at which saturation occurs increases with the injection current. For this reason, it is recommendable to use low injection currents when operating the chip without an optical isolator, which could be necessary e.g. when collimating the output beam when the chip has just been installed. In this regime, low seed powers already saturate the TA, and the risk of amplification of back-reflections is reduced.

At the maximum recommended operating current of 1.0 A, we observe that only 14 mW seed power is needed, after which increasing the seed power does not lead to a significant increase

in output power anymore. At this value of the current, a maximum TA output power of 390 mW was observed. At the high injection currents of 0.8 A and 1.0 A some irregularities in the gain curves in panel (b) are observed. These variations in the output power could be accounted for by small fluctuations of the chip temperature, caused by the high injection current and varying seed powers.

3.4 The integrated set-up

Despite the new TA and the independent set-up functioning satisfactorily, transportation of the gray molasses light to the experimental table would present a certain effort. This includes provisions for frequency tuning and switching as well as overlapping the beams with the existing MOT beams. The most convenient way is to make use of the same optical fiber cluster that was described in Sec. 3.1, so that the gray molasses light perfectly overlaps with the MOT-cooled cloud without the need for any further alignment. A method to achieve just that was found and involves the use of the TA that is already present in the D_2 set-up, so that the independent set-up was abandoned.

In the integrated set-up, the D_1 light shares the same optical table and a large part of the optical arrangement with the D_2 set-up, as is shown schematically in Fig. 3.7. Both the D_1 and D_2 ECDLs are homemade, and are furnished with respectively a Thorlabs HL6545MG laser diode and a TOPTICA Photonics AF, LD-0670-0025-AR-2 anti-reflection coated laser diode. Some 10 mW optical output power is branched off from each ECDL and directed toward a spectroscopy cell containing ^6Li atoms. The lasers are stabilized to the respective atomic transitions using Doppler-free frequency modulation (FM) spectroscopy. Electro-optic modulators (EOMs) are used to phase modulate the light beams, which are split into a pump and a probe beam and sent through the cell in a counter-propagating configuration as shown in Fig. 3.7 for D_2 . The transmitted probe beam is detected by a photodiode and the signal contains information about the absorption frequency of the phase-modulated beam. It is demodulated to generate an error signal, which is used to lock the frequency of the lasers to the respective atomic cross-over features (see Fig. 3.2). For the D_2 light, this results in a blue-

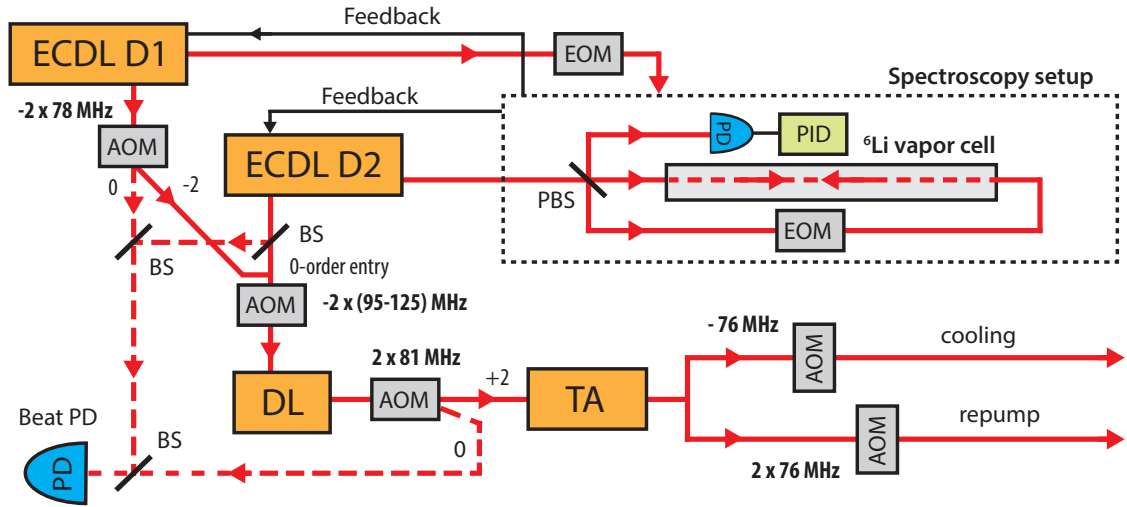


Figure 3.7: The integrated set-up for the production of MOT and gray molasses cooling light. FM spectroscopy is used to lock the ECDLs to the respective atomic frequencies. The arrows connecting the D_1 ECDL to the spectroscopy set-up indicate another beam path and feedback loop to frequency-stabilize the light in the same spectroscopy cell. The D_2 and D_1 beams seed the slave diode laser (DL) in turn, and from that point onwards follow the same path to the experiment. A beat system is used to monitor the seeding of the DL at each instant in the experimental sequence.

detuning of 114 MHz with respect to the cooling transition $|2S_{1/2}, F = 3/2\rangle \rightarrow |2P_{3/2}\rangle$. The frequency of the stabilized D_1 laser is blue-detuned with respect to the $|2S_{1/2}, F = 3/2\rangle \rightarrow |2P_{1/2}, F = 3/2\rangle$ transition by 101 MHz. Due to the distinct absorption frequencies, the beams on the two D-lines can coexist in the same spectroscopy set-up, but care must be taken that the beams of the two frequencies do not cross inside the cell, so that clean error signals can be obtained. In the following, the remainder of the set-up is separately described along with the way it is used for the MOT and the gray molasses cooling stages.

3.4.1 The MOT laser system

A part of the D_2 ECDL output is frequency shifted with an acousto-optic modulator (AOM) in double-pass configuration and the beam is used to seed a slave diode laser, which has an output power of about 70-80 mW. The frequency of the AOM can be externally controlled and this function is used to tune the laser frequency within a range of 60 MHz, about ten times the natural linewidth, without affecting the output power. The light of the slave DL seeds a tapered amplifier, which amplifies a seed beam of 25 mW in a single pass to up to 300 mW. The output beam is split into a cooling and a repumping fraction, which are separated in

frequency by 228 MHz, the ground state hyperfine splitting. In addition to adjusting the frequency of the light, the AOMs can be used to quickly switch the beams on and off, and to set the optical power in each beam. A polarization-maintaining optical fiber (Evanescence Optics Inc.) with two input and six output ports is used to combine the two frequencies and transport the light to the experiment. In total 7-9 mW is available in each of the six beams, with a power ratio between cooling and repumping light that can be regulated.

3.4.2 Integration of the gray molasses light

The D_1 light enters the set-up through a backdoor at the first double-pass AOM in the D_2 set-up. In the first pass of the D_2 light through the AOM, the non-refracted, zero-order beam is branched off via a prism. The beam of D_1 light, coming in from the opposite direction, is overlapped with this zero-order beam and thus enters the AOM from the other side. During the MOT cooling stage this light is blocked, but at the end of this stage the AOM is quickly switched off and the D_1 light is allowed to pass through without being refracted. From there, it is used to seed the slave diode laser, and follows the same beam path through the TA to the experiment table. The requirements of the gray molasses cooling scheme for the polarization of the counter-propagating laser beams are identical to those for the D_2 MOT, and therefore the same optical components can be used on the experiment side. Hence the diameter of the gray molasses beams is also identical to that of the MOT beams. Another AOM in double-pass configuration is used right after the D_1 ECDL output, to enable fast switching and to shift the frequency of the light to the required overall detuning to the blue side of the cooling transition.

The beat system

Since the frequencies of the D_1 and D_2 atomic transitions are so similar (they are separated by only 10.1 GHz), the slave diode laser can be injection seeded by either. However, the different light frequencies match the laser diode cavity modes at different values of the DL operating current. To quickly switch between the two, as is done when progressing from the MOT cooling stage to the gray molasses, a current modulation pulse is sent to the DL. Because

gray molasses cooling is only applied for a few milliseconds, a single modulation current value is typically sufficient. Temperature fluctuations due to the sudden change in injection current are negligible for timescales up to at least 10 ms, as was observed by varying the duration of the gray molasses phase.

To monitor whether the DL is truly following the D_1 frequency for the entire duration of gray molasses cooling and how quickly it does so, a beat system was set up. Unused zero-order light beams from both the AOMs after the D_1 ECDL and after the DL are branched off and overlapped onto a photodiode, as is indicated by the dashed beampaths in Fig. 3.7. When the DL follows the frequency dictated by the ECDL, the combined light waves interfere and form a beat, which is observed as an increase in the amplitude of the photodiode signal. Using this method, the response of the slave DL can be monitored during the experiment and, if necessary, be acted upon accordingly, e.g. by adjusting the modulation current to the DL. When the experimental cycle is completed, the atomic ensemble is imaged using laser light at the D_2 frequency. For this purpose, the source for seeding the slave laser needs to be switched back to the D_2 ECDL. To monitor that this happens correctly and quickly enough, another beat is produced, this time between the D_2 ECDL and slave laser outputs.

The beat method is a very convenient tool for optimizing fast switching between the two ECDLs as source for seeding the slave laser, and is a technique that to our knowledge is not being used for this purpose elsewhere. In practice we see that the slave can switch very quickly between the two light sources, with a gap of only about $30 \mu\text{s}$ in between during which it is not seeded.

3.5 The optical dipole trap

In our all-optical approach (Barrett et al., 2001), the cooled atoms are transferred directly from the gray optical molasses into an optical dipole trap (ODT). In the scope of this thesis, we mainly test the capture efficiency of the atoms from the gray optical molasses into the ODT, to assess the suitability of this sub-Doppler cooling method as an intermediate step in the experimental sequence for producing degenerate quantum gases, or performing

photoassociation experiments in the ODT.

The fiber laser The high-intensity laser light for the ODT is produced by a single mode 1070 nm fiber laser (IPG, YLR-50-1070-LP), with a total optical output power of 50 W. This wavelength was chosen because it is far from resonant with any atomic transition in ${}^6\text{Li}$, and therefore all Zeeman states of the ground state experience the same trapping potential (Grimm et al., 2000). Additionally, 1070 nm is close to a magic wavelength for the atomic $2S_{1/2} \rightarrow 3P_{3/2}$ transition (Safronova et al., 2012), which was previously used in our experiment for cooling in the UV MOT. The differential ac Stark shift induced on the atomic energy levels would be small in the presence of UV light and allow continued laser cooling in the UV MOT while loading the ODT. The latter advantage is absent for trapping from the gray molasses-cooled cloud. Nevertheless, an overlap period of gray molasses and optical trapping can still enhance the loading efficiency, as discussed in Chapter 5.

The crossed ODT The high-intensity fiber laser output is split equally into two beams to produce the crossed ODT. Each of the beams is focused through an AOM and expanded to a $1/e^2$ beam size of 2.6 mm. A periscope brings the two parallel beams to the air bearing translation stage (Nelson Air Corp, Atlas-101-310-HD Stage), where they pass through a 500-mm focal length lens that both focuses the beams and crosses them under a small angle of 3° at the position of the foci (see Fig. 3.1). The measured waists of the ODT beams at their foci are respectively $65 \mu\text{m}$ and $67 \mu\text{m}$ (Gross, 2016). Initially, the beams are crossed at the center of the MOT chamber for maximum overlap with the laser cooled atomic cloud. The linear translation stage enables fast and smooth motion of the lens with high reliability. In this manner, the axial position of the trap is moved to the center of the glass science chamber. To avoid interference effects, the two beams have orthogonal linear polarizations and differ in frequency by 220 MHz.

Compared to a single-beam ODT for use in optical transport (Gustavson et al., 2001; Léonard et al., 2014; Zimmermann et al., 2011), the crossed configuration (Adams et al., 1995) leads to a significant enhancement of the axial trap frequency, and an increased trap depth. This allows transport to be achieved without the need for a very small beam waist,

and hence a large trapping volume is available for overlap with the cloud produced in the laser cooling stages. The advantage of a crossed configuration in our set-up is evident from a comparison with calculated values for a single-beam ODT with identical optical power and axial confinement, as was performed by Gross (2016). The beam waist would have to be reduced to $36\ \mu\text{m}$, and the resulting scattering rate and aspect ratio of the trap would be tripled as compared to the crossed ODT.

Intensity stabilization As was described by Gehm et al. (1998), fluctuations in the optical power of the beams can lead to parametric heating of the atomic cloud. Therefore, the power of the optical trapping beams is actively stabilized through an intensity stabilization mechanism. A small portion of each ODT beam is branched off and directed to a photodiode followed by a logarithmic amplifier. A high-bandwidth PID regulator uses the produced signal to provide feedback to the applied RF power for the AOMs. In this way, the optical power in the ODT beams can be stabilized with high precision and regulated from a few milliwatts to a maximum of 23 W per beam.

3.6 Detection

Another branch of the D_2 -frequency light, not shown in the set-up in Fig. 3.7, is used to produce the light for absorption imaging. With this detection method, the atomic ensemble can be probed and its thermodynamic properties obtained and studied (Ketterle et al., 1999). In absorption imaging, the cloud is exposed to resonant or near-resonant light that is partially absorbed and analyzed with a camera. This provides information on the density distribution and the total number of atoms.

A low-intensity, collimated laser beam is directed onto the atoms and partial absorption leads to a shadow in the center of the beam. The intensity profile I_{abs} of the partially absorbed laser beam that is recorded on the CCD chip can be related to the optical density $\text{OD}(x, y)$ of the cloud. The total atom number N is determined by integration:

$$N = \frac{1}{\sigma} \int \text{OD}(x, y) \, dx dy \quad . \quad (3.2)$$

Here σ is the photon absorption cross-section, which for imaging of multilevel atoms has to be corrected with a normalization factor, in order to account for the different transitions that are accessed. To obtain the full density profile $n(x, y, z)$ of the atomic cloud, a second image from a different direction is required. However, the atomic cloud is often a cylindrically symmetric ellipsoid, so that it is possible to reconstruct the three-dimensional density profile from one absorption image.

The temperature of the atomic cloud can be determined through time of flight imaging. Assuming a classical gas well above temperatures necessary for quantum degeneracy, the velocity distribution of the atoms in the confined cloud is considered to be Maxwellian. When an atomic ensemble is suddenly released from the cooling and trapping forces, it expands according to this distribution. If the cloud initially followed a Gaussian density profile, its density distribution during expansion remains Gaussian (Weiss et al., 1989), and the $1/e^2$ cloud radius $R(t)$ evolves as

$$R^2(t) = R^2(0) + \frac{4k_B T}{m} t^2, \quad (3.3)$$

as a function of the expansion time t . Here $R(0)$ is the initial radius of the Gaussian cloud at $t = 0$, and m is the atomic mass. In the experiment, a series of measurements of the cloud radius at different expansion times is taken. By fitting the data to Eq. 3.3, the temperature T of the cloud and its initial size are extracted.

After both the MOT and the gray molasses cooling stage, we image with a beam that passes vertically through the MOT chamber, along the direction of gravity. A relay telescope translates this image to a position outside the vacuum set-up, where it is projected onto a CCD camera by means of a camera objective. This objective allows the magnification to be varied depending on the measurement, without other changes to the set-up being required. A description with an illustration of this imaging technique can for example be found in Dieckmann (2001). The relay telescope consists of two $f = 100$ mm lenses and the images are recorded with a low-cost 1294×964 pixel CCD camera (Stingray, Allied Vision Technologies) with a pixel area of $3.75 \times 3.75 \mu\text{m}$.

A magnetic field of about 1-2 G is applied along the vertical direction, parallel to the imaging beam, to define a quantization axis for the atoms. The majority of the measurements on the gray molasses have been performed with σ_+ -polarized light resonant with the $|F = 1/2\rangle$ ground hyperfine state. At the end of the optical cooling stage, the atoms are optically pumped to this state by switching off the repumping light a fraction of a millisecond earlier than the cooling light. Even so, also an imaging repumper was installed that is resonant with the $|F = 3/2\rangle$ ground hyperfine state. This beam is directed horizontally through the MOT chamber and continuously pumps the atomic population back into the imaged state, so that all atoms are observed during detection. The imaging repumper typically adds 15-20% to the total atom number measured.

4 The gray optical molasses

In this chapter, the sub-Doppler laser cooling scheme for ${}^6\text{Li}$ based on a gray optical molasses is described. First, a short overview is given of the statistical quantities by which we assess the quality of our cold atomic clouds during the various stages of the experiment. Then follows a description of the MOT that is applied on the D_2 atomic transition to pre-cool the atoms for capture in the gray molasses. The molasses rapidly reduces the temperature of the cloud and enhances the phase-space density by an order of magnitude. Our characterization of the gray molasses is presented. Canceling residual magnetic fields proved to be crucial for effective cooling, and was a challenge in our set-up due to the presence of long-lived eddy currents. Furthermore, some complications were encountered during the interpretation of time-of-flight measurements to extract the cloud temperature after the molasses phase. These challenges are discussed in the following. Finally, the results that optimize the phase-space density of the gray molasses are discussed and compared with those obtained in other studies.

4.1 Analyzing cold atomic clouds

An important property of a cooled and trapped atomic cloud that is commonly used as a figure of merit and to compare results across different experiments is its density in real space and in phase space. It is therefore relevant to obtain some knowledge of the density distribution of the confined gas during the various experimental stages. Here, the gas is described in the classical limit, where quantum statistical effects only have marginal implications and interatomic interactions are not accounted for (Walraven, 2014). This description is valid provided that the gas is dilute enough. This condition can be formulated as $nr_0^3 \ll 1$, where n is the density of the gas and r_0 is the range of the interatomic potential $V(r)$. This potential,

under the influence of which the atoms collide, is assumed to be short-range, which implies that the interaction energy can be neglected for $r > r_0$.

The confinement of the atoms can often be assumed to be provided by a harmonic potential defined by $U(\vec{r}) = \sum_{i=1}^3 \frac{1}{2} m \omega_i^2 r_i^2$. In this equation ω_i denotes the angular trap frequency along the spatial direction r_i , with $i = x, y, z$. By calculating the canonical partition function of the classical gas in this potential, the phase space occupancy $f(\vec{r}, \vec{p})$ can be derived, which corresponds to the number of atoms within a box of size $2\pi\hbar$ around the point (\vec{r}, \vec{p}) . By integrating over the momentum space, an expression for the spatial density distribution can be obtained, as (Walraven, 2014)

$$n(r) = n_0 \prod_{i=1}^3 e^{-(r_i/R_i)^2} \quad . \quad (4.1)$$

Here the peak density n_0 and the $1/e$ radii R_i of the atomic cloud are given by

$$n_0 = N \left(\frac{m \bar{\omega}^2}{2\pi k_B T} \right)^{3/2} \quad \text{and} \quad R_i = \sqrt{\frac{2k_B T}{m \omega_i^2}} \quad . \quad (4.2)$$

where $\bar{\omega} = (\omega_x \omega_y \omega_z)^{1/3}$ is the geometric mean of the trap frequencies, k_B is Boltzmann's constant, and m is the atomic mass. For a given trap frequency, the size of the confined gas therefore only depends on the ensemble temperature T , and R_i is often referred to as the thermal radius of the cloud. In our experiment, we directly measure the cloud radii to infer the peak density. Absorption imaging with the imaging beam propagating along z gives us information about the radii in the (x, y) -plane. The cloud shape is often a cylindrically symmetric ellipsoid, so that we set the cloud radius along z to be equal to one of the horizontal radii. Converting to $1/e^2$ radii we obtain for the peak density

$$n_0 = \frac{N}{(\pi/2)^{3/2} R_x R_y^2} \quad . \quad (4.3)$$

The density in phase space at the center of the trap follows from $f(\vec{r}, \vec{p})$ and is given by

(Walraven, 2014)

$$\rho = N \left(\frac{\hbar\bar{\omega}}{k_B T} \right)^3 = \Lambda_T^3 n_0 \quad , \quad (4.4)$$

where $\Lambda_T = \frac{h}{\sqrt{2\pi m k_B T}}$ is identified as the thermal de Broglie wavelength (Bowley and Sánchez, 1999). The phase-space density can then be calculated from the measured peak density and the temperature of the cloud. For $\rho \ll 1$, the interparticle spacing is much larger than the size of the atomic wave packet and the gas can be described in the classical limit (Walraven, 2014).

4.2 The D_2 magneto-optical trap

Due to the blue-detuning of the cooling light that is required for the gray molasses cooling mechanism and its limited capture velocity range, the gray molasses cannot directly capture atoms from a Zeeman-slowed atomic beam. A pre-cooling stage is necessary before sub-Doppler cooling on the D_1 transition can be employed. Therefore, our cooling sequence begins with standard Doppler cooling on the D_2 transition at 671 nm, where ${}^6\text{Li}$ atoms are loaded into a magneto-optical trap.

Magneto-optical trapping The scattering force due to counter-propagating light beams in a three-dimensional optical molasses configuration can cool an atomic cloud, but cannot confine it, since the atoms are able to diffuse out of the intersection region of the six laser beams. In order to confine the atoms, a quadrupole magnetic field is added, which, in collaboration with the light fields, provides a spatially dependent force. The principle of magneto-optical trapping relies on the Zeeman shift that is induced in the atomic hyperfine states in the presence of an external magnetic field. For a spatially varying magnetic field, the magnitude of the Zeeman shifts induced in the different m_F states varies with position. A light field with the appropriate circular polarization σ_- , which drives $\Delta m_F = -1$ transitions, or σ_+ , which drives $\Delta m_F = +1$ transitions, and a red detuning, produces a restoring force directed towards the center of the quadrupole magnetic field that grows in magnitude as the distance from the trap center is increased.

The first magneto-optical trap was realized with sodium atoms by [Raab et al. \(1987\)](#), and a MOT was successfully applied to lithium for the first time by [Lin et al. \(1991\)](#). A temperature of $350 \pm 40 \mu\text{K}$ was achieved, which is about twice the Doppler temperature of $141 \mu\text{K}$. The measurements were in good qualitative agreement with the detuning dependence of the temperature as predicted by Doppler theory. In later experiments based on different laser sources and trap geometries, similar temperatures were observed ([Ritchie et al., 1994](#); [Schünemann et al., 1998](#)).

MOT loading In the initial phase of the MOT, the parameters are optimized for capturing a large number of atoms from the Zeeman-slowed beam. The effective MOT volume is made large by the application of a moderate magnetic field gradient of 12 G/cm along the axis of the anti-Helmholtz coils. Large-diameter light beams are used of intensities that exceed the saturation intensity, which for the red D -line transitions of ${}^6\text{Li}$ is given by $I_{\text{sat}} = 2.51 \text{ mW/cm}^2$. A laser detuning of about -7Γ is applied, which was experimentally optimized to give the highest atom number. Here, $\Gamma = 2\pi \times 5.87 \text{ MHz}$ is the natural linewidth of the lithium $2S \rightarrow 2P$ transitions. The total number of trapped atoms N reaches a steady-state value after a sufficiently long loading duration. This equilibrium atom number is determined by a balance of the loading and loss rates of atoms from the MOT. The predominant loss mechanisms in the MOT are inelastic collisions ([Ritchie et al., 1995](#)), and collisions with atoms and molecules from the hot background gas ([Bali et al., 1999](#)). From a photodiode that measures the MOT fluorescence we can infer that a steady state atom number is reached at about 30 seconds loading. In practice, shorter loading times of 5-10 s are sufficient to obtain an adequate number of atoms in the MOT.

Compression After the loading phase, the density of the cloud is low and temperatures rather high, at typically 1-3 mK. To obtain lower temperatures and higher densities, the magneto-optical trap is compressed. The cMOT parameters are optimized for obtaining the highest phase space density ρ . In 20 ms, the magnetic field gradient is ramped up to 32 G/cm and simultaneously the intensity of the MOT beams is reduced to around $0.01 I_{\text{sat}}$. During the last 5 ms of the compression phase, the detuning δ is decreased to -2.7Γ . For an overview of

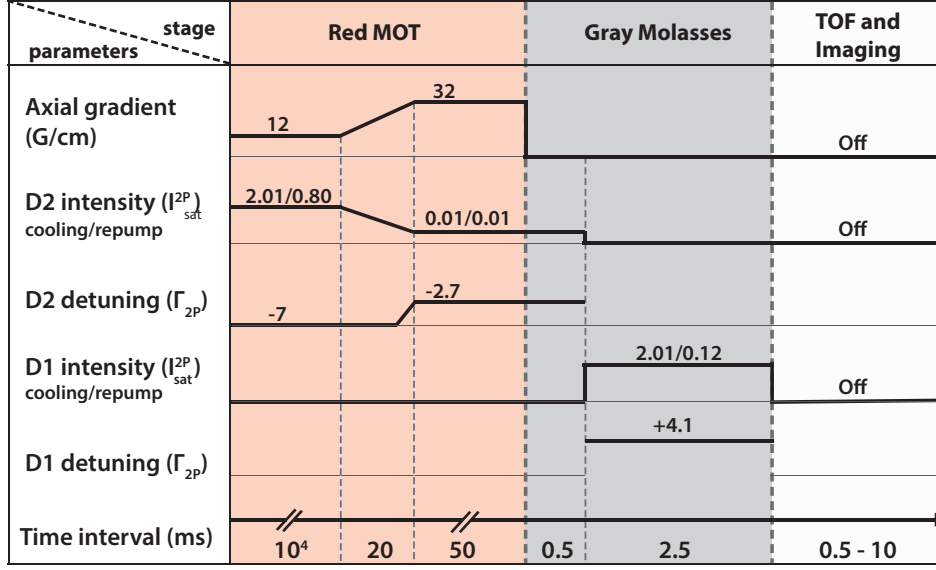


Figure 4.1: Overview of the parameters at each stage of the experimental sequence. As a function of time, the axial gradient of the magnetic quadrupole field, the light intensities per beam, and the detuning with respect to the cooling transition are given for the cMOT, GM cooling phase, and imaging.

the exact timings and changes in parameters during the experimental sequence, see Fig. 4.1. At the end of the compression phase, 8.4×10^8 atoms remain in the cMOT, at a peak density of $3.5 \times 10^{10} \text{ cm}^{-3}$. From time-of-flight measurements we infer a temperature of $380 \mu\text{K}$, as exemplarily shown in Fig. 4.8. The corresponding phase space density of the atomic cloud is calculated according to the method described in Sec. 4.1, yielding a value of 1.7×10^{-6} after the cMOT phase.

4.3 Sub-Doppler cooling in a D_1 gray optical molasses

After the compressed MOT phase on the $2S_{1/2} \rightarrow 2P_{3/2}$ transition, the atoms are transferred into the gray molasses (GM). In preparation for the GM cooling stage, the high magnetic field used in the cMOT is abruptly switched off. We wait for about 0.4 ms to let the field decay, after which also the D_2 light is extinguished. At this point, the laser source for seeding the slave diode laser (see Fig. 3.7) is rapidly switched from the D_2 to the D_1 ECDL to switch on the gray molasses light. The abrupt deactivation of the magnetic quadrupole field leads to the induction of eddy currents and stray magnetic fields in our set-up, as is discussed later in this

section. During the gray molasses therefore, a bias field was applied by the compensation coils installed around the MOT chamber. The D_1 light is applied for 2.5 ms, after which the atoms are probed by standard absorption imaging on the D_2 transition to infer cloud properties. In a number of measurements presented in this section, a systematic error was present in the calibration of the imaging system, so that the atom number is given in arbitrary units. This issue was later resolved, so that our final result is obtained from accurate measurements. The cloud temperature is obtained from time of flight measurements. The temperature trend is also inferred from measurements of the cloud radius at a long time of flight ($t \geq 4$ ms). In this regime the cloud expansion is linear and the trend observed is a direct measure of that of the temperature.

4.3.1 Characterization of the gray molasses

Temporal Evolution We first study the evolution of the gray molasses over time. In Fig. 4.2 the atom number N (a) and cloud radius at long time of flight (b) of the D_1 molasses are plotted against the duration τ_m of the GM cooling stage. A magnetic bias field of -0.9 G was applied (solid markers), which was found to lead to the lowest temperatures at this molasses duration. The atoms are cooled to a minimum temperature in 2.5-3 ms, during which time the atom number stays near-constant. At $\tau_m > 3$ ms however, the temperature starts to rise and the atom number drops. This is attributed to the fact that the magnetic bias field applied compensates well for the eddy fields that are present during the first few milliseconds of the cooling stage, but is not optimal for longer durations, when the eddy fields have decayed. In this context, another scan was performed at a bias field of -0.15 G (open markers), which will be discussed later in this section.

Global detuning The dependence of the atom number on the global detuning $\delta = \delta_{\text{cool}} = \delta_{\text{rep}}$ is shown in Fig. 4.3. The atom number rises sharply as δ increases, and shows a broad maximum at 4.1Γ . Upon further increasing the detuning, the atom number decays, since the capture velocity of the cloud is proportional to $1/\delta^2$ (see Sec. 2.3.4). The temperature was observed to be relatively independent of the global detuning. At red detuning however, the

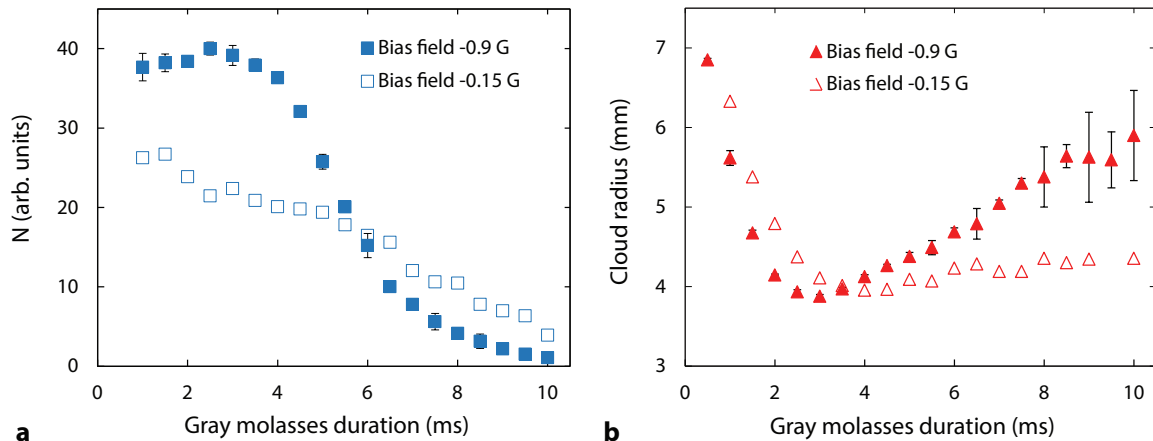


Figure 4.2: Temporal evolution of the gray molasses. The number of captured atoms N (a) and cloud radius at a time of flight of $t = 4$ ms (b) are plotted as a function of the molasses duration τ_m . The solid and open markers correspond to the gray molasses at a magnetic bias field of -0.9 G and -0.15 G respectively.

cloud experiences heating, and for $\tau_m = 2.5$ ms the atoms are quickly lost.

The Raman detuning The cooling mechanism proved much more sensitive to the Raman detuning $\Delta = \delta_{\text{rep}} - \delta_{\text{cool}}$ between the cooling and repumping light, as has become characteristic of gray molasses-cooled clouds (see e.g. Grier et al. (2013); Salomon et al. (2013)). In Fig. 4.4, the atom number (a) and cloud radius at long time of flight (b) are plotted against the Raman detuning in units of the natural linewidth Γ . The data were measured by pre-cooling the cloud at $\Delta = 0$ for 2.3 ms and applying a 0.7-ms pulse at a variable Raman detuning. We find that cooling is optimal at -0.05Γ from exact Raman resonance, in a cooling dip of about -0.15Γ FWHM. The number of atoms captured also displays a clear maximum for a small, red Raman detuning $\Delta = -0.13\Gamma$. On the other hand, for Δ chosen slightly blue of the Raman condition, a strong heating of the cloud occurs, accompanied by a sharp decrease in the number of cooled atoms. This destructive effect is strong enough that when a repumper at $0.1 < \Delta/\Gamma < 0.5$ is applied continuously for a GM duration of 2.5 ms, all atoms are lost.

The strong contribution of the repumper and the enhanced cooling near the Raman condition point to the existence of long-lived coherences between the two hyperfine manifolds $|2S_{1/2}, F = 3/2\rangle$ and $|2S_{1/2}, F = 1/2\rangle$. In the presence of the repumper, another Λ -type three-level system is formed, with new inter-manifold dark states and bright states. The role

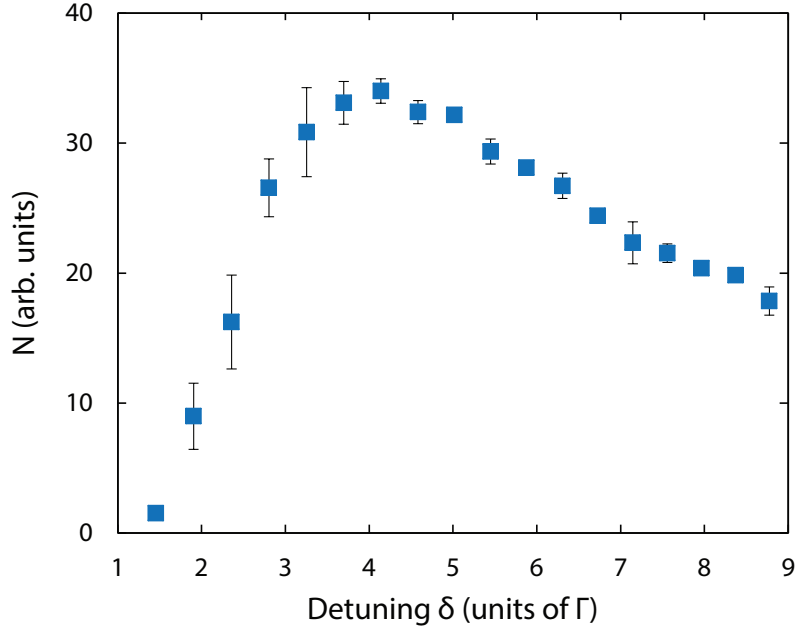


Figure 4.3: The atom number N of the gray molasses after a 2.5 ms cooling phase, as a function of the global detuning $\delta = \delta_{\text{cool}} = \delta_{\text{rep}}$.

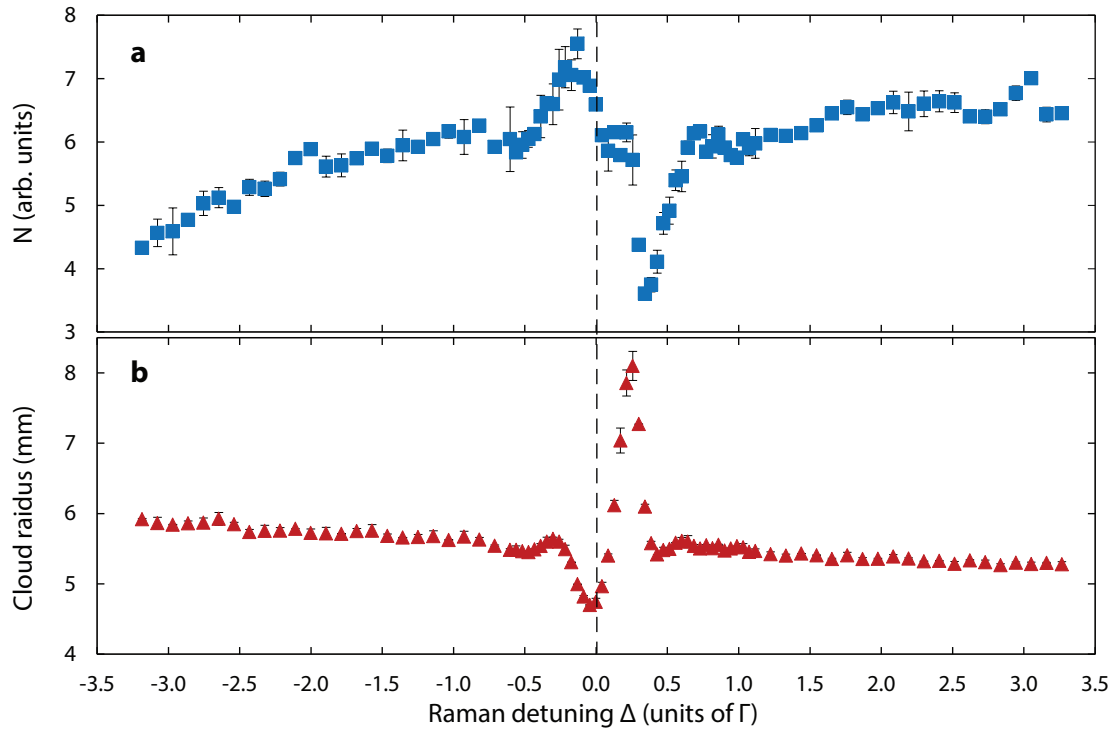


Figure 4.4: The atom number (a) and cloud radius (b) of the gray molasses after a 0.7-ms pulse of D_1 light with variable Raman detuning $\Delta = \delta_{\text{rep}} - \delta_{\text{cool}}$. The MOT was loaded for 5 s, hence a lower atom number is found here as compared to the reported final result. The dashed line indicates $\Delta = 0$ and is meant as a viewing aid.

of the coherences between the ground hyperfine states was studied in detail by [Grier et al. \(2013\)](#), [Nath et al. \(2013\)](#), and [Sievers et al. \(2015\)](#). In order to understand how the addition of the second manifold of ground states modifies the gray molasses scheme, [Grier et al. \(2013\)](#) and [Nath et al. \(2013\)](#) analyze a one-dimensional bichromatic lattice model, which they solve perturbatively and through a continued fractions approach. This model accurately reproduces the experimental observations, but takes only the hyperfine ground states into account while the Zeeman sublevels are disregarded. Standard gray molasses cooling then does not appear in the model. In [Sievers et al. \(2015\)](#), the full level-structure of ${}^6\text{Li}$ atoms is taken into account. A physical picture for the enhanced cooling and heating mechanisms then becomes apparent. For each of the six dressed ${}^6\text{Li}$ Zeeman sublevels, the energy shift is calculated as a function of the position along a 1D $\text{lin}\perp\text{lin}$ optical lattice. Near the Raman condition, the resonant coupling splits the $F = 1/2$ and $F = 3/2$ hyperfine ground states into a bright and a dark manifold. At exact Raman resonance, an additional GM cycle is added, so that the coupling strength of the dark manifold is even weaker than that due to the individual cooling/repumping couplings. This effect persists but becomes weaker as Δ reaches more negative values. The situation becomes reversed for small, positive Δ . In this case, the more weakly-coupled manifold experiences a larger energy shift than the bright states, so that both motional coupling and the Sisyphus cycle now contribute to heating: the atom is observed to be motionally coupled with highest probability to the top of the light shift potential, in which it moves downwards and gains kinetic energy. This heating effect overpowers the cooling that still takes place in the $|2S_{1/2}, F = 3/2\rangle$ Zeeman manifold.

Intensity dependence The effect of the intensity of the GM cooling light on the captured atom number is shown in Fig. 4.5(a). During this measurement, the ratio $I_{\text{rep}}/I_{\text{cool}}$ is kept constant. We observe that, as the cooling intensity is increased, the number of atoms captured by the molasses rises linearly, as indicated by the dashed line in the figure. This is in agreement with the dependence of the capture velocity on the intensity. Since the trend is not yet seen to saturate at $I_{\text{cool}} = 2I_{\text{sat}}$, we expect that a larger atom number can be obtained by using higher-intensity D_1 beams. The temperature of the gray molasses-cooled cloud was observed

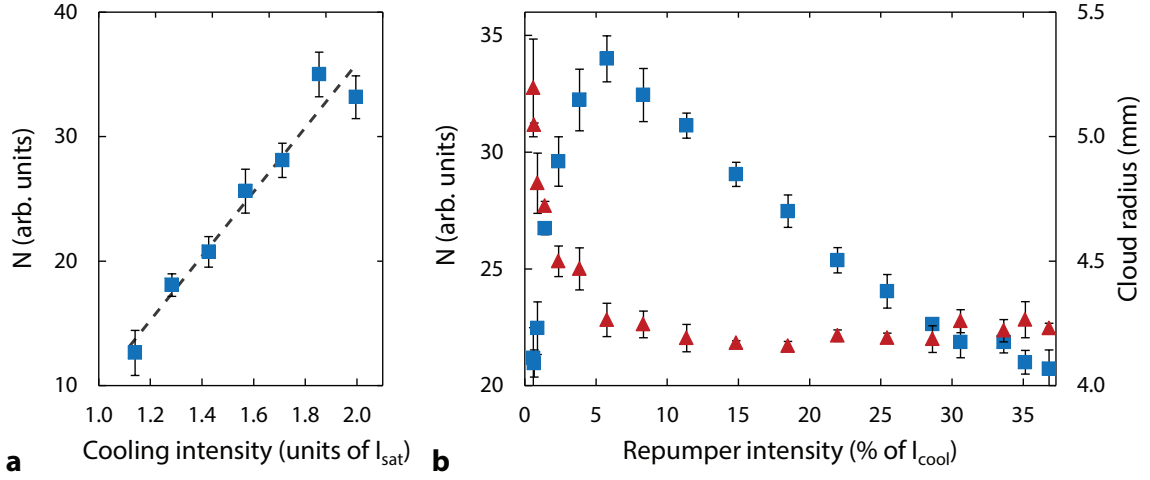


Figure 4.5: The dependence of the gray molasses on the intensities of the D_1 cooling (a) and repumping (b) beams. The atom number N (blue squares) and cloud radius at a long time of flight (red triangles) of the gray molasses are shown after a 2.5 ms cooling phase.

to vary little over the range of cooling intensities measured, and is not shown in the figure.

The intensity of the repumper I_{rep} with respect to the cooling intensity I_{cool} also turned out to play an important role. In Fig. 4.5(b), the captured atom fraction and cloud radius at a long time of flight are plotted against I_{rep} in units of percentage of I_{cool} . The captured atom fraction shows a clear maximum at 5.5%, which corresponds to a repumper intensity of $I_{\text{rep}} = 0.12I_{\text{sat}}$. The intensity of the repumper, and thereby the Rabi frequency of the $|2S_{1/2}, F = 1/2\rangle \rightarrow |2P_{1/2}, F' = 3/2\rangle$ transition, determines the distribution of the atomic population over the ground hyperfine states. At low repump intensities, atoms cease to be cooled efficiently on the cooling transition as they are lost to the $|2S_{1/2}, F = 1/2\rangle$ ground state. This is evident from the large cloud radii and low atom fraction observed at $I_{\text{rep}} < 0.05I_{\text{cool}}$. At higher intensities, the $|2S_{1/2}, F = 3/2\rangle$ state becomes highly populated and reabsorption of spontaneously emitted photons starts to play a larger role (Landini et al., 2011), leading to atom loss.

4.3.2 Compensation of earth and stray magnetic fields

The gray molasses cooling mechanism is known to be sensitive to the presence of magnetic fields. In many studies therefore, a short delay is implemented after switching off the cMOT

fields to ensure a decay to below 100 mG (see e.g. Colzi et al. (2016); Grier et al. (2013)). Some even report a high sensitivity as a function of magnetic field (Salomon et al., 2013), but in such a way that the field can be controlled.

In our set-up, a thorough compensation of earth and stray magnetic fields turned out to be crucial for observing cooling. Before starting the GM cooling phase, the magnetic quadrupole field used during the cMOT is abruptly switched off. Although the current through the Helmholtz coils falls down to zero within 0.2 ms, as measured with a fast current clamp, measurements performed near the MOT chamber with a Hall probe (Lakeshore, HMNT-4E04-VR) still showed disturbances in the magnetic field at 1-2 ms after the MOT current was switched off. These disturbances, which are on the order of several Gauss, were found to be due to eddy currents. Components of our set-up that could be susceptible to the induction of eddy currents are the stainless steel MOT chamber itself, or conductive loops created by stainless steel optomechanical posts, which function as pillars to support the various storeys of breadboards around the MOT chamber.

In the gray molasses cooling stage, we make use of the compensation coils installed around the MOT chamber to minimize the magnetic eddy fields. By scanning the current applied to each of the three pairs of coils, values were found at which the field inside the chamber was canceled, and cooling was immediately observed. In Fig. 4.6 (a), an example is shown of such a scan for the z -axis compensation coil, which was found to have the largest impact on the gray molasses. The scan was performed for a gray molasses cooling period of 2.5 ms, and the bias field values are effective from the start of the cooling stage, during which they remain constant. A clear optimum in both atom number and cloud waist is observed. The value of the compensation field that minimizes the temperature, in this case -0.9 G, is chosen for implementation in the experiment, and we deduct an increase in temperature of $\Delta T \sim 210 \mu\text{K}/\text{G}^2$ when deviating from this optimum.

However, the final temperature of the cloud is only measured after the cooling stage. Since the current applied to the compensation coils is kept constant during the cooling stage, this means that the optimal bias field value thus found is the one that best neutralizes the magnetic field, *averaged* over the time duration of the molasses. For different gray molasses durations

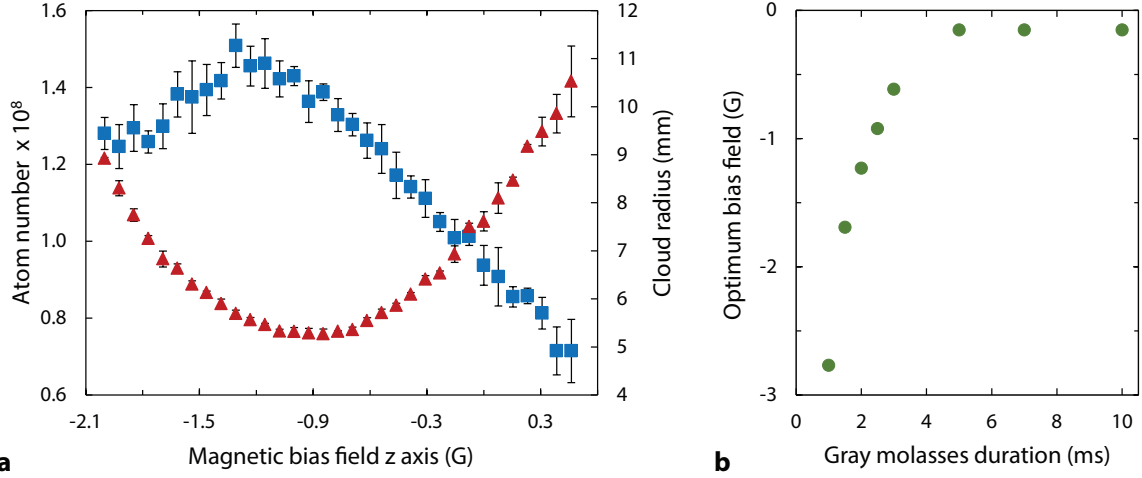


Figure 4.6: (a) Atom number and temperature trend of the gray molasses versus the magnetic field applied along the z axis by the bias coil. Measured at a MOT loading time of 5 s. (b) The optimum bias field along the z axis, defined as the field that minimizes the cloud temperature, as a function of the gray molasses duration.

then, the optimum bias field varies. This is shown in Fig. 4.6 (b), where the optimum bias field B_{opt} along the z -axis, defined as the bias field that leads to the lowest molasses temperature, is plotted as a function of the molasses duration τ_m . During the first 1 ms of the molasses, the bias field optimum lies beyond the minimum value of -3.0 G that can be applied by our coil. As GM cooling progresses, B_{opt} decays and reaches an asymptotic value of -0.15 G at $\tau_m = 5$ ms.

The magnitude of the applied bias field also has a significant effect on the temporal evolution of the atomic cloud, as can be observed from Fig. 4.2. The dataset with the open markers represents a measurement at a bias field of -0.15 G, which is the optimized value for $\tau_m = 7.0$ ms. In this case, the temperature decreases slightly less steeply, but stays relatively constant at longer durations. No significant difference is observed in the minimum temperature reached, as compared to the measurement at the more negative bias field of -0.9 G. The initial capture efficiency of the molasses is however lowered, and the atom number drops throughout the cooling stage. This can be attributed to the fact that the modest bias field does not compensate well for the disturbances in the field that are present during the first few milliseconds of the cooling stage. As a result, the peak density of the cooled cloud is decreased, and we conclude that a short cooling duration at a large applied compensation

field is more beneficial for our purpose, as it leads to a denser cloud.

These measurements also suggest that the efficacy of gray molasses cooling in our set-up could be improved by ‘chirping’ the magnetic bias field, so that the stray field is compensated for to the best of our abilities at each moment during the cooling stage. This we believe would be beneficial for the capture efficiency of the molasses, so that the peak density and thereby also the phase space density of the cloud could be further enhanced. A first attempt was made by adjusting the current applied to the bias coils in steps, each of which lasted 0.5 ms, but no improvement was yet observed. The atom number was observed to decay quickly. In each 0.5-ms step, a different, constant current value was applied, so that the bias field did not evolve smoothly. Most likely, smaller time steps are necessary, especially during the first 2 ms of the molasses stage, or, ideally, a smoothly decreasing bias field with a tunable time constant should be applied.

4.3.3 Analysis of time of flight measurements

Another challenge that we encountered during the investigation of the gray molasses, was the analysis of the cloud temperature. The temperature of the cloud was probed using standard time-of-flight absorption imaging. The D_1 light is switched off, and in the absence of any cooling or trapping forces the cloud is allowed to expand. Using light on the D_2 atomic transition, we then measure the cloud radius at variable expansion times. From the rate of expansion, the temperature is inferred using Eq. 3.3. We expect to distinguish two regimes in the cloud expansion curves. In the first, the atomic density is high, and only those atoms located in the outer region of the cloud whose momentum vector already pointed radially outwards will contribute to expansion of the cloud. This part of the curve is therefore flat. After a certain release time, inter-atomic collisions have been able to take place in the high-density central region of the cloud, ensuring that the atoms experience an effective force radially outwards. After a certain release time then, the expansion becomes linear with the time of flight, with a slope that is proportional to the square root of the cloud temperature.

In our time of flight measurements on the gray molasses however, the flat regime was not observed. In Fig. 4.7, two identical data sets are plotted in panels (a) and (b). As can be

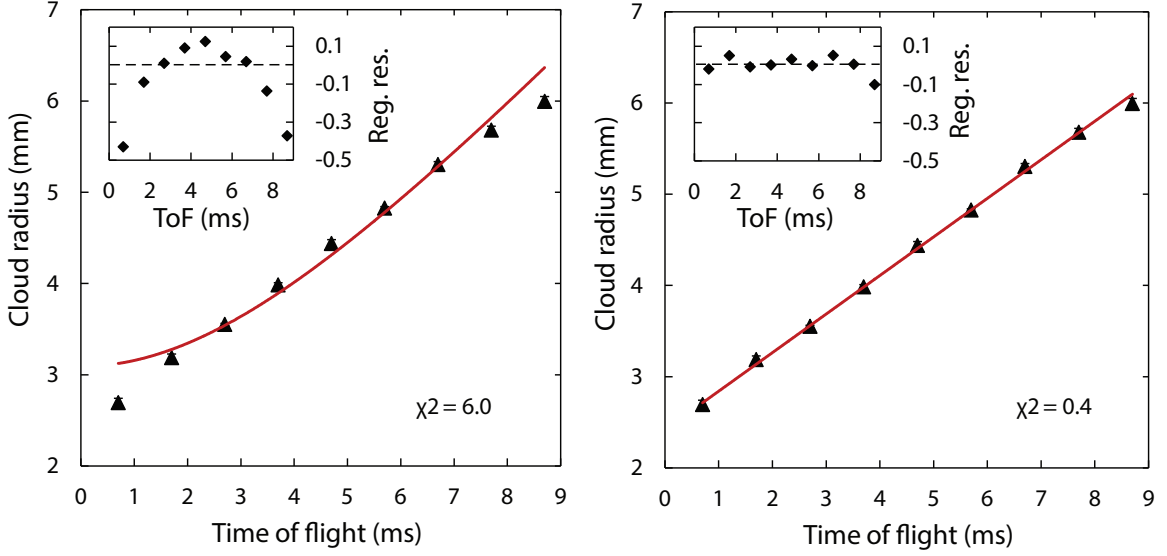


Figure 4.7: Investigation of GM time-of-flight measurements. In both panels, identical data sets are plotted. Panel (a) shows the fit to the Gaussian cloud expansion model described in Sec. 3.6 for the true experimental start time of the expansion. Panel (b) shows the fit when the start time is left variable. The regular residuals for each fit are shown in the insets.

seen, the cloud radius immediately evolves linearly with time of flight, with the same slope of 0.4 mm/ms being maintained at both short and long expansion times. This causes the fitting routine based on the Gaussian cloud expansion model to perform unsatisfactorily. In panel (a), the fit represented by the red line was obtained using true experimental parameters, but the quality of the fit is poor. In the inset, the regular residuals are shown. A large overall reduced $\chi^2 = 6.0$ is observed. The slope of the fit does not match that of the dataset well, and therefore the temperature derived is likely inaccurate.

The absence of a flat expansion regime in our measurements suggests that the cloud was already slowly expanding during the gray molasses cooling stage. This is consistent with only a frictional force being present during the GM stage, and no force that spatially confines the cloud. We therefore introduce the start time t_0 of the expansion as a fit parameter, by replacing the term t^2 by $(t + t_0)^2$ in Eq. 3.3. The time offset t_0 is left variable during the fitting routine to find the fit that best matches the experimental data. The resulting curve is shown in Fig. 4.7 (b), and is characterized by an improved χ^2 factor of 0.4 and significantly reduced regular residuals. From this better fit a value for t_0 is inferred that is lower than

the duration of the gray molasses, pointing to pre-existing momentum-position correlations in the cMOT. While this clearly needs further investigation we are more inclined to believe the temperature extracted from the better curve fit, since the slope of the cloud expansion effectively determines the temperature. The parameters determined from both fits displayed in Fig. 4.7 are summarized in Tab.4.1. Aside from the temperature, one must be mindful not to rely on the variable- t_0 fit to extract other data such as the initial cloud waist $R(0)$, which is clearly not a suitable measure.

	Fixed t_0		Variable t_0	
	Value	Standard error	Value	Standard error
Initial radius $R(0)$ [mm]	3.091	0.075	3.612×10^{-9}	-
Time offset t_0 [ms]	0	-	5.7	0.1
Temperature T [μ K]	73.8	4.0	32.3	0.8

Table 4.1: Overview of the fit parameters extracted from the Gaussian cloud expansion fitting routine, for a fit where the start time t_0 of the expansion is fixed, and for a fit where t_0 is left variable.

Aside from the presence of momentum and position correlation at early expansion times, some experimental factors could be related to the absence of a flat regime in our expansion curves. Since the gray molasses has a capture efficiency of about 40%, some non-cooled atoms are still present during absorption imaging at short times of flight. The presence of this ‘pedestal’ of uncooled atoms was taken into account by making some adjustments to the measurement technique, but images taken at $t < 1.5$ ms may still have experienced some effect. Secondly, a magnetic field is applied to provide a quantization axis for the atoms during imaging. The magnetic eddy fields interfere with this quantization field and cause the resonance frequency of the imaging light not being constant during the first few milliseconds of imaging on the gray molasses cloud. However, we mostly expect this to affect the measured atom number rather than the cloud radius, which was always measured away from resonance to avoid broadening effects due to high optical densities.

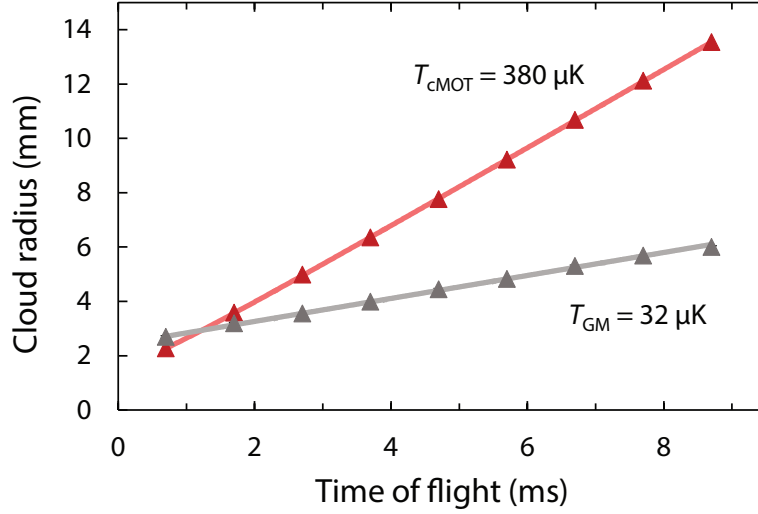


Figure 4.8: Time-of-flight temperature measurement of the cMOT and the gray molasses. The temperature is extracted from a fit based on Eq. 3.3. However, some complications were encountered during the interpretation of the gray molasses temperature measurement, as is described in Sec. 4.3.3.

4.3.4 Optimal performance and discussion

We now turn to the optimal performance of the gray molasses, which is determined by the maximal phase-density ρ . For quantum gas experiments, high peak and phase-space densities of laser-cooled clouds are beneficial for an efficient transfer of atoms to other traps (Lin et al., 2009; O’Hara et al., 2001), and to provide good starting conditions for evaporative cooling. Since the next stage in the experimental sequence is loading of an optical dipole trap, the phase-space density is an important figure of merit for the performance of the gray molasses. The atom number and cloud waist are measured at 0.5 ms time of flight to infer the peak density right after the GM cooling stage. The temperature of the molasses is measured by time-of-flight and from these results the phase-space density is obtained.

The experimental parameters that lead to optimal phase-space densities are summarized in Fig. 4.1. We typically load the MOT for 10 s. Each of the molasses beams has a constant peak intensity of $I_{\text{cool}} = 2.01 I_{\text{sat}}$ for the cooling and $I_{\text{rep}} = 0.12 I_{\text{sat}}$ for the repumping transition. The cooling beam is detuned from the $F = 3/2 \rightarrow F' = 3/2$ transition by $\delta = 4.1\Gamma$, while the two-photon detuning between cooling and repumping light is set to $\Delta = -0.05\Gamma$. In general, up to $N = 2.8 \times 10^8$ cooled atoms are detected in the gray molasses, which corresponds

to a captured fraction of 34% from the cMOT. A typical time-of-flight measurement of the temperature is given in Fig. 4.8, for both the cMOT and the gray molasses. A minimum temperature of $32.3(0.8)\mu\text{K}$ is observed after GM cooling, slightly over 9 times the recoil temperature $T_{\text{rec}} = 3.5\mu\text{K}$. Here, the error in the temperature is obtained from the standard error given in the fitting routine. The D_1 molasses phase improves the cloud temperature by a factor of 10, while the cloud size after the cMOT phase is largely conserved. This leads to an order of magnitude increase in the phase-space density. After a gray molasses duration of 2.5 ms, a maximum phase-space density of $\rho = 1.4 \times 10^{-5}$ is observed. Since a fraction of the atoms remains uncooled by the molasses, the peak density decreases with respect to the cMOT, to $n_0 = 7.0 \times 10^9 \text{ cm}^{-3}$.

Comparison of gray molasses experiments

Table 4.2 summarizes the performance of our molasses, and shows some results obtained for lithium in other studies for comparison (Burchianti et al., 2014; Grier et al., 2013; Sievers et al., 2015). The GM temperature of $32\mu\text{K}$ is colder than what has earlier been observed for lithium, where typically $\sim 40\mu\text{K}$ has been reported. A comparison of the phase-space density, peak density, and atom fraction is given in the following.

Peak and phase-space density Similarly to the present result, Grier et al. (2013) report a phase-space density on the order of 10^{-5} , while Sievers et al. (2015) are close to $\rho \sim 10^{-4}$. It should be noted that since there are no confinement, let alone compression forces present

	T (μK)	N/N_0 (%)	n_0 ($\times 10^{10} \text{ cm}^{-3}$)	ρ ($\times 10^{-5}$)	T_{cMOT} (μK)	I_{cool} (I_{sat})
Present result	32.3	34	0.7	1.4	380	2.01
Grier et al. (2013)	60	100	-	-	600	45
Burchianti et al. (2014)	40.5	75	-	-	500	3
Sievers et al. (2015)	48	60	7.6	8.2	800	14.6

Table 4.2: The performance of the gray molasses as reported in the present study, and that of three other lithium experiments. The optimum temperature T , the captured atom fraction N/N_0 , the density n , and the phase-space density ρ are shown. To aid the comparison, also the cMOT temperature T_{cMOT} and the initial intensity of the D_1 cooling light I_{cool} are given.

during the gray molasses, the cloud size does not decrease during this phase. The peak density thus remains unchanged during GM cooling, or decreases if not all atoms are cooled. The final phase space density is therefore determined by not only the reduction in temperature, but also by the initial peak density of the cloud, and the degree of decrease in peak density during the GM stage.

The studies reporting high phase-space densities for GM consistently also report high peak densities. [Sievers et al. \(2015\)](#) for example find a peak density after the cMOT phase of $n_0 = 18 \times 10^{10} \text{ cm}^{-3}$. Phase-space densities on the order of 10^{-4} have been observed for GM schemes on ^{23}Na ([Colzi et al., 2016](#)) and ^{39}Rb ([Salomon et al., 2013](#)). They too, obtain high peak densities already before the molasses phase. [Salomon et al. \(2013\)](#) for example make use of D_1 light on resonance while loading the MOT on the D_2 transition, to increase the atom number loaded. Subsequently they employ a D_1 - D_2 hybrid cMOT, to reach a peak density $n_0 = 1.3 \times 10^{11}$. Low temperatures are achieved so that all atoms can be cooled with little loss in the peak density during the GM cooling phase. Although we reach a temperature that is comparable to or even lower than what was observed before for GM cooling on ^6Li , the initial peak density of the cMOT cloud, at $n_0 = 3.5 \times 10^{10} \text{ cm}^{-3}$, is comparatively low. Moreover, our captured atom fraction of 35% leads to a reduction in the overall peak density during GM cooling. To improve our phase-space density therefore, increasing either or both the peak density of the cMOT and the capture efficiency of the gray molasses is recommended. To some extent, the peak density before the GM cooling phase can be improved by using longer MOT loading times. For loading times above 10 ms, the atom number in the gray molasses was still observed to increase, albeit with decreasing capture efficiency from the cMOT.

Capture efficiency Where the capture efficiency of the gray molasses is concerned, we believe that the eddy magnetic fields play a crucial role. Better compensation of the field is expected to lead to a significant improvement of the initial capture efficiency of the gray molasses. Also of relevance for the capture efficiency are the thermal velocity $v_{\text{th}} = \sqrt{2k_{\text{B}}T/m}$ of the atoms in the cMOT, and the intensity and detuning of the cooling light, which determine the capture velocity v_{cap} of the GM. To obtain a higher capture efficiency in the GM cooling

stage, one could attempt to improve the cMOT temperature, or use higher optical power in the cooling beams. In Tab. 4.2 also the cMOT temperatures and I_{cool} for each experiment are given, to aid the comparison with the other studies.

A study of the dependence of the captured atom fraction on the initial temperature of the cloud was performed by [Burchianti et al. \(2014\)](#). In their experiment, a cooling intensity of $I_{\text{cool}} = 3I_{\text{sat}}$ was used, similar to our intensity. They experimentally found that at optimal detuning δ , the cooled fraction N/N_0 only approaches 100% for initial temperatures below $150 \mu\text{K}$. Since this is close to the Doppler limit, we expect that improving the cMOT temperature to such an extent is not feasible, and increasing the optical power would be a better alternative. To obtain a rough estimate for what intensities would be necessary, we look at our measurement of the atom number as function of the cooling intensity in Fig. 4.5(a). If the highest observed capture efficiency of 34% is assumed for the data point of highest atom number, we can infer an increase of the captured fraction with the intensity of $25.7\%/I_{\text{sat}}$ from the linear trend line. By extrapolation we can infer that in order to capture 100% of the cMOT atoms, a cooling intensity of at least $4.5I_{\text{sat}}$ per beam would be necessary.

[Sievers et al. \(2015\)](#) also studied the influence of the cooling intensity on the total atom number captured in the gray molasses. Due to a cMOT temperature of $\sim 800 \mu\text{K}$, they experimentally observed a capture efficiency of below 6% at intensities lower than $6I_{\text{sat}}$. However, as in [Rio Fernandes et al. \(2012\)](#), they also observed a linear decrease of the temperature with decreasing intensities. This is generally expected for methods based on polarization gradient cooling, where the temperature lower bound scales with I/δ . They therefore implemented a two-stage gray molasses. A high I_{cool} was used to maximize the capture efficiency, after which the intensity was ramped down to obtain lower temperatures. This leads to an enhanced phase-space density, with minimal reduction in the peak density. The same technique was applied to good effect in other experiments on different species ([Colzi et al., 2016](#); [Rio Fernandes et al., 2012](#); [Salomon et al., 2013](#)).

For the optical powers available to us, these approaches can at the moment not be employed in our set-up. The TA chip that is currently used in the integrated set-up is near the end of its life time, so that we are limited to a total intensity of $I = 2.5 I_{\text{sat}}$ per MOT beam.

With a new chip, the intensity could be increased to more than $I = 5 I_{\text{sat}}$, and thereby more options for increasing the capture efficiency become accessible.

4.4 Summary

In summary, we have implemented and studied a gray optical molasses on the D_1 transition to reach sub-Doppler temperatures for ${}^6\text{Li}$. The phase-space density of a cloud pre-cooled in a compressed MOT is enhanced by an order of magnitude. The molasses proved especially sensitive to the Raman detuning, and to a careful compensation of magnetic fields produced by eddy currents. The latter affects the capture efficiency of the cloud, which could be improved by applying higher optical power in the D_1 cooling beams. Nevertheless, the higher phase-space density obtained in this cooling phase with respect to the compressed MOT on the D_2 transition should facilitate the transfer of the atoms into the optical dipole trap for further cooling to quantum degeneracy.

5 Atomic transfer into an optical dipole trap

In this chapter, an attempt is described to transfer the atoms from the gray molasses-cooled cloud into the crossed optical dipole trap (ODT). A discussion is given of the principle of optical dipole trapping and trap loading dynamics. Subsequently, our results on the transfer efficiency into the ODT are presented. In our first attempts to load the atoms from the gray molasses into the ODT the transfer efficiency was so far low. This is discussed in the context of the loading mechanism of the ODT and the quality of the gray molasses-cooled cloud. To verify that the ODT is operating as desired, we instead pre-cool the cloud in a MOT on the UV-range, narrow-linewidth $2S_{1/2} \rightarrow 3P_{3/2}$ transition, with the intent of emulating the ODT loading experiment performed in our set-up by [Gross et al. \(2016\)](#). An oscillatory phenomenon was however detected in the UV MOT dynamics that interfered with obtaining high densities. This phenomenon is discussed, and an outlook is given on the suitability of the gray molasses for loading the ODT in our experiment.

5.1 Optical dipole trapping

Almost all commonly used strategies for producing quantum degenerate gases rely on the same basic approach: laser cooling of atoms, followed by evaporative cooling in a conservative trap. For the achievement of the first BECs ([Anderson et al., 1995](#); [Bradley et al., 1995](#); [Davis et al., 1995](#)), the latter stage was carried out in a magnetic trap using energetically selective spin transitions, as reviewed by e.g. [Ketterle and Van Druten \(1996\)](#). These traps are characterized by large volumes and tight confinement, but the geometry of the experiments is restricted by the coil arrangement, and experiments concerning the internal atomic dynamics are limited since trapping relies on the internal atomic state. Far-detuned optical dipole

traps offer the advantage that they can be spin-state independent, are effective in a great variety of trapping geometries that provide good optical access, and allow tight confinement and efficient evaporation (Grimm et al., 2000). Most simply, the optical dipole trap can be formed by a single focused laser beam, as first proposed by Ashkin (1978) and demonstrated by Chu et al. (1986). Other configurations include standing wave traps (Vuletić et al., 1998), and crossed-beam traps (Adams et al., 1995).

5.1.1 The conservative potential

Optical dipole traps rely on the dipole force that neutral atoms experience in the presence of a strong light field. Due to the interaction of the induced dipole moment with its driving field, these atoms experience a conservative potential $U_{\text{dip}}(\vec{r})$, which in a classical picture is given by (Grimm et al., 2000)

$$U_{\text{dip}}(\vec{r}) = -\frac{1}{2\epsilon_0 c} \text{Re}(\alpha) I(\vec{r}) \quad . \quad (5.1)$$

Here α is the complex polarizability of the atom, $I(\vec{r})$ is the intensity of the light field at position \vec{r} , ϵ_0 is the vacuum permittivity, and c is the speed of light. The atomic polarizability can be derived within the approximation of a two-level system. With the expression for α , the potential can be written in the rotating-wave approximation, in a way that relates it to the properties of the atomic transition (Grimm et al., 2000):

$$U_{\text{dip}}(\vec{r}) = \frac{3\pi c^2}{2\omega_0^3} \frac{\Gamma}{\delta} I(\vec{r}) \quad . \quad (5.2)$$

The potential is thus proportional to the light intensity $I(\vec{r})$, and inversely proportional to the detuning δ . For red detuning ($\delta < 0$), the dipole potential is negative and the interaction thus attracts atoms into the light field. Potential minima are found at positions with maximum light intensity. For blue detuning ($\delta > 0$) on the other hand, the dipole interaction repels atoms out of the field.

These equations are derived by considering the atom as a simple oscillator subject to the classical radiation field. In real, multi-level atoms the dipole potential experienced depends

on the particular electronic substate that is occupied, and the interaction is described by state-dependent atomic polarizabilities. An intuitive interpretation of the dipole potential in this case is given for a two-level atom in the dressed-atom picture, where the light shift of the ground state induced by the trapping laser is exactly equivalent to the dipole potential. A spatially inhomogeneous field like a Gaussian laser beam then produces a well in the ground-state potential, in which an atom can be trapped. The induced light shift due to the trapping laser can also lead to complications, since it produces a change in the detuning of any simultaneously present cooling or trapping lasers that operate near resonance. Not only the ground state but also the excited state is shifted, in the same or opposite direction compared to the ground state, depending on the detuning of the trapping laser (Grimm et al., 2000). The magnitude of the differential shift depends on the polarizability of the atom, and is state-dependent.

Our optical dipole trap is operated at a wavelength of 1070 nm, far red-detuned from the wavelength of 671 nm for the transition to the first excited state in ${}^6\text{Li}$. The frequency detuning δ is therefore much larger than both the excited and ground state hyperfine splittings. In this regime, Eq. 5.2 remains valid for multi-level atoms, and for linear polarization all Zeeman sublevels of the ground state experience an identical trapping potential. Moreover, by using a large detuning, the optical excitation can be kept extremely low, such that the trap is not limited by the light-induced mechanisms present in radiation-pressure traps like a MOT.

5.1.2 The trap loading process

A common way to load an optical dipole trap is to overlap the trapping region with a laser-cooled atomic cloud, like a (compressed) MOT or a molasses. Usually, the trap is applied a few milliseconds before the cooling lasers are extinguished, to establish the lowest possible temperatures and a quasi-thermal distribution in the trap (Grimm et al., 2000). The efficiency of trap loading and the equilibrium atom number captured in the trap are determined by the competing effects of the loading rate and loss processes. As summarized by Kuppens et al. (2000), losses from the trap can be caused by heating mechanisms, such as spontaneous scat-

tering of ODT light photons, or intensity fluctuations of the ODT beam (Gehm et al., 1998). At high densities, losses are dominated by collisional processes, including photoassociation (Lett et al., 1993) and ground state hyperfine-changing collisions.

The process of loading an optical dipole trap consisting of a single focused laser beam was studied in a microscopic treatment by O’Hara et al. (2001). A conservative potential for the atoms is considered that takes both the MOT that is loaded from and the focused laser beam into account. The number of atoms $N(t)$ captured in the trap at time t is obtained by integrating the phase-space density over the region in phase space where the total conservative potential is attractive. The evolution of the position distribution $n(\vec{x}, t)$ of the atoms is given by a Fokker-Planck equation. For simplicity, the case of radial loading is assumed, and the spatial distribution along the longitudinal axis of the trap is assumed to be identical to that of the MOT. The final equilibrium atom number after trap loading is then found to be

$$N(t \rightarrow \infty) = N_0 \eta \int_0^1 dv (-\ln v) [\exp(\eta v) - 1] \quad , \quad (5.3)$$

where v is the atomic velocity. The final atom number is proportional to the atom number N_0 contained in the overlap volume of the trap with the MOT, and is seen to increase exponentially with the truncation parameter $\eta = U_0/k_B T$, which is the ratio of the trap depth U_0 to the temperature of the cloud.

Generally then, two factors are of importance for the efficiency of trap loading: the temperature of the atomic cloud with respect to the trap depth, and the degree of spatial mode-matching between the cloud and the ODT. Good starting conditions for optical dipole trapping therefore involve a cold, high-density sample. For the truncation parameter η , in previous experiments generally values of 5-10 were chosen (see e.g. Luiten et al. (1996)). The model presented by O’Hara et al. (2001) is not valid for large values of η . However, a strong dependence of the atom number on the trap depth for ratios up to $\eta \simeq 15$ was for example observed by Kuppens et al. (2000), for ODTs operating at a few nanometers off resonance. The atom number in the overlap volume N_0 is given by the density of the laser-cooled cloud multiplied by the ODT dimensions. Increasing the volume of the ODT trapping region has

its limitations, since the trap depth U_0 is proportional to the maximal laser intensity, which is given by $I_{\max} = 2P/\pi\omega^2$. Hence small beam waists ω are favorable to increase the trap depth, and the ODT beam size is a trade-off between enhancing the trap depth and maintaining a sufficient capture volume. Here, trapping in a crossed ODT (Adams et al., 1995) offers a good compromise. In this method, decent trapping volumes are combined with tight confinement.

5.1.3 Gray molasses as precursor to ODT loading

A continuation of cooling while loading the ODT has been shown to lead to large improvements of the final captured atom number (Grimm et al., 2000; Kuppens et al., 2000). ODT loading from a MOT has been applied since the first optical dipole trapping efforts (Chu et al., 1986). Sub-Doppler polarization-gradient cooling in such a MOT leads to temperatures on the order of ~ 10 times the recoil temperature, much lower than the typical depth of a dipole trap, and therefore allows efficient loading of ODTs. Polarization-gradient cooling relies on the modification of the ground-state sublevels by the cooling light. In an ODT the trapping potential is easily made independent from the Zeeman substate, so that the cooling mechanism can be sustained throughout loading. This holds for polarization-induced optical lattices that are produced by red-detuned light, as in standard Sisyphus cooling, or by blue-detuned light as in a gray molasses.

Optical dipole trapping from a gray molasses goes as far back as 1998 (Boiron et al., 1998). Blue Sisyphus cooling was applied to a sample of Cs atoms in a focused-beam ODT. In recent years, two groups (Burchianti et al., 2014; Salomon et al., 2013) have reported using a gray molasses to prepare a cold, dense sample for loading an ODT, leading to the production of quantum degenerate gases (Burchianti et al., 2015; Salomon et al., 2014). It is argued that loading from a gray molasses has the added advantage of being robust against the light shift induced by the trapping laser, since it affects the rather insensitive global detuning δ , and not the critical Raman detuning Δ (Salomon et al., 2013). Burchianti et al. (2014) moreover show that once the atoms are captured in the ODT, another stage of gray molasses cooling can be used to further reduce the temperature of the trapped cloud. A 300- μ s pulse of D_1 light is applied to bring the temperature down from 135 to 80 μ K without atom loss. The cloud

is of high density due to the ODT confinement, and the effect of this on the performance of gray molasses cooling is clear: the minimum temperature reached is twice that obtained in the larger gray molasses cloud. The density-dependence of the efficiency of gray molasses cooling is something that was observed across all ODT loading experiments (Boiron et al., 1998; Burchianti et al., 2014; Salomon et al., 2013).

5.2 Loading the ODT from the gray molasses

Since trapping in an ODT from a gray molasses-cooled cloud has proven to be effective, we here report our attempt to capture atoms from the molasses into the crossed ODT. The ODT set-up and operation was described in Chapter 3. In our trapping geometry, and at the operational optical power of 22.5 W per beam, the effective trap depth was calculated to be $U_0 = k_B \times 330 \mu\text{K}$ (Gross, 2016). This leads to a truncation parameter of about $\eta = 10$ for loading from the gray molasses-cooled cloud. Some parameters of the crossed ODT as used under typical trapping conditions are summarized in Tab. 5.1. For reference, the same parameters are also given for a single-beam ODT consisting of one of the two beams that make up the crossed ODT.

	$1/e^2$ waist	Optical power	U_0/k_B	$\omega_y/2\pi$	$\bar{\omega}_r/2\pi$	Stark shift
Crossed ODT	66 μm	45 W	330 μK	81 Hz	3.04 kHz	4.1 MHz
Single-beam ODT	66 μm	22.5 W	197 μK	9.2 Hz	2.52 kHz	2.1 MHz

Table 5.1: Parameters of the crossed ODT under typical trapping conditions are compared to the calculated trapping parameters for a single-beam ODT consisting of one of the two beams that make up the crossed ODT. Values in the first row are from Gross (2016) and the Stark shift at peak intensity is estimated according to the description in Sec. 5.2.2.

5.2.1 Optimizing the captured atom number

After compression of the D_2 MOT, the atoms are transferred into the gray molasses, and simultaneously the ODT beams are activated at high optical power by fast switching of the AOMs. The trapping region at the intersection of the ODT beams is overlapped with the cloud in the MOT chamber. In this configuration, the frictional force present during the gray

molasses cools the atoms into the attractive ODT potential. After 2.5 ms, the D_1 beams are switched off, and the atoms are held by the ODT. The number of atoms captured in the trap was quantified through in-trap measurements. In these measurements, absorption images were taken while the optical trapping potential was still activated. Previous measurements done in this fashion showed a slight downwards deviation in the atom number measured, but we found that in measurements in which the optical fields were first switched off, the atoms were much harder to detect. The images were typically taken at an ODT hold time of 20 ms, at which the cloud of non-trapped atoms had dispersed.

Loading time and GM parameters For a MOT loading duration of 10 s, the highest atom number measured in the ODT was 3.0×10^5 . For longer MOT loading durations, as shown in Fig. 5.1 (a), we see the atom number increase and become saturated at 18 s, where the maximum of 4.5×10^5 atoms was observed. Scanning over the gray molasses parameters also led to some improvement. As expected, the highest atom number was observed when the GM is operated near Raman resonance, as shown in Fig 5.1 (b). Surprisingly however, the optimum was found at a slightly larger negative Raman detuning than produces the lowest temperature, namely at $\Delta = -0.13\Gamma$. We find that this value yields the highest atom number in the gray molasses. It could however also be a result of a power-broadening of the Fano profile describing the dependence of the gray molasses on the Raman detuning (as shown in Fig. 4.4), in the presence of the high-intensity ODT light field (Burchianti et al., 2014). The magnetic bias fields during the GM phase were also scanned, since the gray molasses proved so sensitive to the magnetic field. The bias fields that optimized the loading of the ODT were found to differ by at most 0.2 G from the values normally used to obtain optimal cooling in the GM, and also lead to a high atom number yield from the gray molasses.

Activation time of the ODT We varied the moment in the experimental sequence at which the ODT beams were activated. We see a significant improvement when the ODT beams are switched on during the molasses, as compared to immediately after the GM cooling beams are switched off, as is shown in Fig. 5.2. In the latter situation, the captured atom number is reduced by a factor three. Starting the ODT even before the molasses beams come on, e.g.

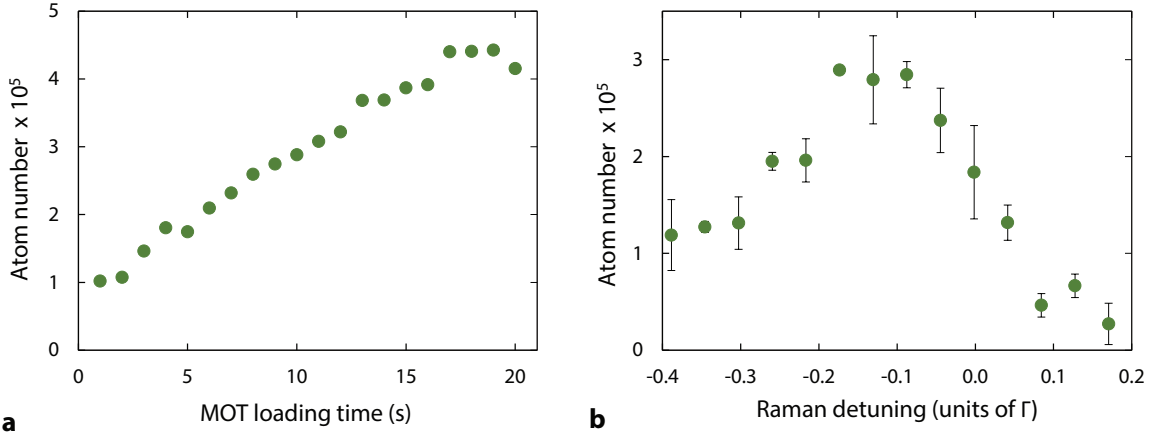


Figure 5.1: The atom number captured in the ODT as a function of (a) the MOT loading time, and (b) the Raman detuning during the GM cooling phase.

during the final part of the cMOT, then does not lead to any further improvement. Since it does not seem to make much difference, in terms of atom number captured in the ODT, whether the ODT comes on during the cMOT or during the GM cooling phase, we conclude that both cooling stages are equally (un)affected by the presence of the high-power light fields.

In these measurements so far, the optical power in both ODT beams is quickly increased from zero to the maximum available power through fast switching of the AOMs in each beam. To compare, we also implement a ramp in which the optical power is gradually increased over 2 ms. The moment at which the ramp is commenced during the cMOT or gray molasses phase is varied, but in each case the atom number captured is seen to be negatively affected, as compared to the situation where the ODT beams are activated near-instantaneously.

Spatial overlap From the absorption images is observed that in the horizontal plane of the MOT chamber, the ODT is slightly offset from the center of the gray molasses cloud by about 0.4 mm in the direction perpendicular to the propagation of the ODT beams. While this is not a large offset, a better overlap would be desirable. Moreover, the image does not give information about a possible spatial mismatch in the vertical direction. We therefore attempted to improve our atom number by making small adjustments to the trap position. While the position of the trap along the propagation axis of the trapping beams can be conveniently adjusted by moving the lens on the translation stage, in the other directions the

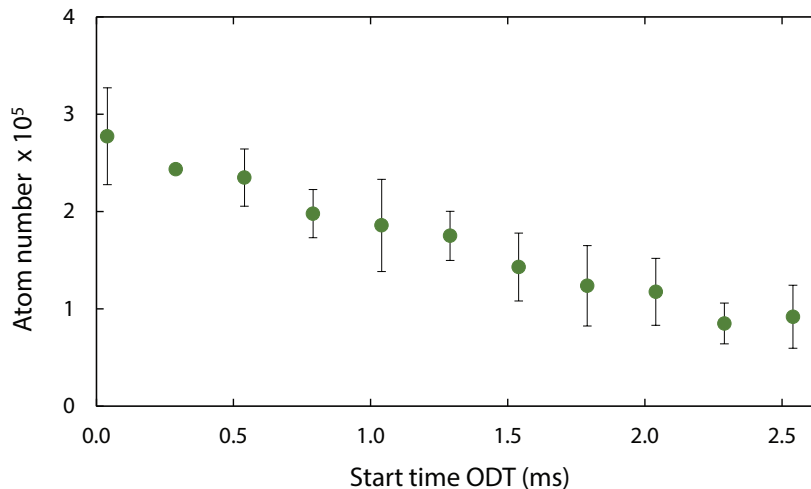


Figure 5.2: The atom number captured in the ODT as a function of the moment in time during the gray molasses phase at which the ODT beams are activated.

trap can only be moved a short distance by careful tuning of the mirror after this lens (see Fig. 3.1). The limit is imposed by the geometry of the science cell, where the diverging ODT beams exit. In the horizontal direction therefore, the trap could not be moved much closer to the center of the gray molasses cloud. There is slightly more freedom in the vertical direction, but an improvement in atom number was not observed.

Instead of moving the ODT closer to the gray molasses cloud, another possibility is to move the gray molasses cloud closer to the trapping region. This would require a beam realignment, since the position of the molasses is solely determined by the intersection region of the six cooling beams, and an optimization has not been done in this way yet in our set-up. That the spatial profile of the molasses is worth optimizing is affirmed by [Burchianti et al. \(2014\)](#), who report improved spatial mode-matching when purposely unbalancing the relative intensities of the molasses beams. This produces a cloud that is elongated in the direction of propagation of the ODT beam. The volume of the trap is furthermore increased by modulating the frequency and amplitude of the ODT’s control AOM at a frequency much greater than the natural trapping frequency. In this way, a time-averaged optical potential is created. Similar methods could be applied in our set-up to both move the cloud and optimize its shape, and are worth investigating.

5.2.2 Discussion

The measured atom number on the order of 10^5 obtained in these first trapping attempts is low compared to values that were achieved previously for ODTs loaded from a gray molasses, where typically $2\text{-}3 \times 10^7$ was observed (Burchianti et al., 2014; Salomon et al., 2013). For loading from a compressed MOT on the UV transition, which was previously done with the ODT in our set-up (Gross et al., 2016), also better results were obtained. We therefore perform a comparison of these different methods of ODT loading, and discuss several possible reasons for the reduced atom number obtained and potential improvements to our current scheme.

Perturbation of GM cooling We first investigate the possibility that the ODT interferes with the operation of the gray molasses. The light shift induced by the ODT could affect the efficacy of GM cooling by shifting the global detuning of the cooling light. Burchianti et al. (2014) quantified the light shift for their single-beam ODT for ${}^6\text{Li}$, which operates at $\lambda = 1073\text{ nm}$, similar to our wavelength. A slope was found of $+6.3(7)\text{ MHz}/(\text{MW}/\text{cm}^2)$, normalized to the estimated peak intensity. Applied to our ODT, this leads to a light shift of 4 MHz , less than one natural linewidth. At such small values, the global detuning δ stays within its broad maximum, and GM operation should hardly be affected. To confirm this, the gray molasses cloud was probed in the presence of the ODT beam. No significant change in the cloud properties was measured, so that this possibility can likely be excluded.

Density of the gray molasses cloud From the discussion in Sec. 5.1 was concluded that the efficiency of loading the optical dipole trap is determined by the truncation parameter η and the atom number N_0 contained in the overlap volume of the trap and the molasses (O'Hara et al., 2001). From our calculation of η we infer that the trap depth should be sufficient for successful loading. Both the UV-loaded ODT by Gross et al. (2016), and the gray molasses-loaded trap by Salomon et al. (2013) use ratios of $\eta \simeq 7$. The peak density obtained in these experiments is however higher: a typical value of $3 \times 10^{11}\text{ cm}^{-3}$ was obtained using cooling on the UV transition (Gross et al., 2016). This substantially increases the number of atoms

in the overlap region of the trap and the cooled cloud.

In the UV MOT, the cloud is compressed until the atoms are confined to a small volume with a typical waist of under 1 mm. Loading the ODT from the UV cMOT therefore profits from good spatial mode-matching. The size of the gray molasses cloud is larger by at least a factor two. To obtain an indication of the effect on trap loading, we estimate the atom number in the overlap volume of the ODT with the gray molasses and with the UV cMOT respectively. From a measurement of the initial size of the trapped cloud as imaged in-trap, we infer the radii of the ODT overlap volume to be roughly $w_r = 2.1$ mm in the radial direction and $w_z = 0.11$ mm in the axial direction. Assuming the atomic distribution in each dimension to be Gaussian, we compute the atom number in each overlap region as $N_0 = (\pi/2)^{3/2} w_r^2 w_z n_0$. For the purpose of this calculation has been assumed that the trapping region of the ODT is located at the center of the laser-cooled cloud. We then find values of $N_0 = 1.2 \times 10^7$ for the UV cMOT, and $N_0 = 2.8 \times 10^5$ for the gray molasses, a factor 43 difference. Since increasing the trap volume will rapidly lower the trap depth, we conclude that a substantial improvement of ODT loading from the molasses can be achieved by increasing the peak density of the gray molasses.

Operation of the ODT A final possibility is that the ODT was not performing optimally during the experiment. At the time of the measurement, the fiber laser that produces the ODT beams had not been activated for some time. It is therefore possible that the optimal alignment was not maintained. Initial absorption images taken at short hold times of atoms loaded into the ODT however showed an increased optical density near the intersection point of the two beams, and by blocking the individual beams was verified that the foci were located near the intersection. We therefore deemed further optimization of the optical alignment not to be necessary. However, the absorption images do not tell about the crossing of the beams in the vertical direction. Minute adjustments were made to the mirrors controlling the individual beams in an attempt to optimize the beam crossing, but no thorough alignment procedure was carried out. A good way to test whether the ODT operation is up to standard is by applying it to the UV MOT, where large samples of trapped atoms were previously obtained

(Gross et al., 2016). Therefore, the UV laser system was reactivated, and the UV MOT optimized. The results are described in the following section.

5.3 Cooling in the UV MOT

To reproduce the ODT loading measurement as performed by Gross et al. (2016), the UV MOT should be optimized so that similar values of the temperature and peak density are achieved as were reported in Sebastian et al. (2014). When this condition is fulfilled, the measurements can be compared and the performance of the optical dipole trap assessed. We therefore adhere closely to the experimental sequence as described in these studies.

The UV light is generated by a commercial frequency doubling system (TOPTICA Photonics AG, TA/DL-SHG Pro). The laser is stabilized and locked to the atomic transition via PID loops using a scheme that combines a fast Pound-Drever-Hall lock (Drever et al., 1983) to an external cavity with a modulation transfer spectroscopy set-up (Shirley, 1982) in a ${}^6\text{Li}$ spectroscopy cell. The main output of the laser passes through an AOM that produces the cooling and repumping frequencies, and is split into three beams that are overlapped with the red MOT beams on dichroic mirrors. The UV beams are retro-reflected after passing through the vacuum chamber, which increases the effectively available power. A detailed description of the UV laser system is given by Gross (2016).

After loading and compression of the MOT on the red D_2 transition, the cooling stage on the narrow-linewidth $2S_{1/2} \rightarrow 3P_{3/2}$ transition is implemented. Repumping light is available on the red D_2 line and on the UV transition. Here the red repumper is used unless otherwise stated. The UV MOT is loaded for 1.5 ms, at a large detuning and shallow magnetic field. During the following 1.5 ms the cloud is compressed by decreasing the detuning and ramping up the magnetic field simultaneously. The MOT is then held for typically 16 ms, to allow the spatial compression of the atomic cloud to be completed. Like for the gray molasses, atom number, density and temperature are inferred from absorption images taken with light on the red D_2 line.

5.3.1 Optimization of phase-space density

After activation of the UV system and alignment of the UV MOT beams, cooling was immediately observed. As expected, most aspects of the UV MOT behaviour closely followed those reported by [Sebastian et al. \(2014\)](#). A minimum temperature of $62 \mu\text{K}$ is reached at a final detuning after compression of $\delta = -2.9\Gamma$. This is in good agreement with values reported for the UV MOT operated with the red repumper. At smaller detunings, the temperature is seen to increase again, due to the higher scattering rate on the UV transition nearer to resonance, which is accompanied by an increase in density-limiting processes like photon reabsorption and light-assisted collisional losses.

Despite the atom number steadily decreasing at lower detunings, [Sebastian et al. \(2014\)](#) see the peak density increase due to a strong reduction of the cloud size. At $\delta = -2.9\Gamma$, they measure a minimum cloud waist of 0.6 mm . At this detuning then, the peak and phase space density reach an optimum. In contrast with this observation, in our measurements the cloud waist was not observed to decrease significantly over a range of $-5 < \delta/\Gamma < -2$, and waists smaller than 1.0 mm were not observed. As a result, the peak density is not improved by decreasing the detuning. The phase space density now peaks at a detuning of -4.3Γ , and a maximum value of 2.5×10^{-5} is found. At this detuning, the peak density is $4.0 \times 10^{10} \text{ cm}^{-3}$, an order of magnitude reduced as compared to the values reported by [Sebastian et al. \(2014\)](#).

In an attempt to reduce the cloud waist further and more closely approach the results obtained by [Sebastian et al. \(2014\)](#), the dependence of the UV MOT on several other experimental parameters was studied, among which the intensity of UV cooling and red repumper light. Moreover, the behaviour of the magnetic field during the red and UV MOT stages was examined, by measuring the current applied to the anti-Helmholtz coils, to verify that the compression of the magnetic field was carried out as required. Eventually, a scan of the hold time of the UV MOT was performed, and a phenomenon was observed that is likely related to the sub-optimal operation of the UV MOT.

5.3.2 Hold time of the UV MOT

As already mentioned by (Sebastian et al., 2014) the high peak density is due to a transient effect. A fast contraction of the cloud was observed, where the cloud waist smoothly decreases and eventually reaches a constant value. In other words, the motion of the cloud during compression can be regarded as that of an overdamped oscillator. Meanwhile, the atom number contained in the MOT decreases, and at a hold time of 16 ms, a maximum in the peak density is measured. In our measurement, we instead observe that the contraction of the cloud is not smooth, but is accompanied by damped oscillations.

Figure 5.3 shows the atom number and cloud radius at a short time of flight as a function of the hold time in the UV MOT. The triangular markers represent the compressed UV MOT operated with respectively the red repumper (solid markers) and the UV repumper (open markers). When the red repumper is used, the cloud expands for about 10 ms right after the compression ramp has finished, before contracting towards a local minimum. One more expansion and contraction cycle is observed before the cloud radius stabilizes at a value of 1.0 mm. Interestingly, in the valleys of the oscillation in the cloud radius, a local maximum is measured in the atom number. For the MOT operated with UV repumping light, the oscillations are smaller. Especially the initial increase in cloud radius is absent, and the first oscillation of the cloud is comparatively reduced.

The instability of the cloud size is already present before the cloud is compressed, as is evident from the dataset represented by square markers. Here, the cloud was held in the UV MOT with red repumper where no compression stage was applied. Large fluctuations are observed in the atom number, while the cloud radius, after an initial expansion, shows less obvious oscillations at longer hold times.

Underdamped oscillator Since the oscillations were first observed at the larger optimal detuning of $\delta = -4.3\Gamma$, an initial thought was that the larger negative detuning affects the slope of the frictional scattering force. A smaller damping coefficient would lead to a relatively flat force profile for small velocities, and the cloud compression would become underdamped. However, when varying the detuning of the compressed UV MOT, the oscillation observed is

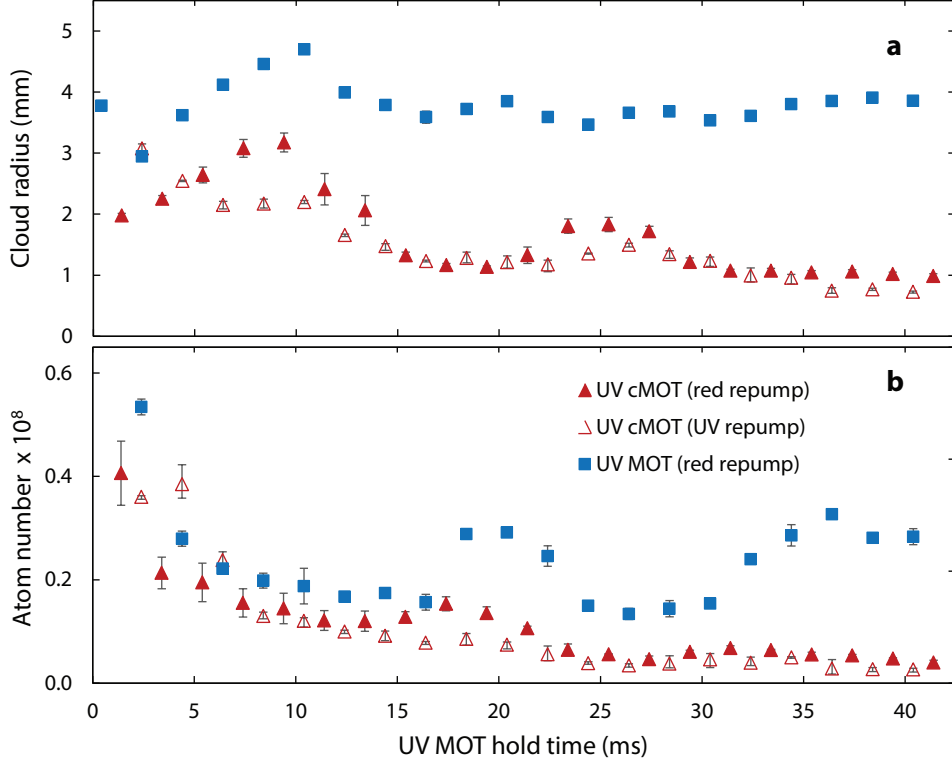


Figure 5.3: The atom number (a) and cloud waist (b) as a function of the hold time in the UV MOT. Measurements are shown for the UV MOT before compression (blue squares), the compressed UV MOT operated with the red repumper (solid red triangles), and the compressed UV MOT operated with the UV repumper (open red triangles).

near-identical in both period and amplitude for all detunings in the range $-4.5 < \delta/\Gamma < -2$.

From the observations that the oscillation is already present before the UV MOT is compressed, and is subdued when the UV repumping light is used, we can speculate that there is a mismatch in the beam alignments, where the intersection region of the UV MOT beams is slightly offset from that of the red D_2 MOT beams. This leads to the atomic cloud being forced to move to a new position at the transition between D_2 and UV cooling, which causes the atoms to undergo a periodic motion in the trap. The fact that, aside from the atom number and cloud radius, the oscillation was also observed in the central position of the cloud, supports this suggestion. When the red repumper is used, the oscillation is enhanced, since both the red and the UV light are simultaneously being scattered. However, optimization of the alignment to improve the overlap of the UV and D_2 MOT beams has not yielded any improvement. This optimization includes the use of the magnetic bias coils to shift the

center of the magnetic quadrupole field to the position where it coincides optimally with the intersection region of the cooling beams.

The origin of the oscillations is currently still under investigation. While this is an interesting physical problem, it hinders the achievement of the previously reported phase-space density results. The investigation into the performance of the ODT is thereby impeded.

5.4 Summary and outlook

In summary, an attempt has been made to transfer atoms cooled by the gray molasses into the crossed optical dipole trap. The process of loading an ODT has been discussed, with an emphasis on loading from a gray molasses-cooled cloud. In our experiment, atom numbers on the order of 10^5 were so far seen to be captured. Loading was optimized by varying the GM parameters and the activation time of the ODT. The relatively low number of atoms observed in the trap can most likely be attributed to the reduced peak density of the atoms in the gray molasses cloud. The temperature-to-trap depth ratio is however favourable, which motivates an investigation into the operation of the ODT. For this purpose we optimize the MOT on the narrow-line UV transition with the intent of loading the ODT from the UV-cooled cloud, as was previously done by [Gross et al. \(2016\)](#). An oscillation is however induced at the transition from the D_2 MOT to the UV MOT, which so far prevents us from obtaining the high peak densities reported previously ([Gross et al., 2016](#); [Sebastian et al., 2014](#)). Conclusions about the proper operation of the ODT can then not be drawn by loading from this UV-cooled cloud.

Based on the results obtained in this chapter, we can not conclusively determine the origin of the low atom number captured in the optical dipole trap. A continuation of efforts to optimize the UV MOT is worthwhile, because loading the ODT from the UV-cooled cloud answers an important open question about the cause of the relatively low atom numbers obtained by loading from the gray molasses. If loading from an optimally UV-cooled cloud also turns out not to be efficient, the problem may reside with the trapping laser, and further investigation will be necessary. On the other hand, if loading from a high-density UV MOT yields atom

numbers on the order observed before, we can conclude that the current performance of gray molasses cooling in our set-up is inadequate for ODT loading. Modifications to the GM cooling scheme can then be made, in particular to better cancel the eddy fields to improve the density of the gray molasses, as discussed in Chapter 4. In either case, loading the ODT from the UV MOT will provide valuable insight into the suitability of the gray molasses as a cooling phase on the road to producing high-density, optically trapped atomic samples.

6 Conclusion and Outlook

In this thesis, our experimental strategy for sub-Doppler laser cooling of ${}^6\text{Li}$ atoms in a gray optical molasses is described. We implement this cooling stage to replace the narrow-line cooling scheme on the UV transition that was earlier used in our set-up (Gross et al., 2016; Sebastian et al., 2014). This frees up the UV laser for use in a photoassociation experiment to study the unexplored $2S\text{-}3P$ asymptote.

The gray molasses is one of few sub-Doppler cooling schemes available for lithium, as standard Sisyphus cooling is hindered by the unresolved hyperfine structure of the excited state. In Chapter 2, sub-Doppler cooling on lithium is discussed in detail, and the gray molasses cooling mechanism is explained. Chapter 3 describes the laser system that is used to produce light on the D_1 wavelength for gray molasses cooling. A set-up is discussed that contains an ECDL and a tapered amplifier to achieve the required optical power for cooling. We improve the design of the TA mount with respect to an earlier version, and characterize the performance of the TA chip. In the experiment a different set-up is eventually used, which allows for more convenient integration of the new D_1 -frequency light into the pre-existing laser system and experimental set-up. A beat system is set up for fast, time-resolved monitoring of the light frequencies, which are rapidly switched between during the different cooling stages in the experimental sequence.

In Chapter 4, the characterization of the gray molasses is presented. After a loading and cooling stage in a MOT on the D_2 atomic transition, the molasses reduces the temperature of the atomic cloud from about $380\ \mu\text{K}$ to $32\ \mu\text{K}$, in 2.5 ms. The phase space density is enhanced by an order of magnitude, to 1.4×10^{-5} . The molasses proved especially sensitive to the Raman detuning between the cooling and repumping light, and to a careful compensation of

magnetic eddy fields. The latter strongly affects the capture efficiency of the cloud, and leads to a reduced peak density after the gray molasses phase. We suspect that this is one of the causes for the relatively low transfer efficiency of the atoms to the optical dipole trap, as is described in Chapter 5. A maximum of 4.5×10^5 atoms is observed to be captured by the ODT in the first loading attempts. We try to verify that the ODT is operating as desired by instead pre-cooling the cloud in a MOT on the UV transition. Here, an oscillatory phenomenon is detected in the UV MOT dynamics that hinders the achievement of high atomic densities. Conclusions about the proper operation of the ODT can then not be drawn by loading from this UV-cooled cloud.

For the performance of a photoassociation experiment in the ODT, high densities and thus high atom numbers in the trap are favourable. The current results are likely not sufficient for meaningful measurements, and improvements should be made to the cooling strategy to enhance the cloud density. Efforts to improve the UV MOT are still ongoing, to confirm the status of the ODT operation. Meanwhile, the performance of the gray molasses can be improved. By pushing for lower temperatures after the D_2 MOT phase and increasing the intensity of the D_1 cooling beams, the capture efficiency of the molasses can be enhanced. However, we expect the largest impact on the peak density after the gray molasses to be obtained by a thorough cancellation of the magnetic eddy fields. These measures, particularly when combined with a cooling scheme that yields a high-density cloud prior to applying the gray molasses, will greatly improve the phase-space density of the laser cooled cloud and provide good conditions for direct loading of the optical dipole trap.

Bibliography

- E. R. I. Abraham, N. W. M. Ritchie, W. I. McAlexander, and R. G. Hulet. Photoassociative spectroscopy of long-range states of ultracold $^6\text{Li}_2$ and $^7\text{Li}_2$. *J. Chem. Phys.*, 103(18): 7773–7778, November 1995. doi:[10.1063/1.470296](https://doi.org/10.1063/1.470296).
- C. S. Adams, H. J. Lee, N. Davidson, M. Kasevich, and S. Chu. Evaporative cooling in a crossed dipole trap. *Phys. Rev. Lett.*, 74:3577–3580, May 1995. doi:[10.1103/PhysRevLett.74.3577](https://doi.org/10.1103/PhysRevLett.74.3577).
- G. Alzetta, A. Gozzini, L. Moi, and G. Orriols. An experimental method for the observation of r.f. transitions and laser beat resonances in oriented na vapour. *Il Nuovo Cimento B (1971-1996)*, 36(1):5–20, 1976. ISSN 1826-9877. doi:[10.1007/BF02749417](https://doi.org/10.1007/BF02749417).
- M. H. Anderson, J. R. Ensher, M. R. Matthews, C. E. Wieman, and E. A. Cornell. Observation of Bose-Einstein condensation in a dilute atomic vapor. *Science*, 269(5221):198–201, 1995. ISSN 0036-8075. doi:[10.1126/science.269.5221.198](https://doi.org/10.1126/science.269.5221.198).
- E. Arimondo and G. Orriols. Nonabsorbing atomic coherences by coherent two-photon transitions in a three-level optical pumping. *Lettere al Nuovo Cimento (1971-1985)*, 17(10): 333–338, 1976. ISSN 1827-613X. doi:[10.1007/BF02746514](https://doi.org/10.1007/BF02746514).
- A. Ashkin. Trapping of atoms by resonance radiation pressure. *Phys. Rev. Lett.*, 40:729–732, Mar 1978. doi:[10.1103/PhysRevLett.40.729](https://doi.org/10.1103/PhysRevLett.40.729).
- A. Aspect, E. Arimondo, R. Kaiser, N. Vansteenkiste, and C. Cohen-Tannoudji. Laser cooling below the one-photon recoil energy by velocity-selective coherent population trapping. *Phys. Rev. Lett.*, 61:826–829, Aug 1988. doi:[10.1103/PhysRevLett.61.826](https://doi.org/10.1103/PhysRevLett.61.826).
- S. Bali, K. M. O’Hara, M. E. Gehm, S. R. Granade, and J. E. Thomas. Quantum-diffractive background gas collisions in atom-trap heating and loss. *Phys. Rev. A*, 60:R29–R32, Jul 1999. doi:[10.1103/PhysRevA.60.R29](https://doi.org/10.1103/PhysRevA.60.R29).
- J. Bardeen, L. N. Cooper, and J. R. Schrieffer. Theory of superconductivity. *Phys. Rev.*, 108: 1175–1204, Dec 1957. doi:[10.1103/PhysRev.108.1175](https://doi.org/10.1103/PhysRev.108.1175).
- F. Bardou, J. P. Bouchaud, O. Emile, A. Aspect, and C. Cohen-Tannoudji. Sub-recoil laser cooling and lévy flights. *Phys. Rev. Lett.*, 72:203–206, Jan 1994. doi:[10.1103/PhysRevLett.72.203](https://doi.org/10.1103/PhysRevLett.72.203).
- M. D. Barrett, J. A. Sauer, and M. S. Chapman. All-optical formation of an atomic Bose-Einstein condensate. *Phys. Rev. Lett.*, 87:010404, Jun 2001. doi:[10.1103/PhysRevLett.87.010404](https://doi.org/10.1103/PhysRevLett.87.010404).
- I. Bloch, J. Dalibard, and W. Zwerger. Many-body physics with ultracold gases. *Rev. Mod. Phys.*, 80(3):885–964, July 2008. doi:[10.1103/RevModPhys.80.885](https://doi.org/10.1103/RevModPhys.80.885).

- D. Boiron, C. Triché, D. R. Meacher, P. Verkerk, and G. Grynberg. Three-dimensional cooling of cesium atoms in four-beam gray optical molasses. *Phys. Rev. A*, 52:R3425–R3428, Nov 1995. doi:[10.1103/PhysRevA.52.R3425](https://doi.org/10.1103/PhysRevA.52.R3425).
- D. Boiron, A. Michaud, P. Lemonde, Y. Castin, C. Salomon, S. Weyers, K. Szymaniec, L. Cognet, and A. Clairon. Laser cooling of cesium atoms in gray optical molasses down to $1.1 \mu\text{k}$. *Phys. Rev. A*, 53(6):R3734–R3737, June 1996. doi:[10.1103/PhysRevA.53.R3734](https://doi.org/10.1103/PhysRevA.53.R3734).
- D. Boiron, A. Michaud, J. M. Fournier, L. Simard, M. Sprenger, G. Grynberg, and C. Salomon. Cold and dense cesium clouds in far-detuned dipole traps. *Phys. Rev. A*, 57:R4106–R4109, Jun 1998. doi:[10.1103/PhysRevA.57.R4106](https://doi.org/10.1103/PhysRevA.57.R4106).
- R. Bowley and M. Sánchez. Introductory statistical mechanics. Oxford University Press, 2nd edition edition, 1999. ISBN 9780198505761.
- C. C. Bradley, C. A. Sackett, J. J. Tollett, and R. G. Hulet. Evidence of bose-einstein condensation in an atomic gas with attractive interactions. *Phys. Rev. Lett.*, 75:1687–1690, Aug 1995. doi:[10.1103/PhysRevLett.75.1687](https://doi.org/10.1103/PhysRevLett.75.1687).
- A. Burchianti, G. Valtolina, J. A. Seman, E. Pace, M. De Pas, M. Inguscio, M. Zaccanti, and G. Roati. Efficient all-optical production of large ^6Li quantum gases using D_1 gray-molasses cooling. *Phys. Rev. A*, 90:043408, Oct 2014. doi:[10.1103/PhysRevA.90.043408](https://doi.org/10.1103/PhysRevA.90.043408).
- A Burchianti, J A Seman, G Valtolina, A Morales, M Inguscio, M Zaccanti, and G Roati. All-optical production of 6 li quantum gases. *Journal of Physics: Conference Series*, 594(1):012042, 2015.
- H. Z. Chen, X. C. Yao, Y. P. Wu, X. P. Liu, X. Q. Wang, Y. X. Wang, Y. A. Chen, and J. W. Pan. Production of large ^{41}K bose-einstein condensates using D_1 gray molasses. *Phys. Rev. A*, 94:033408, Sep 2016. doi:[10.1103/PhysRevA.94.033408](https://doi.org/10.1103/PhysRevA.94.033408).
- J. Chen, J. G. Story, J. J. Tollett, and R. G. Hulet. Adiabatic cooling of atoms by an intense standing wave. *Phys. Rev. Lett.*, 69:1344–1347, Aug 1992. doi:[10.1103/PhysRevLett.69.1344](https://doi.org/10.1103/PhysRevLett.69.1344).
- C. Chin, R. Grimm, P. Julienne, and E. Tiesinga. Feshbach resonances in ultracold gases. *Rev. Mod. Phys.*, 82:1225–1286, Apr 2010. doi:[10.1103/RevModPhys.82.1225](https://doi.org/10.1103/RevModPhys.82.1225).
- S. Chu, L. Hollberg, J. E. Bjorkholm, A. Cable, and A. Ashkin. Three-dimensional viscous confinement and cooling of atoms by resonance radiation pressure. *Phys. Rev. Lett.*, 55(1):48–51, July 1985. doi:[10.1103/PhysRevLett.55.48](https://doi.org/10.1103/PhysRevLett.55.48).
- S. Chu, J. E. Bjorkholm, A. Ashkin, and A. Cable. Experimental observation of optically trapped atoms. *Phys. Rev. Lett.*, 57(3):314–317, July 1986. doi:[10.1103/PhysRevLett.57.314](https://doi.org/10.1103/PhysRevLett.57.314).
- Steven Chu. Nobel lecture: The manipulation of neutral particles. *Rev. Mod. Phys.*, 70:685–706, Jul 1998. doi:[10.1103/RevModPhys.70.685](https://doi.org/10.1103/RevModPhys.70.685).
- Claude N. Cohen-Tannoudji. Nobel lecture: Manipulating atoms with photons. *Rev. Mod. Phys.*, 70:707–719, Jul 1998. doi:[10.1103/RevModPhys.70.707](https://doi.org/10.1103/RevModPhys.70.707).

-
- G. Colzi, G. Durastante, E. Fava, S. Serafini, G. Lamporesi, and G. Ferrari. Sub-doppler cooling of sodium atoms in gray molasses. *Phys. Rev. A*, 93:023421, Feb 2016. doi:[10.1103/PhysRevA.93.023421](https://doi.org/10.1103/PhysRevA.93.023421).
- C. J. Cooper, G. Hillenbrand, J. Rink, C. G. Townsend, K. Zetie, and C. J. Foot. The temperature of atoms in a magneto-optical trap. *EPL (Europhysics Letters)*, 28(6):397, 1994.
- J. Cubizolles, T. Bourdel, S. J. J. M. F. Kokkelmans, G. V. Shlyapnikov, and C. Salomon. Production of long-lived ultracold Li_2 molecules from a Fermi gas. *Phys. Rev. Lett.*, 91:240401, Dec 2003. doi:[10.1103/PhysRevLett.91.240401](https://doi.org/10.1103/PhysRevLett.91.240401).
- J. Dalibard and C. Cohen-Tannoudji. Laser cooling below the Doppler limit by polarization gradients: simple theoretical models. *Journal of the Optical Society of America B*, 6:2023–2045, 1989. doi:[10.1364/JOSAB.6.002023](https://doi.org/10.1364/JOSAB.6.002023).
- N. S. Dattani and R. J. LeRoy. A DPF data analysis yields accurate analytic potentials for Li_2 ($A^1\Sigma_u^+$) and Li_2 ($1^3\Sigma_g^+$) that incorporate 3-state mixing near the Li_2 ($1^3\Sigma_g^+$) state asymptote. *J. Mol. Spectrosc.*, 268:199 – 210, 2011. ISSN 0022-2852. doi:[10.1016/j.jms.2011.03.030](https://doi.org/10.1016/j.jms.2011.03.030).
- K. B. Davis, M. O. Mewes, M. R. Andrews, N. J. van Druten, D. S. Durfee, D. M. Kurn, and W. Ketterle. Bose-einstein condensation in a gas of sodium atoms. *Phys. Rev. Lett.*, 75:3969–3973, Nov 1995. doi:[10.1103/PhysRevLett.75.3969](https://doi.org/10.1103/PhysRevLett.75.3969).
- B. DeMarco and D. S. Jin. Onset of Fermi degeneracy in a trapped atomic gas. *Science*, 285(5434):1703–1706, 1999. doi:[10.1126/science.285.5434.1703](https://doi.org/10.1126/science.285.5434.1703).
- Kai Dieckmann. Bose-Einstein condensation with high atom number in a deep magnetic trap. PhD thesis, Universiteit van Amsterdam, 2001.
- R.W.P. Drever, J.L. Hall, F.V. Kowalski, J. Hough, G.M. Ford, A.J. Munley, and H. Ward. Laser phase and frequency stabilization using an optical resonator. *Appl. Phys. B*, 31(2):97–105–, 1983. ISSN 0946-2171. doi:[10.1007/BF00702605](https://doi.org/10.1007/BF00702605).
- P. M. Duarte, R. A. Hart, J. M. Hitchcock, T. A. Corcovilos, T.-L. Yang, A. Reed, and R. G. Hulet. All-optical production of a lithium quantum gas using narrow-line laser cooling. *Phys. Rev. A*, 84(6):061406–, December 2011. doi:[10.1103/PhysRevA.84.061406](https://doi.org/10.1103/PhysRevA.84.061406).
- Eagleyard Photonics. Tapered amplifier: Product information. PDF file, through personal correspondence, January 2016.
- T. Esslinger, H. Ritsch, M. Weidemüller, F. Sander, A. Hemmerich, and T. W. Hänsch. Purely optical dark lattice. *Opt. Lett.*, 21(13):991–993, Jul 1996. doi:[10.1364/OL.21.000991](https://doi.org/10.1364/OL.21.000991).
- G. Ferrari, M. O. Mewes, F. Schreck, and C. Salomon. High-power multiple-frequency narrow-linewidth laser source based on a semiconductor tapered amplifier. *Opt. Lett.*, 24(3):151–153, Feb 1999. doi:[10.1364/OL.24.000151](https://doi.org/10.1364/OL.24.000151).
- Christopher J. Foot. Atomic physics. Oxford University Press, 2005.

- C. Fort, A. Bambini, L. Cacciapuoti, F.S. Cataliotti, M. Prevedelli, G.M. Tino, and M. Inguscio. Cooling mechanisms in potassium magneto-optical traps. *The European Physical Journal D - Atomic, Molecular, Optical and Plasma Physics*, 3(2):113–118, 1998. ISSN 1434-6079. doi:[10.1007/s100530050154](https://doi.org/10.1007/s100530050154).
- Matthias Fuchs. Development of a high power stabilized diode laser system. Master’s thesis, University of Oregon, 2006.
- M. E. Gehm, K. M. O’Hara, T. A. Savard, and J. E. Thomas. Dynamics of noise-induced heating in atom traps. *Phys. Rev. A*, 58(5):3914–3921, November 1998. doi:[10.1103/PhysRevA.58.3914](https://doi.org/10.1103/PhysRevA.58.3914).
- V. Gokhroo, G. Rajalakshmi, R. Kollengode Easwaran, and C. S. Unnikrishnan. Sub-Doppler deep-cooled bosonic and fermionic isotopes of potassium in a compact 2D⁺-3D MOT set-up. *J. Phys. B: At., Mol. Opt. Phys.*, 44(11):115307, 2011. doi:[10.1088/0953-4075/44/11/115307](https://doi.org/10.1088/0953-4075/44/11/115307).
- L. Goldberg and M. K. Chun. Injection locking characteristics of a 1 w broad stripe laser diode. *Applied Physics Letters*, 53(20):1900–1902, 1988. doi:[10.1063/1.100366](https://doi.org/10.1063/1.100366).
- L. Goldberg, D. Mehuys, M. R. Surette, and D. C. Hall. High-power, near-diffraction-limited large-area traveling-wave semiconductor amplifiers. *IEEE J. Quantum. Electron.*, 29(6):2028–2043, Jun 1993. ISSN 0018-9197. doi:[10.1109/3.234466](https://doi.org/10.1109/3.234466).
- A. T. Grier, I. Ferrier-Barbut, B. S. Rem, M. Delehay, L. Khaykovich, F. Chevy, and C. Salomon. λ -enhanced sub-Doppler cooling of lithium atoms in D₁ gray molasses. *Phys. Rev. A*, 87(6):063411–, June 2013. doi:[10.1103/PhysRevA.87.063411](https://doi.org/10.1103/PhysRevA.87.063411).
- R. Grimm, M. Weidemüller, and Y. B. Ovchinnikov. Optical dipole traps for neutral atoms. *Adv. At., Mol., Opt. Phys.*, Volume 42:95–170, 2000. ISSN 1049-250X. doi:[10.1016/S1049-250X\(08\)60186-X](https://doi.org/10.1016/S1049-250X(08)60186-X).
- Ch. Gross, H. C. J. Gan, and K. Dieckmann. All-optical production and transport of a large ⁶Li quantum gas in a crossed optical dipole trap. *Phys. Rev. A*, 93:053424, May 2016. doi:[10.1103/PhysRevA.93.053424](https://doi.org/10.1103/PhysRevA.93.053424).
- Christian Gross. Atomic 2S_{1/2} to 3P_{3/2} transition for production and investigation of a fermionic lithium quantum gas. PhD thesis, National University of Singapore, 2016.
- G. Grynberg and J.-Y. Courtois. Proposal for a magneto-optical lattice for trapping atoms in nearly-dark states. *EPL (Europhysics Letters)*, 27(1):41, 1994. doi:[10.1209/0295-5075/27/1/008](https://doi.org/10.1209/0295-5075/27/1/008).
- D. Guéry-Odelin and C. Cohen-Tannoudji. Advances in atomic physics. World Scientific, 2011.
- T. L. Gustavson, A. P. Chikkatur, A. E. Leanhardt, A. Görlitz, S. Gupta, D. E. Pritchard, and W. Ketterle. Transport of Bose-Einstein condensates with optical tweezers. *Phys. Rev. Lett.*, 88(2):020401–, December 2001. doi:[10.1103/PhysRevLett.88.020401](https://doi.org/10.1103/PhysRevLett.88.020401).
- P. Hamilton, G. Kim, T. Joshi, B. Mukherjee, D. Tiarks, and H. Müller. Sisyphus cooling of lithium. *Phys. Rev. A*, 89:023409, Feb 2014. doi:[10.1103/PhysRevA.89.023409](https://doi.org/10.1103/PhysRevA.89.023409).

- T. W. Hänsch and A.L. Schawlow. Cooling of gases by laser radiation. *Opt. Commun.*, 13(1):68–69, January 1975. ISSN 0030-4018. doi:[10.1016/0030-4018\(75\)90159-5](https://doi.org/10.1016/0030-4018(75)90159-5).
- J. C. B. Kangara, A. J. Hachtel, M. C. Gillette, J. T. Barkeloo, E. R. Clements, S. Bali, B. E. Unks, N. A. Proite, D. D. Yavuz, P. J. Martin, J. J. Thorn, and D. A. Steck. Design and construction of cost-effective tapered amplifier systems for laser cooling and trapping experiments. *American Journal of Physics*, 82(8):805–817, 2014. doi:[10.1119/1.4867376](https://doi.org/10.1119/1.4867376).
- W. Ketterle and N. J. Van Druten. Evaporative cooling of trapped atoms. *Advances In Atomic, Molecular, and Optical Physics*, 37:181 – 236, 1996. ISSN 1049-250X. doi:[http://dx.doi.org/10.1016/S1049-250X\(08\)60101-9](http://dx.doi.org/10.1016/S1049-250X(08)60101-9).
- W. Ketterle and M. W. Zwierlein. Making, probing and understanding ultracold Fermi gases, January 2008.
- W. Ketterle, D. S. Durfee, and D. M. Stamper-Kurn. Making, probing and understanding Bose-Einstein condensates, 1999.
- S. J. M. Kuppens, K. L. Corwin, K. W. Miller, T. E. Chupp, and C. E. Wieman. Loading an optical dipole trap. *Phys. Rev. A*, 62(1):013406–, June 2000. doi:[10.1103/PhysRevA.62.013406](https://doi.org/10.1103/PhysRevA.62.013406).
- Mark Lam. Molecular spectroscopy of ultracold ${}^6\text{Li}-{}^{40}\text{K}$ molecules. PhD thesis, National University of Singapore, 2016.
- M. Landini, S. Roy, L. Carcagní, D. Trypogeorgos, M. Fattori, M. Inguscio, and G. Modugno. Sub-Doppler laser cooling of potassium atoms. *Phys. Rev. A*, 84(4):043432–, October 2011. doi:[10.1103/PhysRevA.84.043432](https://doi.org/10.1103/PhysRevA.84.043432).
- J. Lawall, F. Bardou, B. Saubamea, K. Shimizu, M. Leduc, A. Aspect, and C. Cohen-Tannoudji. Two-dimensional subrecoil laser cooling. *Phys. Rev. Lett.*, 73:1915–1918, Oct 1994. doi:[10.1103/PhysRevLett.73.1915](https://doi.org/10.1103/PhysRevLett.73.1915).
- J. Lawall, S. Kulin, B. Saubamea, N. Bigelow, M. Leduc, and C. Cohen-Tannoudji. Three-dimensional laser cooling of helium beyond the single-photon recoil limit. *Phys. Rev. Lett.*, 75:4194–4197, Dec 1995. doi:[10.1103/PhysRevLett.75.4194](https://doi.org/10.1103/PhysRevLett.75.4194).
- J. Léonard, M. Lee, A. Morales, Th. M. Karg, T. Esslinger, and T. Donner. Optical transport and manipulation of an ultracold atomic cloud using focus-tunable lenses. *New J. Phys.*, 16(9):093028, 2014. doi:[10.1088/1367-2630/16/9/093028](https://doi.org/10.1088/1367-2630/16/9/093028).
- R. J. LeRoy, N. S. Dattani, J. A. Coxon, A. J. Ross, P. Crozet, and C. Linton. Accurate analytic potentials for Li_2 ($X^1\Sigma_g^+$) and Li_2 ($A^1\Sigma_u^+$) from 2 to 90 Å, and the radiative lifetime of Li ($2p$). *The Journal of Chemical Physics*, 131(20):204309, 2009. doi:[10.1063/1.3264688](https://doi.org/10.1063/1.3264688).
- P. D. Lett, R. N. Watts, C. I. Westbrook, W. D. Phillips, P. L. Gould, and H. J. Metcalf. Observation of atoms laser cooled below the Doppler limit. *Phys. Rev. Lett.*, 61(2):169–172, July 1988. doi:[10.1103/PhysRevLett.61.169](https://doi.org/10.1103/PhysRevLett.61.169).
- P. D. Lett, K. Helmerson, W. D. Phillips, L. P. Ratliff, S. L. Rolston, and M. E. Wagshul. Spectroscopy of Na_2 by photoassociation of laser-cooled Na. *Phys. Rev. Lett.*, 71:2200–2203, Oct 1993. doi:[10.1103/PhysRevLett.71.2200](https://doi.org/10.1103/PhysRevLett.71.2200).

- Y.-J. Lin, A. R. Perry, R. L. Compton, I. B. Spielman, and J. V. Porto. Rapid production of ^{87}Rb Bose-Einstein condensates in a combined magnetic and optical potential. *Phys. Rev. A*, 79(6):063631–, June 2009. doi:[10.1103/PhysRevA.79.063631](https://doi.org/10.1103/PhysRevA.79.063631).
- Z. Lin, K. Shimizu, M. Zhan, F. Shimizu, and H. Takuma. Laser cooling and trapping of Li. *Japanese Journal of Applied Physics*, 30:1324–1326, 1991. doi:[10.1143/JJAP.30.L1324](https://doi.org/10.1143/JJAP.30.L1324).
- J. C. Livas, S. R. Chinn, E. S. Kintzer, J. N. Walpole, C. A. Wang, and L. J. Missaggia. Single-mode optical fiber coupling of high-power tapered gain region devices. *IEEE Photonics Technology Letters*, 6(3):422–424, March 1994. ISSN 1041-1135. doi:[10.1109/68.275506](https://doi.org/10.1109/68.275506).
- O. J. Luiten, M. W. Reynolds, and J. T. M. Walraven. Kinetic theory of the evaporative cooling of a trapped gas. *Phys. Rev. A*, 53:381–389, Jan 1996. doi:[10.1103/PhysRevA.53.381](https://doi.org/10.1103/PhysRevA.53.381).
- N. Masuhara, J. M. Doyle, J. C. Sandberg, D. Kleppner, Th. J. Greytak, H. F. Hess, and G. P. Kochanski. Evaporative cooling of spin-polarized atomic hydrogen. *Phys. Rev. Lett.*, 61:935–938, Aug 1988. doi:[10.1103/PhysRevLett.61.935](https://doi.org/10.1103/PhysRevLett.61.935).
- D. Mehuys, D. F. Welch, and L. Goldberg. 2.0 w cw, diffraction-limited tapered amplifier with diode injection. *Electronics Letters*, 28(21):1944–1946, Oct 1992. ISSN 0013-5194. doi:[10.1049/el:19921246](https://doi.org/10.1049/el:19921246).
- H. J. Metcalf and P. van der Straten. Laser cooling and trapping. Springer, 1999.
- J. D. Miller, R. A. Cline, and D. J. Heinzen. Photoassociation spectrum of ultracold Rb atoms. *Phys. Rev. Lett.*, 71:2204–2207, Oct 1993. doi:[10.1103/PhysRevLett.71.2204](https://doi.org/10.1103/PhysRevLett.71.2204).
- G. Modugno, C. Benkő, P. Hannaford, G. Roati, and M. Inguscio. Sub-Doppler laser cooling of fermionic ^{40}K atoms. *Phys. Rev. A*, 60(5):R3373–R3376, November 1999. doi:[10.1103/PhysRevA.60.R3373](https://doi.org/10.1103/PhysRevA.60.R3373).
- M. Musial and S. A. Kucharski. First principle calculations of the potential energy curves for electronic states of the lithium dimer. *J. Chem. Theory Comput.*, 10(3):1200–1211, March 2014. ISSN 1549-9618. doi:[10.1021/ct401076e](https://doi.org/10.1021/ct401076e).
- D. Nath, R. K. Easwaran, G. Rajalakshmi, and C. S. Unnikrishnan. Quantum-interference-enhanced deep sub-doppler cooling of ^{39}K atoms in gray molasses. *Phys. Rev. A*, 88:053407, Nov 2013. doi:[10.1103/PhysRevA.88.053407](https://doi.org/10.1103/PhysRevA.88.053407).
- P. Nozières and S. Schmitt-Rink. Bose condensation in an attractive fermion gas: From weak to strong coupling superconductivity. *J. Low Temp. Phys.*, 59(3):195–211, 1985. ISSN 1573-7357. doi:[10.1007/BF00683774](https://doi.org/10.1007/BF00683774).
- K. M. O’Hara, S. R. Granade, M. E. Gehm, and J. E. Thomas. Loading dynamics of CO_2 laser traps. *Phys. Rev. A*, 63(4):043403–, March 2001. doi:[10.1103/PhysRevA.63.043403](https://doi.org/10.1103/PhysRevA.63.043403).
- K. M. O’Hara, S. L. Hemmer, M. E. Gehm, S. R. Granade, and J. E. Thomas. Observation of a strongly interacting degenerate Fermi gas of atoms. *Science*, 298(5601):2179–2182, 2002. doi:[10.1126/science.1079107](https://doi.org/10.1126/science.1079107).
- M. A. Ol’shanii and V. G. Minogin. Three-dimensional velocity-selective coherent population trapping of (3+1)-level atoms. *Quantum Optics: Journal of the European Optical Society Part B*, 3(6):317, 1991.

-
- F. Papoff, F. Mauri, and E. Arimondo. Transient velocity-selective coherent population trapping in one dimension. *J. Opt. Soc. Am. B*, 9(3):321–331, Mar 1992. doi:[10.1364/JOSAB.9.000321](https://doi.org/10.1364/JOSAB.9.000321).
- W. D. Phillips and H. Metcalf. Laser deceleration of an atomic beam. *Phys. Rev. Lett.*, 48(9):596–599, March 1982. doi:[10.1103/PhysRevLett.48.596](https://doi.org/10.1103/PhysRevLett.48.596).
- William D. Phillips. Nobel lecture: Laser cooling and trapping of neutral atoms. *Rev. Mod. Phys.*, 70:721–741, Jul 1998. doi:[10.1103/RevModPhys.70.721](https://doi.org/10.1103/RevModPhys.70.721).
- E. L. Raab, M. Prentiss, Alex Cable, Steven Chu, and D. E. Pritchard. Trapping of neutral sodium atoms with radiation pressure. *Phys. Rev. Lett.*, 59(23):2631–2634, December 1987. doi:[10.1103/PhysRevLett.59.2631](https://doi.org/10.1103/PhysRevLett.59.2631).
- C. A. Regal, M. Greiner, and D. S. Jin. Observation of resonance condensation of fermionic atom pairs. *Phys. Rev. Lett.*, 92:040403, Jan 2004. doi:[10.1103/PhysRevLett.92.040403](https://doi.org/10.1103/PhysRevLett.92.040403).
- D. Rio Fernandes, F. Sievers, N. Kretzschmar, S. Wu, C. Salomon, and F. Chevy. Sub-Doppler laser cooling of fermionic ^{40}K atoms in three-dimensional gray optical molasses. *EPL (Europhysics Letters)*, 100(6):63001, 2012. doi:[10.1209/0295-5075/100/63001](https://doi.org/10.1209/0295-5075/100/63001).
- N. W. M. Ritchie, E. R. I. Abraham, and R. G. Hulet. Trap loss collisions of ^7Li : The role of trap depth. *Laser Phys.*, Vol. 4:1066, 1994. doi:[10.1103/physreva.51.r890](https://doi.org/10.1103/physreva.51.r890).
- N. W. M. Ritchie, E. R. I. Abraham, Y. Y. Xiao, C. C. Bradley, R. G. Hulet, and P. S. Julienne. Trap-loss collisions of ultracold lithium atoms. *Phys. Rev. A*, 51(2):R890–R893, February 1995. doi:[10.1103/PhysRevA.51.R890](https://doi.org/10.1103/PhysRevA.51.R890).
- M. S. Safronova, U. I. Safronova, and Charles W. Clark. Magic wavelengths for optical cooling and trapping of lithium. *Phys. Rev. A*, 86(4):042505–, October 2012. doi:[10.1103/PhysRevA.86.042505](https://doi.org/10.1103/PhysRevA.86.042505).
- C. Salomon, J. Dalibard, W. D. Phillips, A. Clairon, and S. Guellati. Laser cooling of cesium atoms below $3\ \mu\text{K}$. *EPL (Europhysics Letters)*, 12(8):683, 1990. doi:[10.1063/1.41003](https://doi.org/10.1063/1.41003).
- G. Salomon, L. Fouché, P. Wang, A. Aspect, P. Bouyer, and T. Bourdel. Gray-molasses cooling of ^{39}K to a high phase-space density. *EPL (Europhysics Letters)*, 104(6):63002, 2013. doi:[10.1209/0295-5075/104/63002](https://doi.org/10.1209/0295-5075/104/63002).
- G. Salomon, L. Fouché, S. Lepoutre, A. Aspect, and T. Bourdel. All-optical cooling of ^{39}K to Bose-Einstein condensation. *Phys. Rev. A*, 90:033405, Sep 2014. doi:[10.1103/PhysRevA.90.033405](https://doi.org/10.1103/PhysRevA.90.033405).
- U. Schünemann, H. Engler, M. Zielonkowski, M. Weidemüller, and R. Grimm. Magneto-optic trapping of lithium using semiconductor lasers. *Opt. Commun.*, 158:263–272, December 1998. ISSN 0030-4018. doi:[10.1016/S0030-4018\(98\)00517-3](https://doi.org/10.1016/S0030-4018(98)00517-3).
- J. Sebastian, Ch. Gross, Ke Li, H. C. J. Gan, Wenhui Li, and K. Dieckmann. Two-stage magneto-optical trapping and narrow-line cooling of ^6Li atoms to high phase-space density. *Phys. Rev. A*, 90:033417, Sep 2014. doi:[10.1103/PhysRevA.90.033417](https://doi.org/10.1103/PhysRevA.90.033417).

- M. S. Shahriar, P. R. Hemmer, M. G. Prentiss, P. Marte, J. Mervis, D. P. Katz, N. P. Bigelow, and T. Cai. Continuous polarization-gradient precooling-assisted velocity-selective coherent population trapping. *Phys. Rev. A*, 48:R4035–R4038, Dec 1993. doi:[10.1103/PhysRevA.48.R4035](https://doi.org/10.1103/PhysRevA.48.R4035).
- S-Q. Shang, B. Sheehy, H. Metcalf, P. van der Straten, and G. Nienhuis. Velocity-selective resonances and sub-Doppler laser cooling. *Phys. Rev. Lett.*, 67:1094–1097, 1991. doi:[10.1103/PhysRevLett.67.1094](https://doi.org/10.1103/PhysRevLett.67.1094).
- J. H. Shirley. Modulation transfer processes in optical heterodyne saturation spectroscopy. *Opt. Lett.*, 7(11):537–539, November 1982. doi:[10.1364/OL.7.000537](https://doi.org/10.1364/OL.7.000537).
- I. Shvarchuck, K. Dieckmann, M. Zielonkowski, and J.T.M. Walraven. Broad-area diode-laser system for a rubidium bose-einstein condensation experiment. *Applied Physics B*, 71(4): 475–480, Oct 2000. ISSN 1432-0649. doi:[10.1007/s003400000395](https://doi.org/10.1007/s003400000395).
- F. Sievers, N. Kretzschmar, D. Rio Fernandes, D. Suchet, M. Rabinovic, S. Wu, C. V. Parker, L. Khaykovich, C. Salomon, and F. Chevy. Simultaneous sub-Doppler laser cooling of fermionic ${}^6\text{Li}$ and ${}^{40}\text{K}$ on the D_1 line: Theory and experiment. *Phys. Rev. A*, 91:023426, Feb 2015. doi:[10.1103/PhysRevA.91.023426](https://doi.org/10.1103/PhysRevA.91.023426).
- A. G. Truscott, K. E. Strecker, W. I. McAlexander, G. B. Partridge, and R. G. Hulet. Observation of Fermi pressure in a gas of trapped atoms. *Science*, 291(5513):2570–2572, 2001. ISSN 0036-8075. doi:[10.1126/science.1059318](https://doi.org/10.1126/science.1059318).
- J. Ulmanis, J. Deiglmayr, M. Repp, R. Wester, and M. Weidemüller. Ultracold molecules formed by photoassociation: Heteronuclear dimers, inelastic collisions, and interactions with ultrashort laser pulses. *Chem. Rev.*, 112(9):4890–4927, 2012. doi:[10.1021/cr300215h](https://doi.org/10.1021/cr300215h). PMID: 22931226.
- D. Voigt, E.C. Schilder, R.J.C. Spreeuw, and H.B. van Linden van den Heuvell. Characterization of a high-power tapered semiconductor amplifier system. *Applied Physics B*, 72(3): 279–284, Feb 2001. ISSN 1432-0649. doi:[10.1007/s003400100513](https://doi.org/10.1007/s003400100513).
- V. Vuletić, C. Chin, A. J. Kerman, and S. Chu. Degenerate raman sideband cooling of trapped cesium atoms at very high atomic densities. *Phys. Rev. Lett.*, 81:5768–5771, Dec 1998. doi:[10.1103/PhysRevLett.81.5768](https://doi.org/10.1103/PhysRevLett.81.5768).
- T. Walker, D. Sesko, and C. Wieman. Collective behavior of optically trapped neutral atoms. *Phys. Rev. Lett.*, 64:408–411, Jan 1990. doi:[10.1103/PhysRevLett.64.408](https://doi.org/10.1103/PhysRevLett.64.408).
- J. N. Walpole. Semiconductor amplifiers and lasers with tapered gain regions. *Optical and Quantum Electronics*, 28(6):623–645, Jun 1996. ISSN 1572-817X. doi:[10.1007/BF00411298](https://doi.org/10.1007/BF00411298).
- J. N. Walpole, E. S. Kintzer, S. R. Chinn, C. A. Wang, and L. J. Missaggia. High-power strained-layer ingaas/algaas tapered traveling wave amplifier. *Applied Physics Letters*, 61(7):740–742, 1992. doi:[10.1063/1.107783](https://doi.org/10.1063/1.107783).
- J.T.M. Walraven. Quantum gases - statistics and interactions, 2014.

-
- D. Wandt, M. Laschek, F. v. Alvensleben, A. Tnnermann, and H. Welling. Continuously tunable 0.5 w single-frequency diode laser source. *Optics Communications*, 148(4):261 – 264, 1998. ISSN 0030-4018. doi:[http://dx.doi.org/10.1016/S0030-4018\(97\)00696-2](http://dx.doi.org/10.1016/S0030-4018(97)00696-2).
- M. Weidemüller, T. Esslinger, M. A. Ol’shanii, A. Hemmerich, and T. W. Hänsch. A novel scheme for efficient cooling below the photon recoil limit. *EPL (Europhysics Letters)*, 27(2):109, 1994. doi:[10.1209/0295-5075/27/2/006](https://doi.org/10.1209/0295-5075/27/2/006).
- D. S. Weiss, E. Riis, Y. Shevy, P. J. Ungar, and S. Chu. Optical molasses and multilevel atoms: experiment. *J. Opt. Soc. Am. B*, 6(11):2072–2083, Nov 1989. doi:[10.1364/JOSAB.6.002072](https://doi.org/10.1364/JOSAB.6.002072).
- D. J. Wineland and H. Dehmelt. Proposed $10^{14}\Delta\nu < \nu$ laser fluorescence spectroscopy on TI^+ mono-ion oscillator III. *Bulletin of the American Physical Society*, 20:637, 1975.
- X. Xu, Th. H. Loftus, J. W. Dunn, C. H. Greene, J. L. Hall, A. Gallagher, and J. Ye. Single-stage sub-Doppler cooling of alkaline earth atoms. *Phys. Rev. Lett.*, 90(19):193002–, May 2003. doi:[10.1103/PhysRevLett.90.193002](https://doi.org/10.1103/PhysRevLett.90.193002).
- B. Zimmermann, T. Müller, J. Meineke, T. Esslinger, and H. Moritz. High-resolution imaging of ultracold fermions in microscopically tailored optical potentials. *New J. Phys.*, 13(4):043007–, 2011. ISSN 1367-2630. doi:[10.1088/1367-2630/13/4/043007](https://doi.org/10.1088/1367-2630/13/4/043007).
- C. Zimmermann, J. Walz, and T. W. Hänsch. Solid-state laser sources for (anti)hydrogen spectroscopy. *Hyperfine Interactions*, 100(1):145–152, Dec 1996. ISSN 1572-9540. doi:[10.1007/BF02059939](https://doi.org/10.1007/BF02059939).